学位論文（要約）

Theoretical modeling of transmission spectra of exoplanet atmospheres with hydrocarbon haze and applications to multi-wavelength transit observations

（炭化水素ヘイズを持つ系外惑星大気の透過スペクトルの
理論モデリングと多波長トランジット観測への応用）

平成29年12月博士（理学）申請
東京大学大学院理学系研究科
地球惑星科学専攻
川島　由依

Abstract

Since the first discovery of an exoplanet in 1995, detection of more than 3000 exoplanets has been reported. The atmospheric composition of planets provides a valuable clue to understanding the bulk composition and origin of exoplanets. A promising method for atmospheric characterization is multi-wavelength transit observation, which measures an apparent decrease in stellar brightness during planetary transit in front of its host star (called transit depth). Sets of transit depths so far measured at different wavelengths (called transmission spectra) are somewhat diverse: Some show steep spectral slope features in the visible, some contain featureless spectra in the near-infrared, some show distinct features from radiative absorption by gaseous species. These facts infer the existence of haze in the atmospheres.

Previous studies that addressed theoretical modeling of transmission spectra of hydrogen-dominated atmospheres with haze used some assumed distribution and size of haze particles and did not access the viability of those assumed haze properties sufficiently from a physical point of view. In addition, although the previous studies found that various haze parameters being chosen, one can generate the observed variation in transmission spectra, it remains to be clarified what yields such a variety of haze properties.

In this doctoral thesis, we focus on photochemically-produced hydrocarbon aerosols as a possible candidate for the haze. Most transiting exoplanets, which orbit very close to their host stars, are constantly exposed to strong stellar UV radiation. Also, many of the transiting small exoplanets detect so far have relatively large radii, which means that they likely have hydrogen-rich atmospheres. Such atmospheres would contain precursor molecules such as CH_4 and HCN for hydrocarbon. Furthermore, current and near-future target stars for exoplanet search are low-mass, low-temperature main-sequence stars, which are called M dwarfs. Observation shows that M dwarfs are diverse in UV emission intensity. Since hazes are formed through photochemical reactions triggered by photo-dissociation of CH_4, the transmission spectrum of an exoplanet atmosphere with such

haze should depend on the UV intensity of its host star. Thus, the diversity in UV intensity of M dwarfs can be considered to bring about the diversity of transmission spectra, which no previous theoretical studies have explored.

The purpose of this doctoral thesis is to explore what diversity of transmission spectra of exoplanets are brought from different production rates and distributions of the monomers of haze particles, which are related to the variety in UV intensities of M dwarfs. To do so, we develop a new numerical code from scratch for simulating transmission spectra of transiting exoplanet atmospheres, which include calculations of thermo- and photo-chemistry, particle growth, opacities of gases and particles, and wavelength-dependent atmospheric absorption of stellar radiation. Then, we model the haze formation processes, assuming hydrogen-dominated atmospheres of close-in warm ($\lesssim$ 1000 K) exoplanets, derive the realistic distribution of the size and number density of haze particles, and explore its impacts on transmission spectra, which were not investigated previously. Then, we explore the production rate of haze monomers and resultant transmission spectra of the atmospheres of currently observable warm exoplanets including GJ 1214b, GJ 3470b, and GJ 436b.

First, we have found that the haze particles tend to distribute more broadly in the atmosphere than previously assumed and consist of various sizes. We have also found that the difference in the production rate of haze monomers with ten orders of magnitude, which relates to the UV irradiation intensity from the host star, yields the diversity of transmission spectra observationally suggested: Completely flat spectra, spectra with only extinction features of hazes (i.e., spectral slope due to Rayleigh scattering and absorption features of hazes), spectra with slope due to Rayleigh scattering and some molecular absorption features, and spectra with only molecular absorption features.

In addition, we have explored the dependences of the vertical distribution of haze particles and the gaseous species, and the transmission spectrum on the other model parameters such as eddy diffusion coefficient, C/O ratio, atmospheric temperature structure, and monomer size. We have found that efficient eddy diffusion yields a steeper Rayleigh-scattering slope in the visible and that the differences in C/O ratio and monomer size have little effect on the vertical distribution of haze particles and the gaseous species, and the transmission spectrum.

Moreover, by applying a simplified grain-growth model, we have examined the validity of characteristic size approximation in particle growth calculation. We have quantified the precisions of observed transit depths beyond which the characteristic approximation suffices to be used for comparison with observation.

Finally, applying our developed models to GJ 1214b, GJ 3470b, and GJ 436b, we have found the followings: For the atmosphere of GJ 1214b, the high production rate of haze monomers can explain the observed flatness of the transmission spectra in the near-infrared and it is likely that large amount of hazes is present in the atmosphere. For the atmosphere of GJ 3470b, the relatively low rate of monomer production matches the observed spectrum; a steep spectral slope in the visible and relatively featureless in the near-infrared. For the atmosphere of GJ 436b, the values of modest to high rate of monomer production can explain the observed relatively featureless spectrum in the near-infrared. To further constrain the monomer production rate, the transit observations in the visible are crucially important, where transit depth strongly varies depending on the monomer production rate. The existence of hazes in these three planets are inferred from our detailed theoretical modeling of haze particles in addition to the observations so far.

At present, the number of exoplanets suitable for atmospheric characterization is still small due to lack of bright targets and sufficient observational precision. Fortunately, all-sky survey projects such as Transiting Exoplanet Survey Satellite (TESS) launched in June 2018 and PLAnetary Transits and Oscillations of stars (PLATO) launched in the mid-2020s will detect a great number of transiting exoplanets around nearby stars that are bright enough for atmospheric characterization. Also, James Webb Space Telescope (JWST) scheduled for launch in late spring of 2019 and Atmospheric Remote-sensing Infrared Exoplanet Large-survey (ARIEL) planned for launch in the mid-2020s will perform high-precision spectroscopy of transiting exoplanets in the infrared. In addition, World Space Observatory-UltraViolet (WSO-UV) planned for launch in the mid-2020s will perform exoplanet transit observation in the UV. In this thesis, we have predicted the diversity in transmission spectra of warm exoplanets exposed to stellar UV, which will be the primary targets of such near-future atmospheric characterization missions. In particular, simultaneous observations in the UV, visible, and infrared are quite interesting for verifying our predictions in this thesis. In any case, the transmission spectrum models developed in this thesis will be able to make a great contribution to the near-future atmospheric characterization of exoplanets.

Acknowledgements

Yui Kawashima

Contents

Chapter 1

General Introduction

1.1 Background

A planet orbiting a star other than the Sun, which is often called an exoplanet, was first discovered in 1995 (Mayor & Queloz, 1995). Since then, detection of about 3000 exoplanets has been reported (http://exoplanets.org, 2017 Dec. 15), thanks to recent advances in observational techniques, revealing the common existence of planets in the universe. There are some observational methods to detect exoplanets: radial velocity measurement, transit photometry (or transit measurement), astrometry, timing measurement, gravitational microlensing, and direct imaging.

Among these methods, most of the known exoplanets have been discovered by transit measurement. By this method, we can constrain the planetary radius while the mass of the planet can be constrained by radial velocity, as explained below:

Transit photometry When a planet passes in front of its host star as seen from the observer (this event is called a transit or primary eclipse), the apparent stellar brightness declines. By detecting this periodical change of the stellar brightness, the planet can be discovered. The incident stellar fluxes in and out of transit being denoted respectively by F_{in} and F_{out}, the ratio of $(F_{out} - F_{in})$ to F_{out}, which is called the transit depth, is equal to the square of the planet-to-star radius ratio. Thus, the radius of the planet can be measured from the transit observation. Also, the transit observation can measure the inclination of the orbital plane with respect to the line of sight.

Radial velocity measurement In the presence of a planet, its host star revolves around their common center of mass. The radial-velocity technique detects this motion

of the star by observing Doppler shifts in the star's spectrum, and thereby finds the planet. From the definition of the mass center and the Kepler's third law, one finds that the velocity of the stellar motion is proportional to the planetary mass and inversely proportional to the square root of the planet's semi-major axis. Thus, this detection method can constrain the mass of the planet. Note that the absolute value of the planetary mass is determined, only when the inclination of the orbit with respect to the line of sight is known by some other method.

Therefore, combined radial-velocity and transit measurements determine both the masses and radii (namely, bulk densities) of exoplanets. Note that the mass determination for some of transiting exoplanets was done via transit-timing variation (TTV) measurement, which observes variations in the timing of a transit (e.g., Kepler-11 planets; Lissauer et al. (2011)). Among $\sim$3000 exoplanets detected so far, there are $\sim$300 planets whose masses and radii are both known.

Exoplanets with measured masses and radii tend (1) to orbit close to their host stars (many of them having semi-major axes of < 0.1 AU and orbital period of < 10 days) and (2) to be massive and/or large in size, because of the observational selection bias. As explained above, the radial-velocity measurement observes stellar motion, which is due to gravitational pull by planetary companions. Thus, planets that are more massive and orbiting closer to their host stars are easier to detect by this method. For planetary transit to occur as seen from Earth, the exoplanet must have the orbit near the plane of the star and Earth. The probability for transit to occur (called a transit probability) is almost equal to the ratio of the stellar to orbital radii for a randomly-oriented planet (Borucki & Summers, 1984) and thus higher for planets with shorter orbital periods. Also, the time interval of transits for short-period planets are short compared to those for long-period planets, as a matter of course. In addition, since the transit depth is the square of the planetary-to-stellar radius, planets with larger relative radii are easier to detect via transit measurement.

From the measured mass and bulk density of an exoplanet, one can infer theoretically the interior structure and internal (or bulk) composition of the planet. In our solar system, there are three types of planets with different compositions: (1) The planets of large mass ($\gtrsim 100$ Earth masses) and low bulk density ($\sim$1 g/cm^3), namely Jupiter and Saturn, are composed of an ice/rock core and a massive H/He envelope, (2) the planets with intermediate mass (~ 10 Earth masses) and bulk density ($\sim$1-2 g/cm^3), namely Neptune and Uranus, are composed of an ice/rock core and a H/He envelope that is

much thinner than those of Jupiter and Saturn, and (3) the planets with small mass ($\lesssim$ 1 Earth mass) and high bulk density ($\sim$4-6 g/cm^3), namely the four terrestrial planets, are mainly composed of rock with tenuous or no atmospheres. Beyond the solar system, most of the exoplanets found in early phase are large in size like Jupiter and close to their host stars (i.e., so-called hot Jupiters) because of the effects of detection bias described above. Detection of smaller planets has become possible, as the observational techniques advance. In particular, exoplanets whose masses are two to ten times larger than that of Earth (called super-Earths) have attracted attention recently, because no planet in such a mass range is present in our solar system, so that we have no exact idea of the composition of super-Earths.

Only from the mass and bulk density of a planet, however, the bulk composition of the planet cannot be determined uniquely, because mixtures with different compositions yield the same mass-radius (or mass-density) relationship. This degeneracy in composition is a serious issue especially in the case of small-size and low-mass planets such as super-Earths. For example, a high-density (i.e., rocky) body surrounded by a H/He envelope is indistinguishable from a low-density (i.e., icy) planet.

The issue of compositional degeneracy affects our understanding of not only the diversity of exoplanets, but also the origin of planets and planetary systems. In the example above, removing the degeneracy provides an important clue to understanding the orbital migration of super-Earth-mass planets, which is one of the uncertain processes relevant to planet formation. If a transiting planet is the latter type, namely an icy planet, the planet must have formed beyond the snowline. This means that the planet is likely to have experienced orbital migration from beyond the snowline to the present location close to its host star. In contrast, if the planet is the former type, namely a rocky planet surrounded by a H/He atmosphere, it is possible that the planet formed in situ. Rocky material is available in hot/warm regions of a protoplanetary disk; also, the H/He atmosphere can be captured from the surrounding disk. Thus, since the compositions of low-mass, relatively low-density, short-period planets contain information about their origins, it is important to remove the compositional degeneracy. A key constraint to remove the compositional degeneracy is the composition of planetary atmosphere.

1.2   Observations of atmospheric compositions of exoplanets

Atmospheric compositions of exoplanets can be measured with indirect methods such as transit and secondary eclipse observation; the latter detects an apparent decline in stellar brightness that happens when a planet passes *behind* its host star as seen from the observer. Note that although the composition of the atmosphere of exoplanets such as HR 8799 (Barman et al., 2011) has been constrained by direct imaging, possible targets are currently limited only to large, bright and quite long-period planets (e.g. Marois et al., 2008; Kalas et al., 2008).

During a transit, a fraction of the incident light from the star passes through the narrow annulus of the planetary atmosphere. Since the amount of absorption and scattering by molecules and clouds in the planetary atmosphere is different depending on wavelength, the transit depth depends on the wavelength. In other words, from the wavelength-dependent transit depth obtained by doing transit observations at multiple wavelengths, one can infer the atmospheric composition. This type of observation is often called multi-wavelength (or multi-band or multi-color) transit observation, and the spectrum thus obtained is called a transmission spectrum. On the other hand, during a secondary eclipse, one can obtain the emission spectrum of the planet, which contains the information about its temperature structure and atmospheric composition.

Characterization of exoplanetary atmospheres via transit observation began in 2002. In 2000, the first transiting exoplanet, HD 209458b, was found (Charbonneau et al., 2000; Henry et al., 2000). Soon after this discovery, Charbonneau et al. (2002) detected sodium in the atmosphere of HD 209458b by the transit observation at the D-line. Since then, atmospheric characterization has been done for several exoplanets. Recently, thanks to advance in observational techniques, atmospheric characterization for relatively small planets has become possible via multi-wavelength transit observations. Typical examples are GJ 1214b of mass 6.26 $M_\oplus$ and radius 2.80 $R_\oplus$ (Charbonneau et al., 2009; Anglada-Escudé et al., 2013), GJ 3470b of 13.73 $M_\oplus$ and 3.88 $R_\oplus$ (Biddle et al., 2014), and GJ 436b of 25.4 $M_\oplus$ and 4.10 $R_\oplus$ (Lanotte et al., 2014). Interestingly, transmission spectra of those planets observed so far cannot be explained only by absorption and scattering (i.e., extinction) of gaseous molecules in the atmospheres.

GJ 1214b is a super-Earth whose atmosphere has been probed most. Recent multi-wavelength transit observations show a relatively featureless or flat spectrum from the optical (e.g. Narita et al., 2013b; Nascimbeni et al., 2015a) to near-infrared (e.g. Krei-

dberg et al., 2014), although de Mooij et al. (2012) made a tentative report on an increase in the transit depth in the optical. This raises the possibility that particles such as clouds and haze are present in the atmosphere, because those particles obscure molecular absorption features. (In this study, we refer to thermochemical condensates as "clouds" and photochemical products as "haze".) Also, its transmission spectrum in the near-infrared is too flat to be explained even by a CO_2-dominated atmosphere (Kreidberg et al., 2014). In addition to GJ 1214b, GJ 436b is also reported as showing a featureless spectrum in the near-infrared by Knutson et al. (2014), suggesting the presence of a cloudy/hazy layer.

GJ 3470b is reported to show a bit more complicated spectrum, which includes a steep spectral slope[1] in the optical (Fukui et al., 2013; Nascimbeni et al., 2013; Biddle et al., 2014; Dragomir et al., 2015; Awiphan et al., 2016a) and is relatively featureless or flat in the near-infrared (Crossfield et al., 2013; Ehrenreich et al., 2014). A modest amount of cloud/haze particles, if present, tend to steepen the spectral slope in the optical (Lecavelier Des Etangs et al., 2008), while a thick cloud/haze obscures molecular and atomic absorption features, flattening the spectrum.

Though the number of samples is still small, cloud/haze may be commonly present and bring about a diversity of spectra (Sing et al., 2016). Recently, Stevenson (2016) and Heng (2016) explored the diversity in transmission spectra known so far by quantifying the degree of cloudiness in atmospheres of transiting exoplanets from their spectra. Both two studies reported the trend that cooler planets were more likely to have cloudy/hazy atmospheres. Since the existence of clouds/haze obscures predicted spectral features of molecular absorption, for constraining the atmospheric composition of transiting exoplanets with clouds/haze in their atmospheres, it is necessary to understand the effects of clouds/haze on transmission spectra first.

Currently, the number of low-mass exoplanets for which atmospheric characterization is feasible is still small. However, a great number of possible targets will be detected within a decade by scheduled exoplanet missions, as described later.

---

[1]The steep slope in the optical is sometimes referred to as the Rayleigh scattering slope in the literature. However, one can never conclude that the slope is due to Rayleigh scattering from an observed spectral slope alone (see Heng, 2016).

1.3 Previous theoretical transmission spectrum models of exoplanet atmospheres with clouds or haze

Components of cloud/haze particles floating in planetary atmospheres are different depending on planetary environment such as temperature, atmospheric composition, atmospheric circulation, stellar irradiation, etc. For example, in the atmosphere of planets and moons in our solar system, various kinds of cloud or haze have been observed (see Morley et al., 2013, and references therein): H_2SO_4 cloud on Venus, H_2O and CO_2 clouds on Mars, NH_3 cloud on Jupiter, NH_3 and H_2O clouds on Saturn, CH_4 cloud and haze on Titan, and CH_4-derived clouds and haze on Uranus and Neptune.

The above three exoplanets GJ 1214b, GJ 3470b, and GJ 436b are close-in super-Earths/mini-Neptunes orbiting low-mass stars (called M stars) whose radii are $\lesssim 0.7$ solar radii and effective temperatures are $\sim$ 2500–3500 K. Their atmospheric temperatures are typically $\sim$ 500 to 1000 K. From their relatively large radii, their atmospheres are thought to contain hydrogen. Also, since orbiting close to their host stars, those planets are exposed to intense UV radiation from their host stars. In such warm, highly-UV irradiated environments, hydrocarbon haze is formed easily through photochemical reactions triggered by photo-dissociation of methane, provided the atmospheres are reducing enough that CH_4 rather than CO dominates the atmospheric carbon chemistry (e.g. Yung et al., 1984).

Some studies so far addressed theoretical modeling of transmission spectra of hydrogen-rich atmospheres in such environments, considering the effect of haze in the atmosphere. Howe & Burrows (2012) is the first to quantify the effects of haze on transmission spectrum of GJ 1214b's atmosphere. They assumed an atmospheric layer containing haze particles. They defined the haze layer using four parameters that include single values of the number density and size of haze particles and the pressures of the upper and lower edges of the haze layer. (They also considered the existence of clouds, below which transmitted light is cut off completely, regardless of wavelength.) Comparing the theoretical spectra derived with various haze/cloud properties and molecular compositions to the observed transmission spectrum of GJ 1214b, they demonstrated that a hydrogen-rich atmosphere with the haze layer could explain the observed transmission spectrum, provided appropriate sets of the haze parameters were chosen.

The same way for incorporating the effect of a haze layer was adopted by Ehrenreich et al. (2014), who modeled transmission spectra of GJ 3470b's atmosphere and then compared them with the observed one, including their own observations done with

Hubble Space Telescope (HST). They found no solution that reproduced the observed steep spectral slope in the optical, simultaneously with the observed flat spectrum in the near-infrared. Instead, they concluded that both of the observed features in the optical and near-infrared could be matched by a hydrogen-rich atmosphere covered with not haze, but clouds, which they modeled in the same way as Howe & Burrows (2012). This was because they only considered the cases where particle densities were modest for haze, while large particle densities were considered for clouds such that below the cloud layer, transmitted light was cut off completely, regardless of wavelength.

In contrast to the above theoretical modeling that *assumes* the altitude and thickness of the haze layer, Morley et al. (2013) tried to determine those properties by doing photochemical calculations. They derived numerically the vertical distributions of the photochemically-produced hydrocarbons, HCN, C_2H_2, C_2H_4, and C_2H_6, which are precursors of haze particles. Assuming that haze particles formed from a given fraction of the precursors, which they regarded as a parameter (called the haze-forming efficiency), they determined the distribution of haze particles and then modeled the transmission spectrum of GJ 1214b's atmosphere with assumed particle size and number density. (In their modeling, they used the opacity data of soot instead of those of tholin, which Howe & Burrows (2012) and Ehrenreich et al. (2014) used.) They found that the observed transmission spectra of GJ 1214b could be explained by the haze particles with the assumed size of 0.01 to 0.25 μm and the assumed haze-forming efficiency of 1–5 %, although there remained a possibility of clouds composed of KCl and ZnS.

1.4   Purpose of this thesis

As mentioned above, the atmospheric composition provides a valuable clue to understanding the bulk composition and origin of exoplanets. A promising method for atmospheric characterization is multi-wavelength transit observation. An important issue we have faced is to understand the effects of cloud/haze on transmission spectra. Indeed, some recent studies show that cloud/haze may be commonly present and could bring about a diversity of spectra (Sing et al., 2016). Since cloud/haze could obscure spectral features of molecular absorption, it is necessary to understand the effects of cloud/haze on transmission spectra first.

The previous studies we have mentioned above certainly demonstrated that theoretical transmission spectra of hazy atmospheres matched the corresponding observations for appropriate choices of the haze parameters. However, they did not access the viability of those assumed haze properties sufficiently from a physical point of view. It is uncertain whether the particles with the sizes they assumed can really exist in spite of growing larger, sedimenting downward, or being diffused upward at the steady state, whether the particle number densities they assumed is plausible (see Chapter 2). In particular, all of the previous studies assumed the single particle size throughout the atmosphere. However, the size of the particles would vary with the altitude because of the particle growth. Also, particles of various size might exist at a certain altitude. In addition, although the previous studies found that various haze parameters being chosen, one can generate variation in transmission spectra, it remains to be clarified what yields such a variety of haze properties.

In this doctoral thesis, we focus on photochemically-produced hydrocarbon haze as a possible candidate for the cloud/haze, while some other constituents are assumed in previous studies. As mentioned in § 1.2, the number of the targets for multi-wavelength transit observations is currently limited. However, it is considered to increase thanks to the launch of the first-ever space all-sky survey satellite, TESS (Transiting Exoplanet Survey Satellite) in June 2018. Most of exoplanets that will be detected by such missions are warm ($\sim$ 500 to 1000 K) exoplanets with relatively hydrogen-rich, reducing atmospheres around M stars and those planets would be the primary targets for atmospheric characterization with the near-future high-precision telescopes such as James Webb Space Telescope (JWST) scheduled to be launched in late spring of 2019. This is because M dwarfs are most abundant in the solar neighborhood (e.g., Cantrell et al., 2013) and also favorable for observation because of their relatively small radii; close-in exoplanets around M dwarfs have typical temperatures of $\sim$ 500 to 1000 K and

from the relatively large radii of the planets, their atmospheres are thought to contain hydrogen. Also, since those planets orbit close to their host stars, they are exposed to intense UV radiation from their host stars. In such warm, highly-UV irradiated reducing environments, hydrocarbon haze is formed easily through photochemical reactions triggered by photo-dissociation of methane (e.g. Yung et al., 1984). From the above reason, we focus on hydrocarbon haze in this thesis.

As we have mentioned, transmission spectra so far observed seem to be diverse (Sing et al., 2016). Observation shows that M dwarfs are diverse in UV emission intensity (Linsky et al., 2013). Since haze is formed through photochemical reactions triggered by photo-dissociation of CH_4, the transmission spectrum of an exoplanet atmosphere with such haze should depend on the UV intensity of its host star. Thus, the diversity in UV intensity of M dwarfs can be considered to bring about the diversity of transmission spectra, which no previous theoretical studies have explored.

The purpose of this doctoral thesis is to explore what diversity of transmission spectra of exoplanets are brought from different production rates and distributions of the monomers of haze particles, which are related to the variety in UV intensities of M dwarfs. To do so, we develop a new numerical code from scratch for simulating transmission spectra of transiting exoplanet atmospheres, which include calculations of thermo- and photo-chemistry, particle growth, opacities of gases and particles, and wavelength-dependent atmospheric absorption of stellar radiation. Then, we model the haze formation processes, assuming hydrogen-dominated atmospheres of close-in warm ($\lesssim$ 1000 K) exoplanets, derive the realistic distribution of the size and number density of haze particles, and explore its impacts on transmission spectra, which were not investigated previously. Then, we explore the production rate of haze monomers and resultant transmission spectra of the atmospheres of currently observable warm exoplanets including GJ 1214b, GJ 3470b, and GJ 436b.

The rest of this doctoral thesis is organized as follows. In Part I, we describe the methodology for developing our transmission spectrum models and, then, demonstrate the sensitivity of transmission spectra to the production rate of haze monomers, which relates to the amount of UV irradiation from the host star, and other model parameters, namely, eddy diffusion coefficient, C/O ratio, temperature structure, and monomer size. In Part II, we explore the production rate of haze monomers in the atmospheres of GJ 1214b, GJ 3470b, and GJ 436b, by comparing our developed transmission spectrum models to the observed spectra of those planets. Also, we apply our models to Titan, a moon of the Saturn and known to have hazes in its atmosphere, and compare the transmission spectrum of Titan we calculate with that Robinson et al. (2014) constructed

from the solar occultation observations. Finally, we conclude this thesis.

Part I

Theoretical Modeling of Transmission Spectra of Exoplanet Atmospheres with Hydrocarbon Haze

Chapter 2

Introduction of Part I

As described in Chapter 1, in Part I, we develop transmission spectrum models of warm transiting planets with hydrogen-rich atmospheres by incorporating the effects of the size and number density distributions of hydrocarbon haze that are determined through the production, growth, and settling processes of the particles. First, precursor molecules of haze particles (i.e., higher-order hydrocarbons, which we call haze precursors, hereafter) are created through photochemical reactions triggered by UV photodissociation of CH_4. Then, aggregation of the haze precursors results in haze particles of small size, which are called monomers. Note that the size of monomers in the atmosphere of Titan was reported as 40 ± 10 nm from observations (Tomasko et al., 2009). Those monomers diffuse and settle downward. Also, collisional growth of the haze particles takes place. Once the haze particles go down into hot, convective regions, they are likely to be thermodynamically dissociated and evaporated to be CH_4 again, which can be diffused upward to be the source of haze precursors.

The rest of this part is organized as follows. In Chapter 3, we describe the assumptions, equations, and calculation methods for the size and number density distributions of haze particles and generating the transmission spectra. In Chapter 4, we investigate the vertical distribution of haze particles and its effects on the transmission spectra. Also, we investigate the dependence of the vertical distribution of haze particles and the gaseous species, and the transmission spectrum on the model parameters, namely, the production rate of haze monomers, which is related to UV irradiation intensity from the host star, eddy diffusion coefficient, C/O ratio, temperature structure, and monomer size. In Chapter 5, to gain a deeper understanding of the effect of the haze particle distribution on transmission spectrum, we calculate the particle growth and transmission spectra with a characteristic-size approximation and then compare the

results with those obtained in Chapter 4. Finally, we discuss several effects to be examined and implications for future characterization of exoplanets in Chapter 6 and then summarize this part in Chapter 7.

Chapter 3

Model and Method Description

In § 3.1, we first describe the method of coupling photochemical and particle growth models. We perform photochemical calculations to derive the vertical distribution of haze precursors in a similar way to Morley et al. (2013) (§ 3.2). Then, using the obtained vertical profiles of the precursors, we calculate the growth and settling of haze particles in the atmosphere to derive the steady-state distributions of the size and number density of the haze particles (§ 3.3). Finally, we calculate the extinction opacities of the gases and particles (§ 3.4) and model transmission spectra of the atmospheres with obtained properties of haze (§ 3.5). In § 3.6, we summarize the calculation procedure, and the model parameters and their values that we use in our simulations.

Before explaining the details of the above three modules, we first describe the assumptions and treatments made in all the modules. We make an reasonable assumption that the atmosphere is in hydrostatic equilibrium and composed of ideal gases. While considering the altitude variation of gravity for hydrostatic structure, we neglect the effect of curvature, which would yield only a small difference compared to other large uncertainties in model parameters, and assume plane-parallel structure in the photochemical and particle growth calculations. Because our focus is on the effects of the size distribution of haze particles on transmission spectra, we assume, for simplicity, that the atmospheric structure is spherically symmetric. In reality, since close-in exoplanets tend to be tidally locked, the structure may be far from spherically symmetric.

3.1   Treatment of monomers

In this section, we describe our treatment of monomers, namely, the method of coupling photochemical and particle growth models. We assume that monomers form in situ

from the precursor molecules of haze particles. We assume HCN and C_2H_2 as the precursor molecules. While higher-order hydrocarbons may have to be also included as the precursors, previous studies (e.g., Morley et al., 2013) showed that HCN and C_2H_2 are the most dominant hydrocarbons photochemically produced in solar abundance atmospheres with temperature of 500-1000 K. We calculate the vertical profile of the mass production rate of monomers according to the distribution of the two molecules. We consider that the mass production rate of monomers with volume v_1 and mass $m_{p,1}$, which means the total numbers of monomers produced per unit volume per unit time, at altitude z is given by

$$p\left(v_1, z\right) = \frac{\left[f_{\mathrm{HCN}}\left(z\right) + f_{\mathrm{C_2H_2}}\left(z\right)\right] N\left(z\right)}{\int_0^\infty \left[f_{\mathrm{HCN}}\left(z'\right) + f_{\mathrm{C_2H_2}}\left(z'\right)\right] N\left(z'\right) dz'} \frac{\dot{M}}{m_{p,1}}, \tag{3.1}$$

where f_{HCN} and $f_{\mathrm{C_2H_2}}$ are the volume mixing ratios of HCN and C_2H_2, respectively, N is the total number density of the atmospheric gas molecules, and $\dot{M}$ is the total mass production rate of monomers throughout the atmosphere and its physical unit is mass/area/time. As for $\dot{M}$, we consider two cases, UV-limited case (§ 3.1.1) and Carbon-limited case (§ 3.1.2). In UV-limited case, we assume that $\dot{M}$ is proportional to the incident stellar Lyman-alpha ($Ly\alpha$) flux at the planet's orbital distance because monomer production is relevant to UV photodissociation and uses Titan for reference following Trainer et al. (2006). In Carbon-limited case, we assume that $\dot{M}$ is equal to the total mass production rate of carbon throughout the atmosphere by the photodissociation of haze precursors, HCN and C_2H_2. Below, we describe each case in detail.

3.1.1   UV-limited case

For the production mechanism of haze monomers, Trainer et al. (2006) proposed two mechanisms. One, which they called Mechanism A, is such that haze monomers are produced predominantly by photodissociation of hydrocarbon intermediate molecules, which is the product of photodissociation of CH_4;

$$CH_4 + h\nu \quad \rightarrow \quad A \tag{3.2}$$
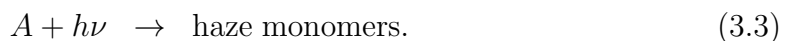
$$A + h\nu \quad \rightarrow \quad \text{haze monomers.} \tag{3.3}$$

In this mechanism, the production rate of monomers, $\dot{m}$ is proportional to the square of the light intensity, I, and proportional to the CH_4 concentration, n_{CH_4};

$$\dot{m} \propto I^2 n_{CH_4}. \tag{3.4}$$

The other, which they called Mechanism B, is such that haze monomers are produced mainly by thermochemical reactions between multiple intermediates;

$$CH_4 + h\nu \quad \rightarrow \quad A \tag{3.5}$$

$$A + A \quad \rightarrow \quad \text{haze monomers.} \tag{3.6}$$
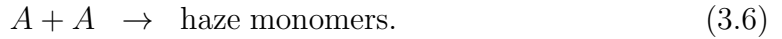
In this mechanism, $\dot{m}$ is proportional to I and n_{CH_4};

$$\dot{m} \propto I n_{CH_4}. \tag{3.7}$$

Considering the above two cases, Trainer et al. (2006) proposed the following equation for $\dot{M}$ using Titan for reference:

$$\dot{M} = \zeta \left(\frac{I_{Ly\alpha}}{I_{Ly\alpha,Titan}} \right)^q \left(\frac{f_{CH_4}}{f_{CH_4,Titan}} \right) \dot{M}_{Titan}, \tag{3.8}$$

where $I_{Ly\alpha}$ and $I_{Ly\alpha,Titan}$ are the incident stellar Lyman-alpha (Lyα) flux at the planet's orbital distance and the incident solar Lyα flux at Titan's orbit, respectively. They used the Lyα intensity because the primary wavelength for CH_4 photolysis is expected at the Lyα wavelength. f_{CH_4} and $f_{CH_4,Titan}$ are the volume mixing ratios of CH_4 in the atmospheres of the planet and Titan, respectively. $\dot{M}_{Titan}$ is the mass production rate in the Titan's atmosphere. q is an exponent depending on the production mechanisms of haze monomers, 2 for Mechanism A and 1 for Mechanism B. The factor, ζ, was added to account for the effect of the C/O ratio. From their experiments, they determined $\zeta = 1.5$ for C/O = 1 case like early Earth. $\zeta = 1$ for CH_4-only case, like Titan.

Simplifying Eq.(3.8), we use the following equation for $\dot{M}$ in the UV-limited case;

$$\dot{M}_{UV} = \beta \frac{I_{Ly\alpha}}{I_{Ly\alpha,Titan}} \dot{M}_{Titan}. \tag{3.9}$$

Although both linear and quadratic dependences of $\dot{M}$ on $I_{Ly\alpha}$ are proposed, there is still room for discussion to determine which relationship is appropriate. Because the

relationship is totally uncertain for exoplanet atmospheres, we have adopted the linear relationship for simplicity ($q = 1$). Also, for simplicity, we have ignored the dependence of $\dot{M}$ on CH_4 abundance and C/O ratio, and added a numerical parameter β in the above equation to also account for the uncertainty of the intensity-relationship. Thus, the value of β can change according to the intensity-relationship, CH_4 abundance, and C/O ratio, and $\beta = 1$ for Titan's atmospheric environment. Although there are several factors for uncertainty of β, we regard the Lyα intensity as the main uncertainty, because the current and future targets, M dwarfs, are diverse in UV emission intensity. We explore the dependence of the distribution of haze particles and transmission spectra on β (i.e., the UV irradiation intensity), by changing its value by several orders of magnitude. When we vary β, we also vary the intensities of the actinic flux at all the wavelengths according to β. We adopt 1×10^{-14} g cm^{-2} s^{-1} for $\dot{M}_{\mathrm{Titan}}$, since microphysical models, photochemical models, and laboratory simulations all imply that the production rate of the monomers on Titan is in the range between 0.5×10^{-14} and 2×10^{-14} g cm^{-2} s^{-1} (McKay et al., 2001). Also, we use 6.2×10^9 photons cm^{-2} s^{-1} for $I_{\mathrm{Ly\alpha,Titan}}$ (Trainer et al., 2006).

3.1.2   Carbon-limited case

In this case, we assume that $\dot{M}$ is equal to the total mass production rate of carbon throughout the atmosphere by the photodissociation of haze precursors, HCN and C_2H_2, namely, photochemical reactions P13 and P16 (see § 3.2 and Table D.2), $\dot{M}_{\mathrm{C}}$. We calculate $\dot{M}_{\mathrm{C}}$ by integrating the production rate of carbon by the reactions P13 and P16 from 10 bar to top of the atmosphere at the steady-state. Same as in the UV-limited case (§ 3.1.1), we explore the dependence of the distribution of haze particles and transmission spectra on β (the UV irradiation intensity), by changing its value by several orders of magnitude. Because haze particles do not consist of only carbon and all the products from the dissociation of the precursor molecules do not result in haze monomers, in reality, the value of $\dot{M}$ is expected to be different from that of $\dot{M}_{\mathrm{C}}$. However, we consider this case as one ultimate case.

3.2   Photochemical model

Various photochemical models have been constructed for terrestrial and gaseous planets. Allen et al. (1981)'s model is for studying the vertical transport and photochemistry in the Earth's mesosphere and lower thermosphere (50-120 km). Using their model,

they derived the distributions of long-lived species and compared them with observations. Line et al. (2011) introduced their photochemical model to explore the chemistry of warm gaseous exoplanetary atmospheres for explaining the observed depletion of methane in the atmosphere of GJ 436b. Venot et al. (2012) released a large chemical network applying combustion models, which were validated over the temperature and pressure ranges relevant to hot Jupiter atmospheres. After that, they expanded their networks to hydrocarbons up to six-order (Venot et al., 2015). Hu et al. (2012) presented the photochemical model for terrestrial exoplanets applicable for all types of atmospheres, from reducing to oxidizing. They presented the results for three benchmark cases of atmospheric scenarios from reducing to oxidizing for terrestrial exoplanets. Tsai et al. (2017) presented an open-source photochemical model for hot exoplanetary atmospheres, VULCAN, which they validated by reproducing the results of Moses et al. (2011). In this study, we newly develop a photochemical model to derive the vertical distribution of haze precursors.

3.2.1 Model description

The one-dimensional continuity-transport equation that governs the change in the number density of species i, n_i, is written as (Yung & Demore, 1999)

$$\frac{\partial n_i}{\partial t} = P_i - L_i - \frac{\partial \Phi_i}{\partial z}, \tag{3.10}$$

where t and z are the time and the altitude, respectively, P_i and L_i are the production and loss rates of species i due to photochemical and thermochemical reactions, respectively, and Φ_i is the vertical transport flux of species i. We assume that the vertical transport occurs by eddy diffusion and ignore molecular diffusion. The eddy diffusion flux is given by (Yung & Demore, 1999)

$$\Phi_i = -K_{zz} N \frac{\partial f_i}{\partial z}, \tag{3.11}$$

where K_{zz} is the eddy diffusion coefficient, N is the total number density of the atmospheric gas molecules, and $f_i \equiv n_i/N$ is the mixing ratio of species i. Here, we have used the definition of atmospheric scale height and the ideal gas law.

We include the following 29 chemical species composed of the five elements, C, H, O, N, and He: O, O_2, H_2O, H, OH, CO_2, CO, HCO, CH_4, CH_3, CH_3O, CH_3OH, CH, CH_2, C, C_2, C_2H, C_2H_2, N, N_2, NH, NH_2, NH_3, CN, HCN, H_2, He, $O(^1D)$, and

[1]CH_2. These species are the ones considered in the photochemical models of Kopparapu et al. (2012), who studied the atmosphere of the hot Jupiter WASP-12b, except for H_2CO and CH_2OH, which we do not consider. Since the main focus of this study is on calculating the size and spatial distributions of haze particles and evaluating their impacts on resultant transmission spectra, we simply assume that the haze precursors form from C_2H_2 and HCN, in the same way as Morley et al. (2013), and do not include hydrocarbons such as C_2H_4 and C_2H_6. They showed that HCN and C_2H_2 are the most dominant hydrocarbons phtochemically produced in solar-abundance atmospheres with temperature of 500-1000 K, although there remains uncertainties for the treatment of higher-order hydrocarbons (see, e.g., Zahnle et al., 2016). Also, we do not consider sulphur compounds, because they are scarcely involved in reactions with hydrocarbons of interest here. As both the opacities of H_2S and OCS are much smaller compared to those of H_2O and CH_4 according to sulphur's small elemental abundance, it is sure that they have little impact on the transmission spectrum. We do not consider Na and K because they condense as Na_2S and KCl clouds, respectively, and settle downward in the temperature range of interest ($\lesssim$ 1000 K) (Morley et al., 2013).

We adopt 154 thermochemical reactions from the reaction list of Hu et al. (2012). All the thermochemical reactions and their rate coefficients are listed in Table C.1. We have chosen the reactions that involve only some of the above 31 species, although the reaction list of Hu et al. (2012) contains more reactions. We also consider their reverse reactions using the method described in Visscher & Moses (2011). Thus, in total, we consider 308 thermochemical reactions. For the calculation of the Gibbs free energy of each species, which is needed to calculate the equilibrium constants (the ratios of forward to reverse reaction rate coefficients), we use the polynomial coefficients for calculating enthalpies of formation, entropies, and heat capacities from the Third Millennium Ideal Gas and Condensed Phase Thermochemical Database for Combustion [1]. Although some rate coefficients are invalid in the temperature range considered in this study, we use them outside their temperature range due to the lack of data and/or theory.

For photochemistry, we consider 16 reactions listed in Table D.2. Likewise, all the reactions are extracted from the reaction list of Hu et al. (2012) if the reaction involves only some of the above 31 species. Photodissociation rate of species i (i.e., the number

---

[1]http://garfield.chem.elte.hu/Burcat/burcat.html

of atoms or molecules dissociated per unit time) at altitude z, $J_i(z)$, is written as

$$J_i(z) = \frac{1}{2} \int_0^\infty q_i(\lambda)\,\sigma_i(\lambda)\,F(z,\lambda)\,d\lambda, \tag{3.12}$$

where λ is the wavelength, $q_i(\lambda)$ and $\sigma_i(\lambda)$ are the dimensionless quantum yield of species i, the absorption cross section (its physical dimension being area) of species i, and $F(z,\lambda)$ is the actinic photon flux per unit area, unit time, and unit wavelength. The factor $1/2$ is needed to account for diurnal variation (see Hu et al., 2012). The references from which we take the data of the quantum yields and absorption cross sections are tabulated in Table E.3 and D.2, respectively, most of which can be downloaded from the website of the MPI-Mainz UV/VIS Spectral Atlas of Gaseous Molecules of Atmospheric Interest[2]. Temperature dependences of absorption cross sections are known for some of the species, but measured only in a temperature range between 200 and 300 K. Thus, following Hu et al. (2012), we calculate the absorption cross sections at 300 K by a linear interpolation with the use of the measured data and use them for temperatures higher than 300 K, namely $\sigma(\lambda, T) = \sigma(\lambda, 300 \text{ K})$, instead of extrapolating beyond 300 K. We consider the attenuation of the actinic flux as

$$F(z,\lambda) = F(\infty,\lambda)\,e^{-\tau(z,\lambda)/\mu}, \tag{3.13}$$

where $F(\infty,\lambda)$ is the actinic flux at the top of the atmosphere at wavelength λ and μ is the cosine of the zenith angle of the star. $\tau(z,\lambda)$ is the optical depth defined by

$$\tau(z,\lambda) = \sum_i^{\mathcal{N}} \int_z^\infty n_i(z')\,\sigma_i(\lambda)\,dz', \tag{3.14}$$

where $\mathcal{N}$ is the number of the species. We do not consider the shiedling due to haze. We assume the zenith angle to be 57.3°, as done in Hu et al. (2012). They found that the mean zenith angle differed depending on the optical depth of interest and concluded that the assuming the zenith angle to be 57°-48°, which corresponded to $\tau = 0.1$-1.0, was appropriate for the one-dimensional photochemical models.

For the boundary conditions, we set the diffusion flux Φ_i as zero for all the species at the upper boundary, while we fix the volume mixing ratios f_i of all the species at the thermochemical equilibrium values at the lower boundary. The exact conditions are, however, uncertain, so that previous studies chose different conditions at both

---

[2]http://satellite.mpic.de/spectral_atlas

boundaries. As for the upper boundary condition, while some studies set the diffusion flux equal to the assumed atmospheric escape flux (e.g., Hu et al., 2012), some studies set $\Phi_i = 0$ for all the species (e.g. Moses et al., 2011; Venot et al., 2012; Tsai et al., 2017). In this study, we choose the latter because the atmospheric escape rate is unknown for exoplanets. As for the lower boundary condition, photochemical modeling of terrestrial planet atmospheres often sets the flux of surface emission and/or deposition at the lower boundary (e.g., Hu et al., 2012). However, gas-rich planets, which we consider in this study, have no rigid surfaces. While some studies adopted zero flux (e.g., Moses et al., 2011; Venot et al., 2012; Tsai et al., 2017), we fix the volume mixing ratios f_i of all the species at thermochemical equilibrium values in a similar way to, for example, Line et al. (2011) and Zahnle & Marley (2014). This is because the gases at deep levels would be in thermochemical equilibrium. While Moses et al. (2011) reported that they did not find any differences in the results between the two types of inner boundary condition, Tsai et al. (2017) found that only the minor ($f_i \lesssim 10^{-9}$) molecules, CO and CO_2, deviated from their thermochemical equilibrium values at relatively cool (1000 K) lower boundary (1000 bar), but major molecules are in thermochemical equilibrium.

3.2.2 Calculation method

The calculation method we use in this study is basically the same as that used in previous works (e.g., Venot et al., 2012; Hu et al., 2012; Tsai et al., 2017). We discretize Eq. (3.10) as

$$\frac{\partial n_{i,j}}{\partial t} = P_{i,j} - L_{i,j} - \frac{\Phi_{i,j+1/2} - \Phi_{i,j-1/2}}{\Delta z_j}, \qquad (3.15)$$

where the subscript j represents the physical quantities in the jth layer and Δz_j is the thickness of the jth layer. We prepare layers with the same thickness Δz and set the pressure at the mid-point altitude of the lowest layer as the lower boundary pressure. From Eq. (3.11), we approximate $\Phi_{i,j+1/2}$ as (e.g., Venot et al., 2012; Hu et al., 2012; Tsai et al., 2017)

$$\Phi_{i,j+1/2} = -K_{zz} N_{j+1/2} \frac{f_{i,j+1} - f_{i,j}}{\Delta z}. \qquad (3.16)$$

To obtain a steady-state solution, we solve Eq. (3.15) implicitly with the use of the solver DLSODES (Hindmarsh, 1982), which is suitable to solve stiff ODE systems such as chemical network calculations (e.g., Grassi et al., 2014). It is based on a backward differentiation formula (BDF), which is also called Gear's method. The most suitable order is chosen within the solver. We set the maximum order allowed to be five. We adopt the values of relative (RTOL) and absolute (ATOL) tolerances as 10^{-4}

and $N_j \times 10^{-15}$, respectively; the value of ATOL differs from layer to layer.

The initial number densities of the species are set to their thermochemical equilibrium values, which we calculate in the following way. A system composed of $\mathcal{N}$ gaseous species being considered, the Gibbs free energy of the system is minimized at equilibrium. The Gibbs free energy at fixed temperature T, pressure P, and composition ξ is written as (Smith & Missen, 1982)

$$G\left(T, P, \xi\right) = \sum_{i=1}^{\mathcal{N}} \xi_i \phi_i, \tag{3.17}$$

where ξ_i and ϕ_i are the molar number and chemical potential of species i, respectively, and $\xi = \{\xi_1, \xi_2, \cdots, \xi_{\mathcal{N}}\}$. The chemical potential of an ideal gas is given by (Smith & Missen, 1982)

$$\phi_i\left(T, P\right) = \phi_i^\circ\left(T\right) + \mathcal{R}T \ln \frac{p_i}{p_{\text{ref}}}. \tag{3.18}$$

Here ϕ° is the standard chemical potential that is a function of T only, p_i is the partial pressure of gaseous species i, p_{ref} is the reference pressure, and $\mathcal{R}$ is the molar gas constant. If a collection of species in the system is given, theoretically permissible chemical reactions can be derived from the law of conservation of mass:

$$\sum_{i=1}^{\mathcal{N}} a_{ki}\xi_i = b_k, \tag{3.19}$$

where a_{ki} is the number of the kth element contained in species i and b_k is the total number of moles of the kth element. The composition that gives the minimum value of the Gibbs free energy is searched for to determine the equilibrium values of the mole fractions of the elements in the system. We assume vertically constant elemental abundance ratios and use the same Gibbs free energy data as that we use for calculation of reverse rate coefficients.

We time-integrate Eq. (3.15) until the system becomes in a steady state. We adopt the criteria of convergence such that all the species of $f_i > 10^{-10}$ vary in mixing ratio by less than 1% in all the layers. The integration is done over a period longer than the eddy diffusion timescale, which we assume as the maximum value of H_j^2/K_{zz} among all the layers at the initial condition. Here, H_j is the atmospheric scale height for layer j. The time step is self-adjusted within the solver so that the estimated local error in $n_{i,j}$ is not larger by an order of magnitude than that of RTOL $\times n_{i,j}$ + ATOL$_j$ ($\equiv$ EWT$_{i,j}$). At each time after calling the solver, for the atmosphere to be in hydrostatic

equilibrium and the total mixing ratio to be unity, we set the output negative number densities to be zero, renormalize the volume mixing ratio of each species, recalculate the total number density at each layer assuming hydrostatic equilibrium, and calculate the number density of each species at each layer. Note that the output negative number densities are not larger by an order of magnitude than EWT.

We compare our photochemical model with the previous thermochemical models for the atmospheres of HD 189733b and HD 209458b presented by Tsai et al. (2017) in AP-PENDIX A and the photochemical models for the WASP-12b's atmosphere presented by Kopparapu et al. (2012) in APPENDIX B. We have confirmed that the abundances of most of the species match those of the previous works within one order of magnitude and the profiles of the molecules are similar except for absolute value. And the differences in abundances for some molecules would not affect our results regarding haze distributions and transmission spectra. We have also confirmed the major trend found in those for GJ 1214b's atmosphere (Miller-Ricci Kempton et al., 2012; Morley et al., 2013) and other low temperature ($\lesssim$ 1000 K) atmospheres (Moses et al., 2013; Venot et al., 2014).

3.3 Particle growth model

We simulate the growth and settling of hydrocarbon haze particles after the production of monomers in the upper atmosphere and determine their steady-state distribution.

3.3.1 Model description

We follow the classical formalism for cloud particle growth (see Jacobson, 2005), which has also been used to simulate haze particle growth in Titan's atmosphere (e.g., Toon et al., 1980, 1992). Note that the same formalism has been also used for dust particle growth in the field of planet formation (see, e.g., Armitage, 2010). Also, as for dust particle growth for brown dwarf atmospheres, there is a series of work (Woitke & Helling, 2003, 2004; Helling & Woitke, 2006), which is different from ours in the point that they considered particle growth due to chemical surface reactions but did not consider the growth due to coagulation.

Adopting a discrete volume grid, one can write the one-dimensional continuity-transport equation for the number density of particles with volume v_i, $n(v_i)$, as (e.g. Lavvas et al., 2010)

$$\frac{\partial n(v_i)}{\partial t} = \quad \frac{1}{2} \sum_{k=1}^{i-1} K(v_k, v_i - v_k) n(v_k) n(v_i - v_k)$$
$$- n(v_i) \sum_{k=1}^{\mathcal{N}} K(v_i, v_k) n(v_k)$$
$$- \frac{\partial \Phi(v_i)}{\partial z} + p(v_i), \tag{3.20}$$

where the subscript denotes the volume grid, $K(v_i, v_k)$ is the coagulation kernel between two particles with volumes v_i and v_k, and $\mathcal{N}$ is the total number of volume bins used in the calculation. The first and second terms on the right-hand side describe the production and loss of the particles of volume v_i (hereafter, the ith particles, for simplicity) due to the coagulation. $\Phi(v_i)$ is the vertical transport flux and $p(v_i)$ is the photochemical production rate of the ith particles, which takes a non-zero value only for v_1, namely monomers. The monomer production rate, $p(v_1)$, is given by Eq. (3.1).

Assuming that the vertical transport occurs by sedimentation and eddy diffusion, one can write $\Phi(v_i)$ as (e.g. Lavvas et al., 2010)

$$\Phi(v_i) = -V_{s,i} n(v_i) - K_{zz} N \frac{\partial (n(v_i)/N)}{\partial z}, \tag{3.21}$$

where $V_{s,i}$ is the sedimentation velocity of the ith particles written as (e.g. Lavvas et al., 2010)

$$V_{s,i} = \frac{2s_i^2 \rho_p g}{9\eta_a} f_{\text{slip},i}.$$
(3.22)

Here, s_i is the radius of the ith particle, ρ_p is the particle internal density, and g is the local gravitational acceleration. η_a is the dynamic viscosity defined as

$$\eta_a = \frac{1}{3} \rho_a \overline{V}_{\text{th}} \lambda_a,$$
(3.23)

where ρ_a is the mass density of the gas, $\overline{V}_{\text{th}}$ is the thermal velocity of the gaseous molecules defined as

$$\overline{V}_{\text{th}} = \sqrt{\frac{8k_{\text{B}}T}{\pi m_a}}$$
(3.24)

with the Boltzmann constant k_{B}, and the temperature T, and the mean mass of gaseous molecules m_a. λ_a is the atmospheric mean free path defined as

$$\lambda_a = \frac{k_{\text{B}}T}{\pi \sqrt{2} P d^2}$$
(3.25)

with the pressure P and the diameter of the gas molecule d. Because H_2 is the most abundant gas species in the atmosphere of interest in this study, we use the diameter of H_2 for the value of d, taken from CRC Handbook of CHEMISTRY and PHYSICS (Haynes, 2012). f_{slip} is the Cunningham slip-flow correction factor given by (Davies, 1945)

$$f_{\text{slip},i} = 1 + 1.257 K_{n,i} + 0.400 K_{n,i} \exp\left(-1.10/K_{n,i}\right),$$
(3.26)

where $K_{n,i}$ is the Knusden number defined as $K_{n,i} \equiv \lambda_a/s_i$.

As for coagulation, we consider two rate-controlling processes which include the Brownian diffusion and gravitational collection. The latter is the collisional process that occurs as a result of difference in sedimentation velocity between different size particles. The total kernel is assumed to be the sum of the two kernels, namely

$$K\left(v_i, v_k\right) = K_{\text{BD}}\left(v_i, v_k\right) + K_{\text{GC}}\left(v_i, v_k\right).$$
(3.27)

The Brownian collision kernel for the ith and kth particles, $K_{\text{BD}}\left(v_i, v_k\right)$, can be written

as (Jacobson, 2005)

$$K_{\text{BD}}\left(v_i, v_k\right) = \frac{4\pi\left(s_i + s_k\right)\left(D_{p,i} + D_{p,k}\right)}{\frac{s_i + s_k}{s_i + s_k + \sqrt{\delta_i^2 + \delta_k^2}} + \frac{4\left(D_{p,i} + D_{p,k}\right)}{\sqrt{\overline{v}_{\text{th},i}^2 + \overline{v}_{\text{th},k}^2}\left(s_i + s_k\right)}} \tag{3.28}$$

with

$$\delta_i = \frac{\left(2s_i + \lambda_{p,i}\right)^3 - \left(4s_i^2 + \lambda_{p,i}^2\right)^{3/2}}{6 s_i \lambda_{p,i}}. \tag{3.29}$$

$D_{p,i}$ and $\overline{v}_{\text{th},i}$ are the diffusion coefficient and thermal velocity for the ith particle, respectively. These parameters are given as

$$D_{p,i} = \frac{k_{\text{B}}T}{6\pi s_i \eta_a} f_{\text{slip},i} \tag{3.30}$$

and

$$\overline{v}_{\text{th},i} = \sqrt{\frac{8 k_{\text{B}} T}{\pi m_{p,i}}} \tag{3.31}$$

with the particle mass $m_{p,i}$. $\lambda_{p,i}$ is the particle's mean free path written as

$$\lambda_{p,i} = \frac{8 D_{p,i}}{\pi \overline{v}_{\text{th},i}}. \tag{3.32}$$

The gravitational collection kernel for the ith and kth particles, $K_{\text{GC}}\left(v_i, v_k\right)$, can be written as (Jacobson, 2005)

$$K_{\text{GC}}\left(v_i, v_k\right) = E_{\text{coll},i,k} \pi \left(s_i + s_k\right)^2 \left|V_{s,i} - V_{s,k}\right|, \tag{3.33}$$

where $E_{\text{coll},i,k}$ is a collision efficiency given by

$$E_{\text{coll},i,k} = \frac{60 E_{\text{V},i,k} + E_{\text{A},i,k} \text{Re}_i}{60 + \text{Re}_i} \quad \left(s_i \geq s_k\right) \tag{3.34}$$

$$E_{\text{V},i,k} = \begin{cases} \left[1 + \frac{0.75 \ln\left(2\text{St}_{i,k}\right)}{\text{St}_{i,k} - 1.214}\right]^{-2} & \left(\text{St}_{i,k} > 1.214\right) \\ 0 & \left(\text{St}_{i,k} \leq 1.214\right) \end{cases} \tag{3.35}$$

$$E_{\text{A},i,k} = \frac{\text{St}_{i,k}^2}{\left(\text{St}_{i,k} + 0.5\right)^2}. \tag{3.36}$$

Here, Re_i is the Reynolds number written as

$$\mathrm{Re}_i = \frac{2s_i V_{s,i}}{\nu_a} \tag{3.37}$$

with the kinematic viscosity

$$\nu_a = \frac{\eta_a}{\rho_a} \tag{3.38}$$

and $\mathrm{St}_{i,k}$ is the Stokes number written as

$$\mathrm{St}_{i,k} = \frac{V_{s,k}|V_{s,i} - V_{s,k}|}{s_i g} \ \ (s_i > s_k). \tag{3.39}$$

$E_{\mathrm{coll},i,k}$ simplifies to $E_{\mathrm{V},i,k}$ when $\mathrm{Re}_i \ll 1$ and to $E_{\mathrm{A},i,k}$ when $\mathrm{Re}_i \gg 1$. The inclusion of $E_{\mathrm{coll},i,k}$ is important for lower atmosphere but negligible for upper atmosphere.

When we simulate the particle growth with the discretized size distribution, we face the problem that the coagulation between the ith and kth particles $(v_i > v_k)$ produces particles of an intermediate volume,

$$v_{i,k} = v_i + v_k. \tag{3.40}$$

To satisfy the conservations of the mass and the particle numbers at the same time, we partition this intermediate-volume particle into the two volume bins, v_l and v_{l+1} $(v_l < v_{i,k} < v_{l+1})$, with fractions γ_l and γ_{l+1}, respectively. Unless v_l is the largest volume bin, these fractions can be written as

$$\gamma_l = \frac{v_{l+1} - v_{i,k}}{v_{l+1} - v_l} \tag{3.41}$$

and

$$\gamma_{l+1} = 1 - \frac{v_{l+1} - v_{i,k}}{v_{l+1} - v_l}. \tag{3.42}$$

If v_l is the largest volume bin, we cannot partition the intermediate particle but just put it into the largest volume bin v_{l+1}, although the mass conservation is not satisfied. We specify the volume ratio of two adjacent bins in § 3.6.

Finally, the boundary conditions for Eq. (3.20) are given as follows. As the lower boundary conditions, we consider that all the particles are lost with the larger of the sedimentation velocity and the downward velocity imposed by the atmospheric mixing, following Lavvas et al. (2010). As the upper boundary conditions, we set zero fluxes for all the particle sizes.

3.3.2 Calculation method

We divide the atmosphere into layers with the same thickness Δz and discretize Eq. (3.20) as

$$
\begin{aligned}
\frac{\partial n_j\left(v_i\right)}{\partial t} = \quad & \frac{1}{2} \sum_{k=1}^{i-1} K_j\left(v_k, v_i - v_k\right) n_j\left(v_k\right) n_j\left(v_i - v_k\right) \\
& -n_j\left(v_i\right) \sum_{k=1}^{\mathcal{N}} K_j\left(v_i, v_k\right) n_j\left(v_k\right) \\
& -\frac{\Phi_{j+1/2}\left(v_i\right) - \Phi_{j-1/2}\left(v_i\right)}{\Delta z} + p_j\left(v_i\right),
\end{aligned} \tag{3.43}
$$

where the subscript j represents the physical quantities in the jth layer. We set the pressure at the mid-point altitude of the lowest layer as the lower boundary pressure. For Eq. (3.21), we use the upwind difference scheme instead of the central difference scheme for the calculation of sedimentation flux, because of numerical stability, and approximate $\Phi_{j+1/2}\left(v_i\right)$ as

$$
\begin{aligned}
\Phi_{j+1/2}\left(v_i\right) = \quad & -V_{s,i,j+1} n_{j+1}\left(v_i\right) \\
& -K_{zz} N_{j+1/2} \frac{n_{j+1}\left(v_i\right)/N_{j+1} - n_j\left(v_i\right)/N_j}{\Delta z}.
\end{aligned} \tag{3.44}
$$

To obtain a steady-state solution, we solve the continuity Eq. (3.43) implicitly with the same solver DLSODES (Hindmarsh, 1982) that we use in the photochemical calculations (§ 3.2). We adopt the values of relative (RTOL) and absolute (ATOL) tolerances as 10^{-4} and 10^{-20}, respectively. The initial number densities of all the sizes are set to zero. We adopt the criteria of convergence such that the volume-averaged sizes of particles in all the layers, which we calculate as

$$
s_{\mathrm{vol}} = \frac{\sum_{i=1}^{\mathcal{N}} n\left(s_i\right) s_i^4}{\sum_{i=1}^{\mathcal{N}} n\left(s_i\right) s_i^3}, \tag{3.45}
$$

are different by less than 1%.

3.4 Opacity

3.4.1 Haze particles

We calculate the extinction cross sections of haze particles based on the Mie theory (Mie, 1908). In the limit where the particle radius, s, is large compared to the radiation wavelength, λ, the Mie theory agrees with geometric optics. On the other hand, the Mie theory reduces to the Rayleigh theory in the limit of $s \ll \lambda$.

From the Mie theory, the extinction cross section of a homogeneous spherical particle of radius s, σ_{ext}, can be written as (Bohren & Huffman, 2004)

$$\sigma_{\text{ext}} = \pi s^2 \frac{2}{x^2} \sum_{n=1}^{\infty} \left(2n+1\right) \operatorname{Re}\left(a_n + b_n\right), \qquad (3.46)$$

where Re denotes the real part. Here, x is the size parameter defined as

$$x \equiv \frac{2\pi s}{\lambda}. \qquad (3.47)$$

Coefficients a_n and b_n are calculated as

$$a_n = \frac{m\phi_n\left(mx\right)\phi_n'\left(x\right) - \phi_n\left(x\right)\phi_n'\left(mx\right)}{m\phi_n\left(mx\right)\zeta_n'\left(x\right) - \zeta_n\left(x\right)\phi_n'\left(mx\right)}, \qquad (3.48)$$

and

$$b_n = \frac{\phi_n\left(mx\right)\phi_n'\left(x\right) - m\phi_n\left(x\right)\phi_n'\left(mx\right)}{\phi_n\left(mx\right)\zeta_n'\left(x\right) - m\zeta_n\left(x\right)\phi_n'\left(mx\right)}, \qquad (3.49)$$

where m is the ratio of the complex refractive indices of the particle to the surrounding atmosphere. ϕ and ζ are the so-called Ricatti-Bessel functions and the prime indicates differentiation with respect to the argument in parentheses.

We use the bhmie code (Bohren & Huffman, 2004) to calculate Eqs. (3.46)-(3.49). Complex refractive indices of haze are taken from Khare et al. (1984), which reports laboratory experiment results for production of tholin hazes in a simulated Titan's atmosphere (0.9 N_2/0.1 CH_4 gas mixture at 0.2 mb).

In Figure 3.1, we show the extinction cross sections of the haze particles of five different particle sizes, namely, 0.001 μm, 0.01 μm, 0.1 μm, 1 μm, and 10 μm. When the particle size is sufficiently small relative to the wavelength, the scattering is approximated by the Rayleigh scattering. More specifically, the cross sections for $s = 0.001$ μm, 0.01 μm, and 0.1 μm show the behavior due to the Rayleigh scattering in the visible wavelength region; namely, $\sigma_{\text{ext}} \propto \lambda^{-4}$. Also, the dependence on the particle

radius is such that $\sigma_{\text{ext}} \propto s^3$ (e.g., Petty, 2006). In contrast, for larger particles of 1 μm and 10 μm, no such feature is found, and the cross sections are relatively independent of wavelength. Note that the bumps found around 3.0 μm and 4.6 μm come from the vibrational transitions of the C-H bond and C≡N bond of the tholin haze particles, respectively (Khare et al., 1984).
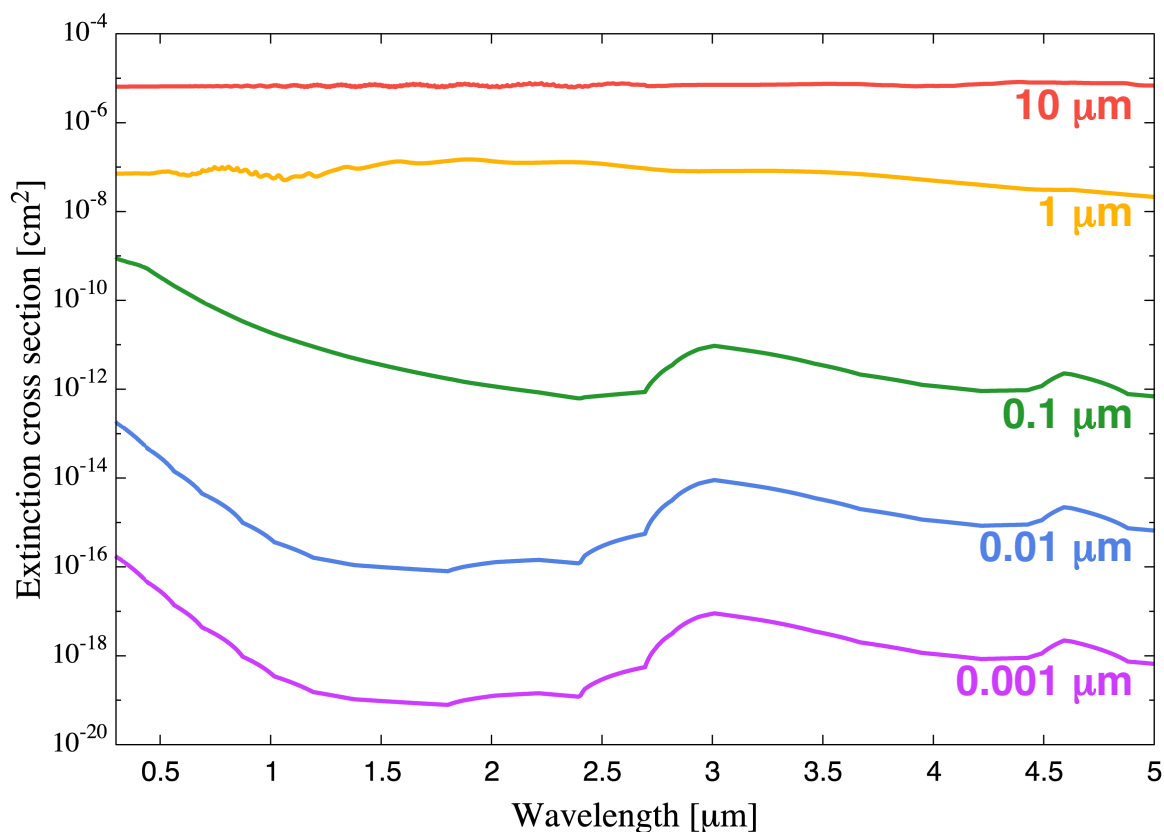
Figure 3.1: Extinction cross sections of the tholin-like haze particles of five different particle sizes of 0.001 μm, 0.01 μm, 0.1 μm, 1 μm, and 10 μm.

3.4.2 Gaseous species

For another source of radiative extinction in the atmosphere, we consider line absorption by H_2O, CO_2, CO, CH_4, O_2, NH_3, OH, N_2, HCN, C_2H_2, and H_2. We ignore the extinction by Na and K because they condense as Na_2S and KCl clouds, respectively, and settle downward in a temperature range of interest ($\lesssim$ 1000 K) (Morley et al., 2013).

The extinction cross section of species i, at wavenumber ν, $\sigma_i(\nu)$, is written as

$$\sigma_i(\nu) = \sum_{\eta,\eta'} \sigma_{i,\eta\eta'}(\nu) \tag{3.50}$$

where $\sigma_{i,\eta\eta'}$ is the line absorption cross section for the transition from lower state η to upper state η'.

For brevity, we omit the subscript i hereafter. The line absorption cross section, $\sigma_{\eta\eta'}$, is given as

$$\sigma_{\eta\eta'}(\nu) = S_{\eta\eta'}(T) f(\nu - \nu_{\eta\eta'}), \tag{3.51}$$

where $\nu_{\eta\eta'}$ is the spectral line transition wavenumber, $S_{\eta\eta'}$ is the spectral line intensity, and f is the line profile function. We calculate $\sigma_{\eta\eta'}$, using the line data from HITRAN2012 (Rothman et al., 2013). When summing the absorption cross section for each transition, we do not consider the cross sections whose spectral line intensities are less than 10^{-40} cm^{-2} because of the computational cost.

According to Sharp & Burrows (2007) and Rothman et al. (1998), the spectral line intensity at temperature T, $S_{\eta\eta'}(T)$, is written as

$$
\begin{aligned}
S_{\eta\eta'}(T) &= \frac{\pi e^2 g_\eta f_{\eta\eta'}}{m_e c} \frac{\exp\left(-hcE_\eta/k_B T\right)}{Q(T)} \\
&\quad [1 - \exp\left(-hc\left(E_{\eta'} - E_\eta\right)/k_B T\right)] \\
&= S_{\eta\eta'}(T_{\rm ref}) \frac{Q(T_{\rm ref})}{Q(T)} \frac{\exp\left(-hcE_\eta/k_B T\right)}{\exp\left(-hcE_\eta/k_B T_{\rm ref}\right)} \\
&\quad \frac{[1 - \exp\left(-hc\left(E_{\eta'} - E_\eta\right)/k_B T\right)]}{[1 - \exp\left(-hc\left(E_{\eta'} - E_\eta\right)/k_B T_{\rm ref}\right)]},
\end{aligned}
\tag{3.52} \tag{3.53}
$$

where g_η is the statistical weight of the lower state η, $f_{\eta\eta'}$ is the oscillator strength for the transition between the lower and upper states, E_η and $E_{\eta'}$ are the lower-state and upper-state energy, respectively, and $Q(T)$ is the total internal partition function at temperature T. e is the elementary charge, m_e is the electron mass, and h, c, and k_B are the Planck constant, the speed of light, and the Boltzmann constant, respectively. $S_{\eta\eta'}(T_{\rm ref})$ is the spectral line intensity at the reference temperature $T_{\rm ref}$ and written as

$$
\begin{aligned}
S_{\eta\eta'}(T_{\rm ref}) &= \frac{\pi e^2 g_\eta f_{\eta\eta'}}{m_e c} \frac{\exp\left(-hcE_\eta/k_B T_{\rm ref}\right)}{Q(T_{\rm ref})} \\
&\quad [1 - \exp\left(-hc\left(E_{\eta'} - E_\eta\right)/k_B T_{\rm ref}\right)].
\end{aligned}
\tag{3.54}
$$

The HITRAN2012 database provides the values of E_η, $E_{\eta'}$, $S_{\eta\eta'}(T_{\text{ref}})$, and $Q(T_{\text{ref}})$, where $T_{\text{ref}} = 296$ K. We calculate $Q(T)$ with the total internal partition sums (TIPS) code (Fischer et al., 2003) in the HITRAN database. This code calculates $Q(T)$ for given temperature (the temperature range is 70-3000 K) and molecular species in the HITRAN database.

We consider the air-broadened pressure-shift in the following way. The shifted spectral line transition wavenumber $\nu^*_{\eta\eta'}$ can be written as

$$\nu^*_{\eta\eta'} = \nu_{\eta\eta'} + \delta(P_{\text{ref}}) P, \tag{3.55}$$

where $\delta(P_{\text{ref}})$ is the air-broadened pressure shift, provided that the shift, $\delta(P_{\text{ref}})$, is small relative to $\nu_{\eta\eta'}$. Here, P_{ref} is the reference pressure. The HITRAN2012 database provides the values of $\delta(P_{\text{ref}})$, which we use in calculating the line absorption cross sections.

As for line broadening, we consider pressure broadening and Doppler broadening. The line profile for pressure broadening is given by the Lorentz profile (Petty, 2006),

$$f_{\text{L}}(\nu - \nu_{\eta\eta'}) = \frac{\Gamma_{\text{P}}}{\pi\left[(\nu - \nu_{\eta\eta'})^2 + {\Gamma_{\text{P}}}^2\right]}, \tag{3.56}$$

where Γ_{P} is the line half width of the pressure broadening. On the other hand, the line profile for Doppler broadening is given by the Gaussian profile (Petty, 2006),

$$f_{\text{D}}(\nu - \nu_{\eta\eta'}) = \frac{1}{\Delta\nu_{\text{D}}\pi^{1/2}} \exp\left[-\frac{(\nu - \nu_{\eta\eta'})^2}{{\Delta\nu_{\text{D}}}^2}\right], \tag{3.57}$$

where ν_{D} is the line half width of the Doppler broadening.

To consider both line profiles, the convolution of the Lorentz and Gaussian profiles, which is called the Voigt profile, is used:

$$
\begin{aligned}
f_{\text{V}}(\nu - \nu_{\eta\eta'}) &= \int_{-\infty}^{\infty} f_{\text{L}}(\nu' - \nu_{\eta\eta'}) f_{\text{D}}(\nu - \nu') d\nu' && (3.58) \\
&= \int_{-\infty}^{\infty} \frac{\Gamma_{\text{L}}}{\pi\left[(\nu' - \nu_{\eta\eta'})^2 + {\Gamma_{\text{L}}}^2\right]} \frac{1}{\Delta\nu_{\text{D}}\pi^{1/2}} \\
&\quad \exp\left[-\frac{(\nu - \nu')^2}{{\Delta\nu_{\text{D}}}^2}\right] d\nu' && (3.59) \\
&= \frac{1}{\Delta\nu_{\text{D}}\pi^{1/2}} \mathcal{H}\left(\frac{\Gamma_{\text{L}}}{\Delta\nu_{\text{D}}}, \frac{\nu - \nu'}{\Delta\nu_{\text{D}}}\right), && (3.60)
\end{aligned}
$$

where $\mathcal{H}(a, y)$ is called the Voigt function and defined as

$$\mathcal{H}(a, y) \equiv \frac{a}{\pi} \int_{-\infty}^{\infty} \frac{e^{-x^2}}{(y - x)^2 + a^2} dx. \tag{3.61}$$

For the calculation of the Voigt function, we use the polynomial expansion of this function (Kuntz, 1997; Ruyten, 2004). We adopt any cut-off in the line wings.

In the HITRAN2012 database, the line half width of the pressure broadening is calculated as

$$\begin{aligned}
\Gamma_{\mathrm{P}}(P, T) &= \left(\frac{T_{\mathrm{ref}}}{T}\right)^n \\
&\quad \left[\Gamma_{\mathrm{air}}(P_{\mathrm{ref}}, T_{\mathrm{ref}})(P - P_s) + \Gamma_{\mathrm{self}}(P_{\mathrm{ref}}, T_{\mathrm{ref}}) P_{\mathrm{s}}\right],
\end{aligned} \tag{3.62}$$

where Γ_{air} and Γ_{self} are, respectively, the air-broadened halfwidth and the self-broadened halfwidth at half maximum (HWHM) at $T_{\mathrm{ref}} = 296$ K and $P_{\mathrm{ref}} = 1$ atm and P_s is the partial pressure. The line half width of the Doppler broadening is given by

$$\Delta\nu_{\mathrm{D}} = \nu \left(\frac{2kT}{mc^2}\right)^{1/2}, \tag{3.63}$$

where m is the mass of the molecule (Petty, 2006).

We also consider the Rayleigh scattering by those molecules except OH and the collision-induced absorption by H_2-H_2 and H_2-He. We have confirmed that the Rayleigh scattering by OH is negligible for the total extinction by all the molecules because of its low abundance in the atmosphere. The Rayleigh scattering cross section is given by (Liou, 2002)

$$\sigma_{\mathrm{Rayleigh}} = \frac{128\pi^5}{3\lambda^4} \alpha^2, \tag{3.64}$$

where α is the polarizability. We use the value of the polarizability for each molecule from CRC Handbook of CHEMISTRY and PHYSICS (Haynes, 2012). The collision-induced absorption cross sections are taken from HITRAN2012 (Rothman et al., 2013).

3.5 Transmission spectrum model

We model transmission spectra following Brown (2001). The transit depth at wavelength λ, $D(\lambda)$, can be defined as

$$D(\lambda) = \frac{L_s(\lambda) - L_{obs}(\lambda)}{L_s(\lambda)}. \tag{3.65}$$

Here, L_s is the disk-integrated luminosity from the host star given by

$$L_s(\lambda) = \int_0^{R_s} F_s(\lambda)\, 2\pi r dr, \tag{3.66}$$

where R_s and F_s are the stellar radius and flux, respectively, and r is the impact parameter measured from the disk center. L_{obs} is the disk-integrated luminosity of the host star during transit. Here, we assume that the incident stellar light rays are parallel and thus F_s is constant through the stellar disk, because the orbital distances of planets of interest are much larger (by a factor of 10-100) than the host star's radius. With this assumption, L_{obs} is expressed as

$$L_{obs}(\lambda) = \int_0^{R_s} F_s(\lambda)\, e^{-\tau(r,\lambda)}\, 2\pi r dr, \tag{3.67}$$

where $\tau(r, \lambda)$ is the so-called chord optical depth defined by

$$\tau(r, \lambda) = 2 \int_0^\infty \sum_{i=1}^{\mathcal{N}} \sigma_i(r, s, \lambda)\, N_i(r, s)\, ds. \tag{3.68}$$

Here, σ_i and N_i are the extinction cross section and number density of species i, $\mathcal{N}$ is the number of species whose extinction is considered, and ds is the line element along the line of sight.

In this study, we assume that all the parts inside the sphere of radius R_0 are optically thick enough to block the incident stellar light completely. The radius R_0 may be defined as that of a solid surface or an optically thick cloud deck in the atmosphere, if present. However, some exoplanets may have no such well-defined boundary. Even if there is such a boundary, its radius is unknown in advance. According to our numerical results, τ is sufficiently larger than unity below the pressure level of 10 bar in the atmosphere considered in this study. Thus, we define R_0 as the radial distance from the planetary center at which the pressure is 10 bar.

With the above assumption and from Eqs. (3.65) to (3.67), the transit depth $D(\lambda)$ can be written as

$$D(\lambda) = \frac{R_0{}^2 + \int_{R_0{}^2}^{R_*{}^2} \left[1 - \mathrm{e}^{-\tau(r,\lambda)}\right] dr^2}{R_*{}^2}. \tag{3.69}$$

The so-called transit radius, $R_{\mathrm{tr}}(\lambda)$, is defined as

$$R_{\mathrm{tr}}(\lambda) \equiv R_* \sqrt{D(\lambda)}. \tag{3.70}$$

3.6 Calculation procedure and model parameters

Finally, we summarize the calculation procedure and the model parameters and their values that we use in our simulations.

First, we derive the vertical profiles of volume mixing ratios of the gaseous species, f_i, from the photochemical calculations (§ 3.2). Then, from the sum of f_{HCN} and $f_{\mathrm{C_2H_2}}$, which corresponds to the distribution of the haze precursors, we simulate the particle growth and calculate the number density distribution of each haze volume $n(v_i, z)$ (§ 3.3). After that, with the obtained size and number density distributions of haze particles and the vertical distribution of the gaseous species, we model transmission spectrum of the atmosphere (§ 3.5) with calculations of opacities of gaseous species and haze particles (§ 3.4). The opacity and transit depth is calculated every wavenumber grid with width of 0.1 cm^{-1}.

In this part I, we model the transmission spectra assuming the properties of the super-Earth GJ 1214b. Among super-Earths found so far, the atmosphere of GJ 1214b has been probed most by transit observations at multiple wavelengths. The model parameters and their values we use are listed in Table 3.1.

We adopt the value of the radius at the 1000-bar pressure level (simply called the 1000-bar radius, hereafter) as 2.07 $R_{\oplus}$, which is 74% of the planet radius reported by Anglada-Escudé et al. (2013); we have found that this value of the 1000-bar radius can roughly match the observed transit radii of GJ 1214b when we assume a clear solar composition atmosphere. Note that when we infer the molecular abundance from observational transmission spectrum, we suffer from degeneracy among the reference radius, 1000-bar radius, and inferred molecular abundance (see Heng & Kitzmann, 2017).

For the temperature-pressure profile, we use the analytical formula of Guillot (2010), because its smooth and simple function suits computationally-heavy photochemical calculations. With Eq. (29) of Guillot (2010), we calculate the temperature-pressure profile averaging over the whole planetary surface (i.e., $f = 1/4$ in the equation). We choose the parameters, namely, the intrinsic temperature T_{int}, equilibrium temperature T_{irr}, averaged opacity in the optical k_{v}, and averaged opacity in the infrared k_{th}, so as to match the temperature-pressure profile of GJ 1214b that Miller-Ricci & Fortney (2010) derived for a solar composition atmosphere under the assumption of efficient heat redistribution from the day and night sides. This yields $T_{\mathrm{int}} = 120$ K, $T_{\mathrm{irr}} = 790$ K, $k_{\mathrm{v}} = 10^{-4.0}$ g cm^{-2}, and $k_{\mathrm{th}} = 10^{-2.6}$ g cm^{-2}. We have confirmed that our profile agrees with that of Miller-Ricci & Fortney (2010) within 86 K for the grids we adopt.

The temperature-pressure profile we use is shown in Figure 3.2. We adopt the value of eddy diffusion coefficient K_{zz} as 1×10^7 cm^2 s^{-1}. As for the elemental abundance ratios, we assume that of the solar system abundance, which we take from Table 2 of Lodders (2003), corresponding to C/O, O/H, and N/H of 5.010×10^{-1}, 5.812×10^{-4}, and 8.021×10^{-5}, respectively.
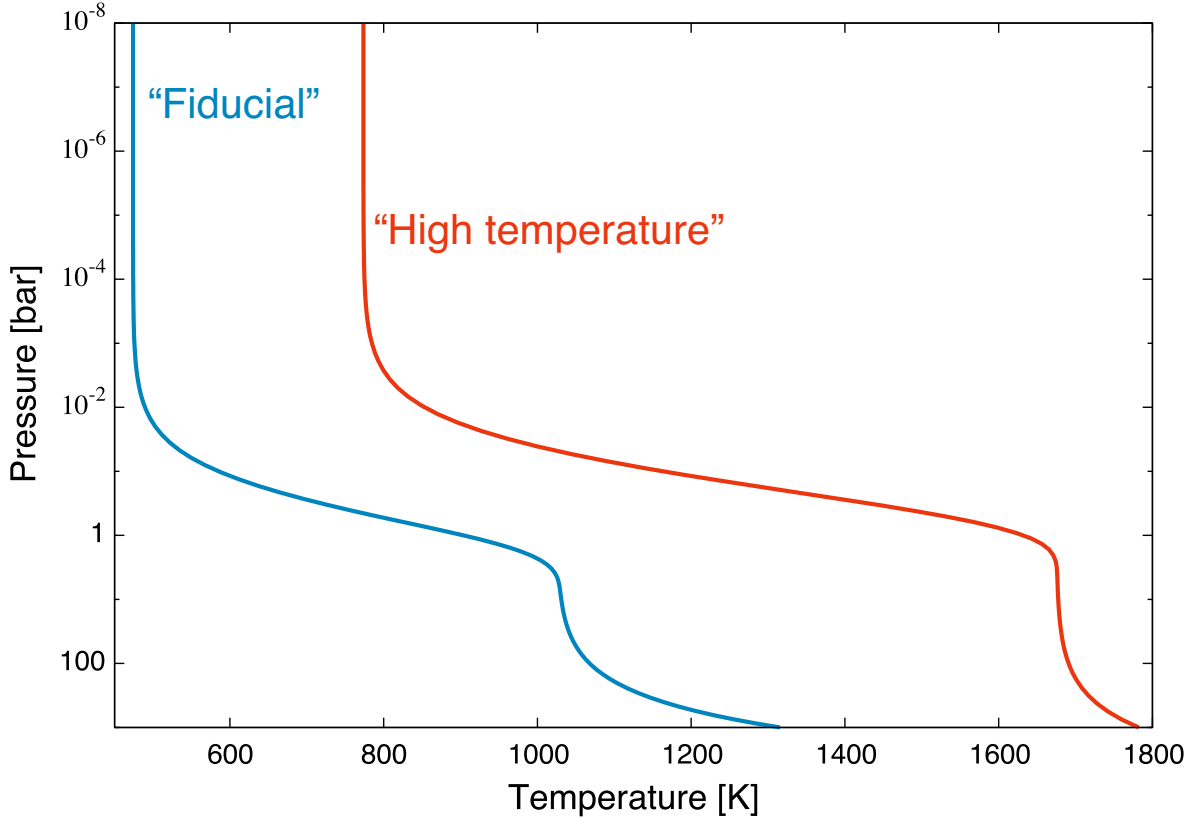
Figure 3.2: Temperature-pressure profile of the atmospheres we use as the fiducial case (blue line), which are calculated with the use of the analytical formula of Guillot (2010). Also shown is that in the case where the equilibrium temperature $T_{\rm irr}$ is higher by 500 K than in the fiducial case where $T_{\rm irr}$ is 790 K, which we use to explore the dependence of the vertical distribution of haze particles and the gaseous species on temperature-pressure profile in the atmosphere in § 4.8 (red line).

As for the stellar spectrum used in the photochemical model, we use that of GJ 1214 constructed by the MUSCLES Treasury Survey (France et al., 2016; Youngblood et al., 2016; Loyd et al., 2016), the wavelength coverage of which is from 0.55 nm to 5500 nm. The spectrum for X-rays is constructed from Chandra/XMM-Newton and APEC models (Smith et al., 2001), that for EUV from empirical scaling relation based on Lyα flux (Linsky et al., 2014), that for Lyα from model fit to line wings (Youngblood et al.,

2016), and that for visible–IR from synthetic photospheric spectra from PHOENIX atmosphere models (Husser et al., 2013). We use the version 1.1 of the panchromatic SED binned to a constant 1 Å resolution and downsampled in low signal-to-noise regions to avoid negative flux, the data of which is taken from the MUSCLES team's website[3]. We adopt 1 Å as the spectral resolution we use. The Lyα flux of GJ 1214, which is located at 14.6 pc far away from the Sun, was observed as $1.3^{+1.4}_{-0.5} \times 10^{-14}$ erg cm^{-2} s^{-1} at the Earth (Youngblood et al., 2016). From this value, we calculate the Lyα flux at the planet's orbit as 3.30×10^{13} photons cm^{-2} s^{-1} using the value of GJ 1214b's semi-major axis, 0.0148 AU (Anglada-Escudé et al., 2013), and the Lyα wavelength of 121.6 nm.

As for the monomer radius s_1, we adopt 1×10^{-3} μm. We prepare 40 volume bins, setting the volume ratio of two adjacent bins to be 3 (Lavvas et al., 2010), and cover from 1×10^{-3} μm (monomer size) to 1600 μm. As for the value of haze particle internal density ρ_p, we adopt 1.0 g cm^{-3} , which is adopted by most of the particle growth models for hydrocarbon hazes in Titan's atmosphere (e.g. Toon et al., 1992; Lavvas et al., 2010).

In the photochemical calculations, the atmosphere is vertically divided into 165 layers with thickness of 45 km, placing the lower boundary pressure at 1000 bar. This thickness is sufficiently smaller relative even to the minimum atmospheric scale hight in the atmosphere, which is 177 km. In the case of the particle growth model, we consider the pressure range from 10 bar to 10^{-10} bar with 200 same thickness layers.

Table 3.1: Model parameters and their values used in the simulations

Parameter	Description	Value
R_*	Host star radius	0.201 $R_\odot$ [4]
M_p	Planet mass	6.26 $M_\oplus$ [4]
$R_{1000 \text{ bar}}$	1000-bar radius	2.07 $R_\oplus$
K_{zz}	Eddy diffusion coefficient	1.00×10^7 cm^2 s^{-1}
s_1	Monomer radius	1.00×10^{-3} μm
ρ_p	Particle internal density	1.00 g cm^{-3}
$I_{\text{Ly}\alpha}$	Lyα flux at the planet's orbit	3.30×10^{13} photons cm^{-2} s^{-1} [5]

---

[3]https://archive.stsci.edu/prepds/muscles/
[4]Anglada-Escudé et al. (2013)
[5]Youngblood et al. (2016)

Chapter 4

Results

In this chapter, we show results of our numerical simulations. First, we investigate the fiducial UV irradiation intensity case (i.e., $\beta = 1$) in § 4.1-4.3 assuming the UV-limited case (§ 3.1.1) for the monomer production rate, $\dot{M}$. Then we explore the dependence of the vertical distribution of haze particles and the gaseous species, and the transmission spectrum on the UV irradiation intensity, β, assuming the UV-limited case for $\dot{M}$ in § 4.4 and carbon-limited case (§ 3.1.2) in § 4.5. Finally, assuming the UV-limited case, we explore the dependence of the results on the other model parameters, eddy diffusion coefficient in § 4.6, C/O ratio in § 4.7, temperature structure in § 4.8, and monomer size in § 4.9.

4.1 Photochemical calculations

First we outline the photochemistry of the atmosphere. Although the results we show below are basically the same as those from the previous studies, we show them because they are helpful in interpreting our later results. We note that our photochemical models of GJ 1214b's atmosphere are the first ones that use the observed GJ 1214's UV spectrum (France et al., 2016; Youngblood et al., 2016; Loyd et al., 2016).

Figure 4.1 shows the calculated vertical distributions of gaseous species in the photochemical equilibrium state (solid lines). We also present the distributions obtained by thermochemical equilibrium calculations (dashed lines) that ignore photochemical processes and eddy diffusion. In the lower atmosphere ($P \gtrsim 10^{-4}$ bar), the eddy diffusion mixing, which tends to smooth out compositional gradients, is found to yield constant abundances of H_2O, CH_4, NH_3, N_2, and CO equal to the lower boundary values. In the upper atmosphere ($P \lesssim 10^{-4}$ bar), it turns out that many species (i.e., H, O, C,

HCN, N, O_2, C_2H_2, CH_3, OH, CH_3OH, NH_2, CH_2, and $O(^1D)$)) that are quite rare in thermochemical equilibrium states are produced photochemically and H is the most abundant species. The H is known to act as a reactive radical in reducing atmospheres (Hu et al., 2012).
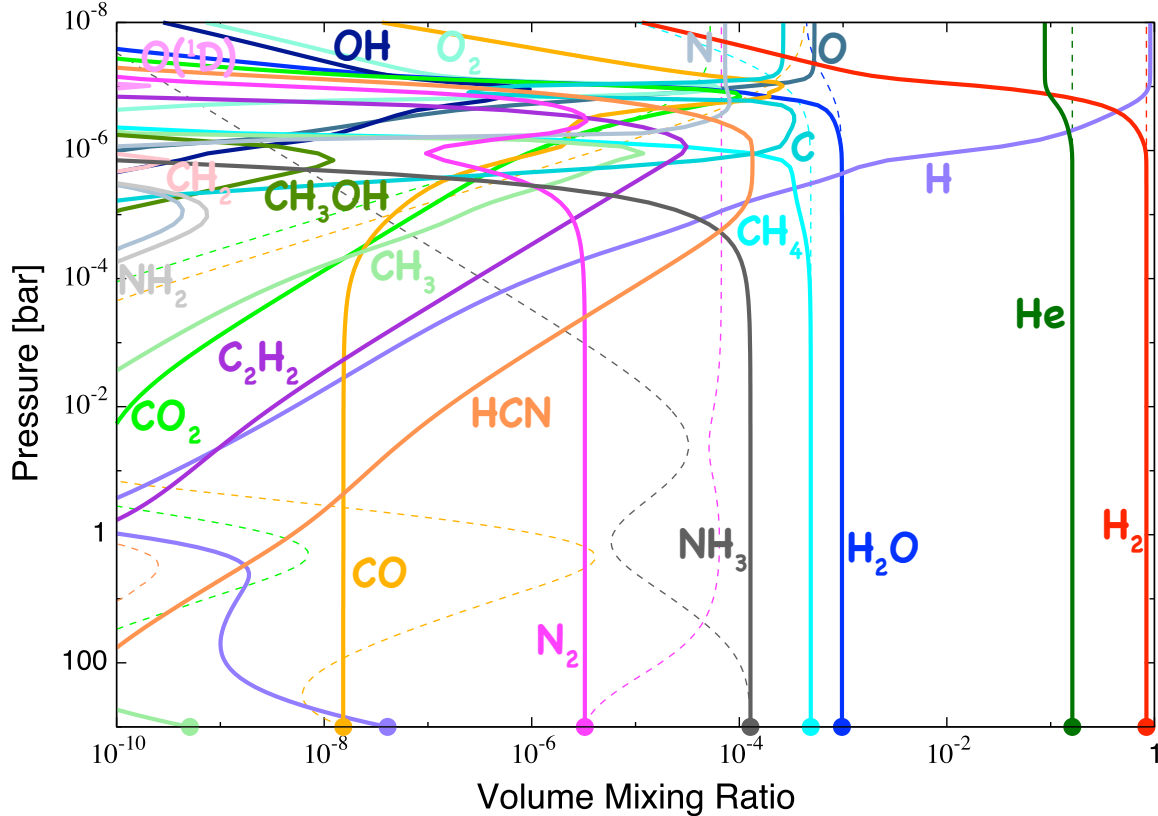
Figure 4.1: Vertical distributions of gaseous species in the photochemical equilibrium atmosphere. Filled circles represent the thermochemical equilibrium values at the lower boundary. The thermochemical equilibrium abundances are shown with dashed lines for reference. Note that the eddy diffusion transport is not included in the thermochemical equilibrium calculations.

As for the haze precursors, HCN and C_2H_2, f_{HCN} is always greater than $f_{C_2H_2}$. This means that in our simulations, the profile of the production rate of monomers is determined mainly by that of f_{HCN}. The ratio f_{HCN} is constant in the pressure range of 1×10^{-6} bar to 1×10^{-5} bar because HCN is the most stable N-bearing species in this range.

Below, we describe the production (and loss) mechanisms of HCN and C_2H_2 Moses et al. (2011) discussed for the cases of two hot Jupiters, HD 189733b ($T_{eq} = 1100$ K) and

HD 209458b ($T_{\text{eq}} = 1316$ K[1]). They showed that at low pressures, CH_4 is converted to HCN through the following reactions, making HCN the most abundant carbon-bearing species;

$$2\,(H_2O + h\nu \rightarrow H + OH)$$
$$2\,(OH + H_2 \rightarrow H_2O + H)$$
$$NH_3 + H \rightarrow NH_2 + H_2$$
$$CH_4 + H \rightarrow CH_3 + H_2$$
$$NH_2 + H \rightarrow NH + H_2$$
$$NH + H \rightarrow N + H_2$$
$$N + CH_3 \rightarrow H_2CN + H$$
$$H_2CN + H \rightarrow HCN + H_2$$
$$\overline{\text{Net} : CH_4 + NH_3 \rightarrow HCN + 3H_2.}$$
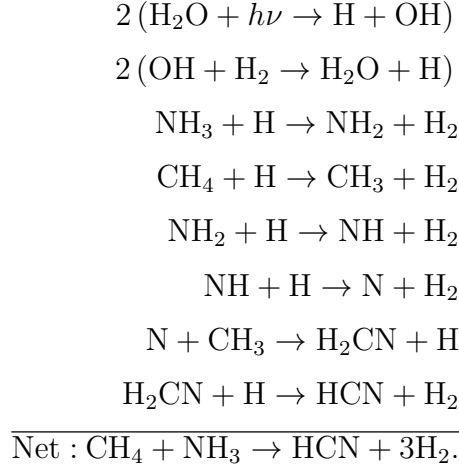
Also, they showed that in the cooler atmosphere of HD 189733b, NH_3 is converted to HCN through the following reactions;

$$CO + h\nu \rightarrow C + O$$
$$N_2 + h\nu \rightarrow 2N$$
$$C + C_2H_2 \rightarrow C_3H_2$$
$$N + C_3H_2 \rightarrow HC_3N + H$$
$$H + HC_3N \rightarrow CN + C_2H_2$$
$$CN + H_2 \rightarrow HCN + H$$
$$\overline{\text{Net} : CO + N_2 + H_2 \rightarrow HCN + N + O + H.}$$
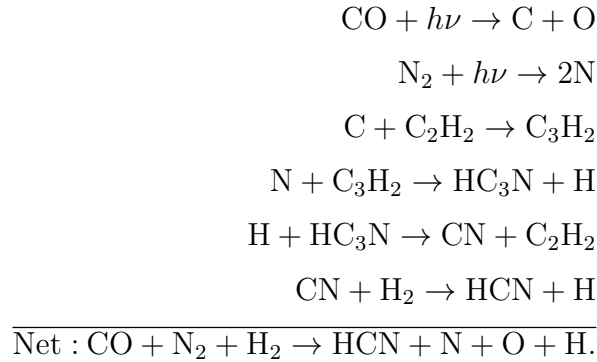
As for C_2H_2, they showed that in the region where CH_4 or CH_3 are more abundant

---

[1]http://www.openexoplanetcatalogue.com

than C, C_2H_2 are produced from the destruction of CH_4 through the following reactions;

$$2\,(H_2O + h\nu \rightarrow H + OH)$$
$$2\,(OH + H_2 \rightarrow H_2O + H)$$
$$2\,(CH_4 + H \rightarrow CH_3 + H_2)$$
$$CH_3 + H \rightarrow {}^1CH_2 + H_2$$
$${}^1CH_2 + H_2 \rightarrow {}^3CH_2 + H_2$$
$${}^3CH_2 + CH_3 \rightarrow C_2H_4 + H$$
$$C_2H_4 + H \rightarrow C_2H_3 + H_2$$
$$C_2H_3 + H \rightarrow C_2H_2 + H_2$$
$$\overline{\text{Net} : 2CH_4 \rightarrow C_2H_2 + 3H_2.}$$
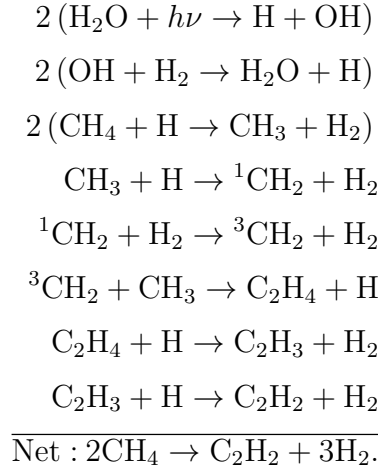
The photolysis of H_2O is important for providing H to destroy CH_4. At high pressures, C_2H_2 is hydrogenerated and converted to CH_4 through the following reactions;

$$C_2H_2 + H + M \rightarrow C_2H_3 + M$$
$$C_2H_3 + H_2 \rightarrow C_2H_4 + H$$
$$C_2H_4 + H + M \rightarrow C_2H_5 + M$$
$$C_2H_5 + H \rightarrow 2CH_3$$
$$2\,(CH_3 + H_2 \rightarrow CH_4 + H)$$
$$\overline{\text{Net} : C_2H_2 + 3H_2 \rightarrow 2CH_4.}$$
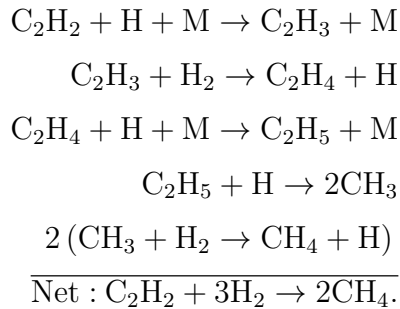
They reported that the above scheme was responsible for removing C_2H_2 while the photolysis of C_2H_2 resulted in simply recycling C_2H_2.

Although some of the species involved in the production (and loss) mechanisms of HCN and C_2H_2 are missing in our photochemical model and the atmospheric temperature considered in this study is lower than HD 189733b and HD 209458b, the similar reactions are considered to be responsible for the production (and loss) mechanisms of HCN and C_2H_2. Below, we also explore how the steady-state abundances of HCN and C_2H_2 are maintained.

In Figure 4.2, we plot the distributions of the production and loss rates of HCN due to thermochemical and photochemical reactions, and transport by eddy diffusion for the

steady-state distribution of HCN. In the pressure range of 1×10^{-7} bar to 3×10^{-6} bar, the steady-state is maintained almost by the production process via the thermochemical reaction,

$$R52 : H_2 + CN \rightarrow HCN + H,$$

and the loss process via photodissociation,

$$P13 : HCN \rightarrow H + CN.$$

On the other hand, in the pressure range of 3×10^{-6} bar to 2×10^{-3} bar, the steady-state is maintained by a balance between the production process via the thermochemical reaction,

$$R62 : N + CH_3 \rightarrow H_2 + HCN,$$
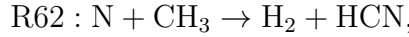
and the loss process via eddy diffusion transport to the upper atmosphere.
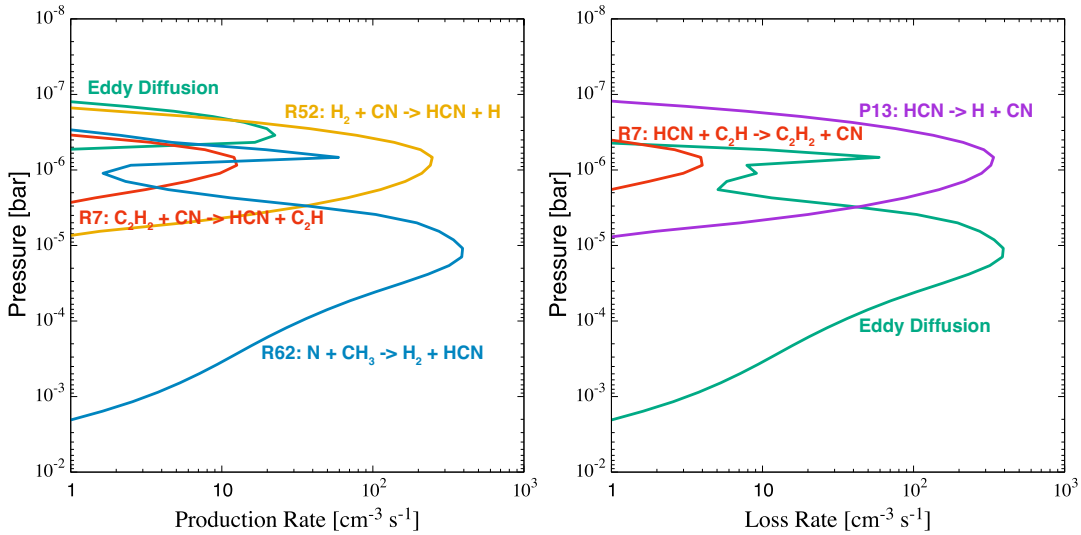
(a) Production Rate of HCN   (b) Loss Rate of HCN

Figure 4.2: Distributions of (a) the production and (b) loss rates of HCN due to thermochemical and photochemical reactions, and transport by eddy diffusion for the steady-state distribution of HCN.

Figure 4.3 is the same as Fig. 4.2 but for C_2H_2. In the pressure range of 1×10^{-7} bar to 5×10^{-6} bar, the steady-state is determined by the production process via the thermochemical reaction,

$$R30 : C_2H + H_2 \rightarrow H + C_2H_2,$$

and the loss process via photodissociation,

$$P16 : C_2H_2 \rightarrow C_2H + H.$$
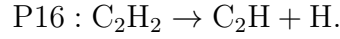
On the other hand, in the pressure range of 5×10^{-6} bar to 2×10^{-5} bar, the steady-state is determined by production process via the thermochemical reaction,

$$R71 : C_2H + NH_3 \rightarrow NH_2 + C_2H_2,$$

and the loss process, via photodissociation,

$$P16 : C_2H_2 \rightarrow C_2H + H.$$
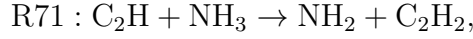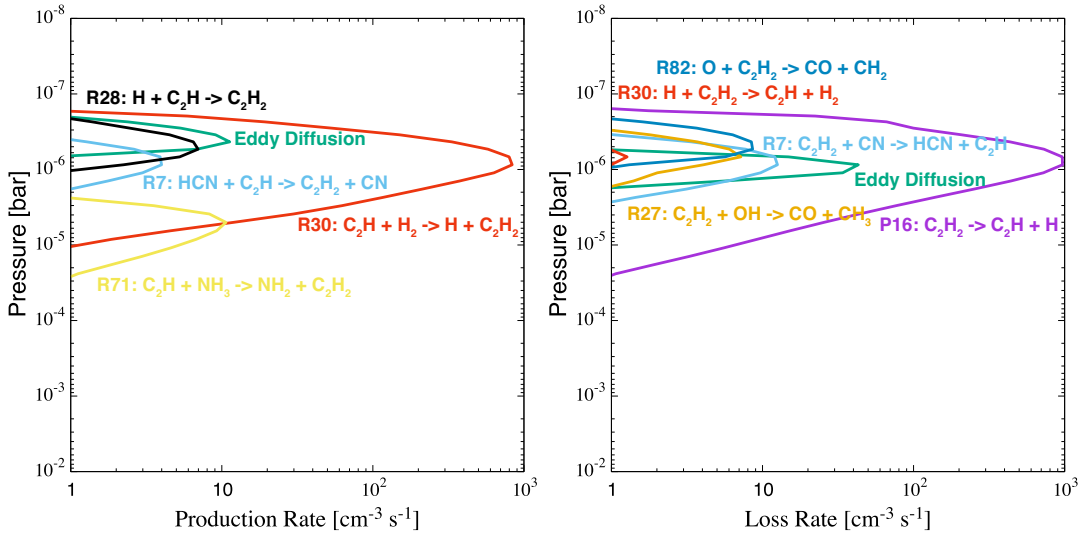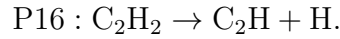
(a) Production Rate of C_2H_2 (b) Loss Rate of C_2H_2

Figure 4.3: Distributions of (a) the production and (b) loss rates of C_2H_2 due to thermochemical and photochemical reactions, and transport by eddy diffusion for the steady-state distribution of C_2H_2.

4.2 Particle growth calculations

The growth of haze particles occurs via competition among coagulation, sedimentation, and diffusion. Knowledge of the sedimentation velocity is therefore helpful in understanding the particle growth. Figure 4.4 shows the sedimentation velocity along pressure for five different particle radii, 1.0×10^{-3} μm, 3.9×10^{-2} μm, 1.5 μm, 59 μm, and 1600 μm. Change of the trend found at $P \sim 10^{-2}$ bar for the 59 μm particle and $P \sim 10^{-3}$ bar for the 1600 μm particle, respectively, results from the transition from slip flow ($K_{n,i} = \lambda_a/s_i > 1$) to Stokes flow ($K_{n,i} = \lambda_a/s_i < 1$). In the slip flow regime, the sedimentation velocity is proportional to the particle radius (see Eqs. (3.22) and (3.26)). On the other hand, in the Stokes flow regime, the sedimentation velocity is proportional to the square of the particle radius (see Eqs. (3.22) and (3.26)).
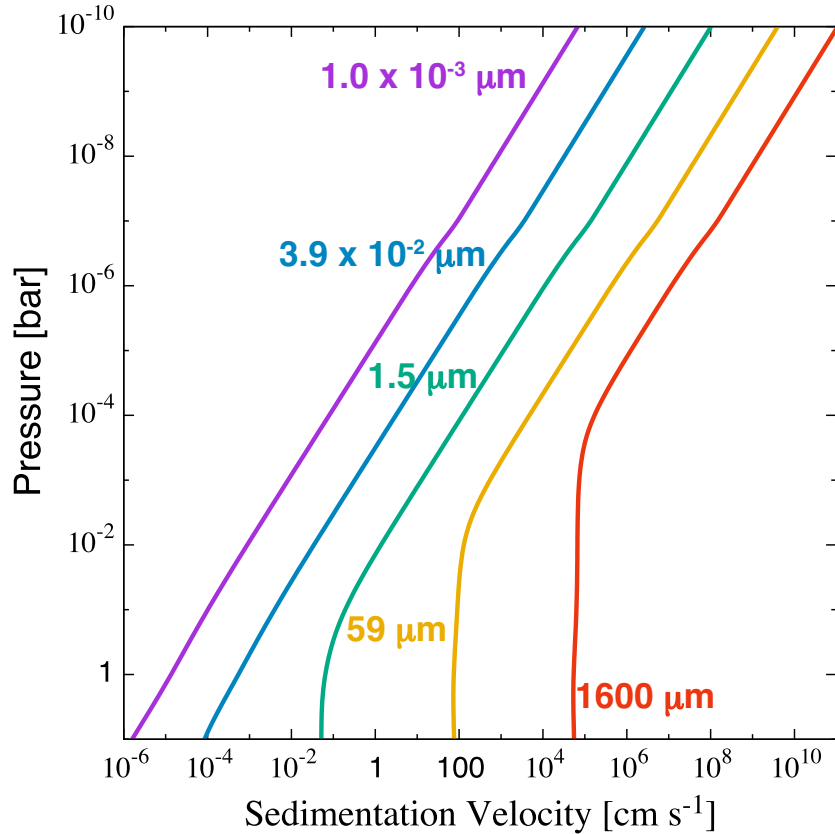
Figure 4.4: Sedimentation velocity for five different particle radii, 1.0×10^{-3} μm (purple line), 3.9×10^{-2} μm (blue line), 1.5 μm (green line), 59 μm (orange line), and 1600 μm (red line) along pressure.

Figure 4.5 shows the vertical profiles of haze properties. Here, we define the surface

average radius s_{surf} (orange solid line) as

$$s_{\text{surf}} = \frac{\sum_{i=1}^{\mathcal{N}} n\left(s_i\right) s_i^3}{\sum_{i=1}^{\mathcal{N}} n\left(s_i\right) s_i^2},\tag{4.1}$$

and the volume average radius s_{vol} (red solid line) by Eq. (3.45). If the two average sizes agree with each other at a certain altitude, the size distribution is unimodal at the altitude. The surface average number density n_{surf} (orange dashed line) and the volume average number density n_{vol} (red dashed line) are calculated as

$$n_{\text{surf}} = \frac{\sum_{i=1}^{\mathcal{N}} n\left(s_i\right) s_i^3}{s_{\text{surf}}^3}\tag{4.2}$$

and

$$n_{\text{vol}} = \frac{\sum_{i=1}^{\mathcal{N}} n\left(s_i\right) s_i^3}{s_{\text{vol}}^3},\tag{4.3}$$

respectively. Also, the mass densities for all the size bins at each pressure level are plotted with the blue color contour and the vertical profile of the monomer mass production rate is plotted with the green solid line.

From Fig. 4.5, it is demonstrated that the average radii change dramatically with altitude. In the upper atmosphere, particles grow little because they settle faster than coagulational growth proceeds. The number densities become larger as altitude decreases (or the pressure increases) and they take the peak value at $P \sim 10^{-7}$ bar. Coagulational growth occurs significantly below this pressure level. As altitude decreases, the average radii increase from 1×10^{-3} μm to 2-3 μm because of coagulational growth, and the number densities decrease by several orders of magnitude from the peak values. Again, change of the trend found at $P \sim 10^{-2}$ bar results from the transition from the slip flow to Stokes flow regimes. A significant increase in the sedimentation velocity due to the regime transition of drag force (see Fig. 4.4) inhibits the collision between particles.

The slight difference between s_{surf} and s_{vol} means that the haze contains different size particles at each altitude. The color contour indicates that particles in some narrow range of size are abundant at each altitude and the monomer size particles exist broadly below the level of 10^{-7} bar because monomer production occurs in this region.

In Figure 4.6, we plot the distributions of number density of haze particles for all the size bins at seven different pressure levels, 3.4×10^{-8} bar, 2.3×10^{-7} bar, 8.3×10^{-6} bar, 4.9×10^{-4} bar, 3.7×10^{-2} bar, 0.95 bar, and 10 bar. First it is found that the number
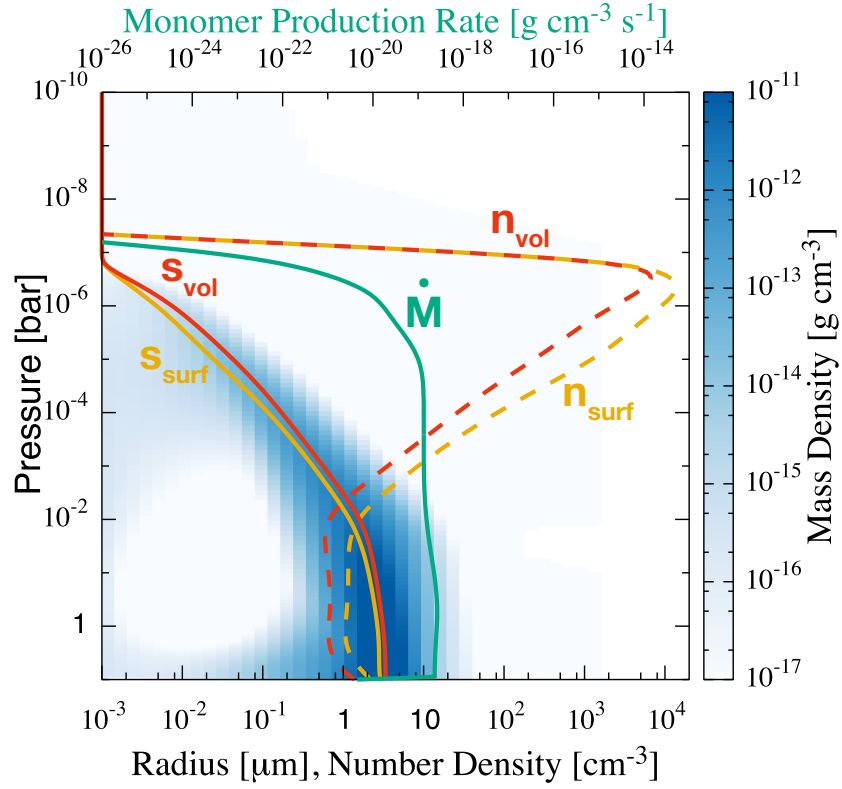
Figure 4.5: Vertical profiles of the surface average radius s_{surf} (orange solid line) and number density n_{surf} (orange dashed line), and the volume average radius s_{vol} (red solid line) and number density n_{vol} (red dashed line) along with that of the monomer mass production rate (green solid line). See the text for the definition of each quantity. Also, the mass densities for all the size bins at each pressure level are plotted with the blue color contour.

density of monomer size, 10^{-3} μm, is the largest among all the sizes at all the pressure levels because of the large monomer production rate. At low pressures of $P \lesssim 10^{-5}$ bar, the coagulation due to brownian diffusion is the dominant process, whereas that due to gravitational collection hardly occurs. On the other hand, at high pressures of $P \gtrsim 10^{-5}$ bar, both coagulation mechanisms contribute to the particle growth. The coagulation due to gravitational collection makes a second peak of number density for the pressure levels higher than 8.3×10^{-6} bar, because it occurs in a runaway fashion much more rapidly compared to that due to brownian diffusion.

The change of size distribution can be understood as follows: The particles grow through the frequent collisions with the abundant small particles. The collision timescale τ_{coll} between a large particle and monomer size particles can be written as $\tau_{\mathrm{coll}} = (n_1 \sigma \Delta v)^{-1}$, where n_1 is the number density of monomers, σ is the collision cross section
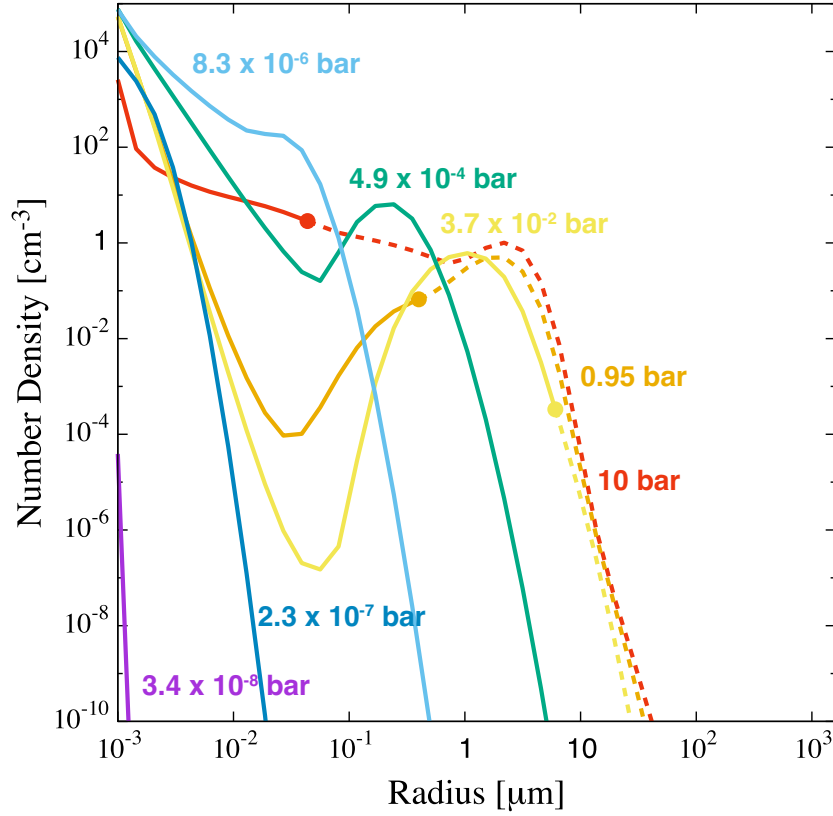
Figure 4.6: Distributions of number density of haze particles for all the size bins at seven different pressure levels, 3.4×10^{-8} bar (purple line), 2.3×10^{-7} bar (blue line), 8.3×10^{-6} bar (light blue line), 4.9×10^{-4} bar (green line), 3.7×10^{-2} bar (yellow line), 0.95 bar (orange line), and 10 bar (red line). The Stokes regime is indicated by dashed lines, while the slip flow regime is indicated by solid lines; the transition points are marked by filled circles.

of the large particle, and Δv is the relative velocity between the particles. The relative velocity due to sedimentation is proportional to particle radius s in the slip flow regime and s^2 in the Stokes flow regime (see Eqs. (3.22) and (3.26)), while the relative velocity due to brownian diffusion is proportional to $s^{-\frac{3}{2}}$ (see Eq. (3.31)). Thus, $\tau_{\text{coll}} \propto s^{-3}$ (slip flow) and $\propto s^{-4}$ (Stokes flow) for gravitational collection, while $\tau_{\text{coll}} \propto s^{-1/2}$ for brownian diffusion. This means the particle growth is always a runaway process: The larger the particle, the faster the growth proceeds. Also, the gravitational collection is much faster than the brownian diffusion especially for large size particles. Therefore, from $P \sim 10^{-5}$ bar on, the second peak grows rapidly and a valley-shaped distribution develops (see yellow and orange lines), because gravitational collection contributes predominantly to the particle growth above this pressure.

At $P = 10$ bar, however, the valley is found to disappear. This is because the drag law for the large particles shifts from the slip flow regime to the Stokes regime. In Fig 4.6, the Stokes regime is indicated by dashed lines, while the slip flow regime is indicated by solid lines; the transition points are marked by filled circles. Since the sedimentation velocity is so high in the Stokes regime (see Fig. 4.4) that the particles settle faster than they grow, the largest-size group ($\gtrsim 2$ μm) stops growing (see the orange lines). Then, small particles, which are still in the slip flow regime, grow and are catching up with the largest particles.
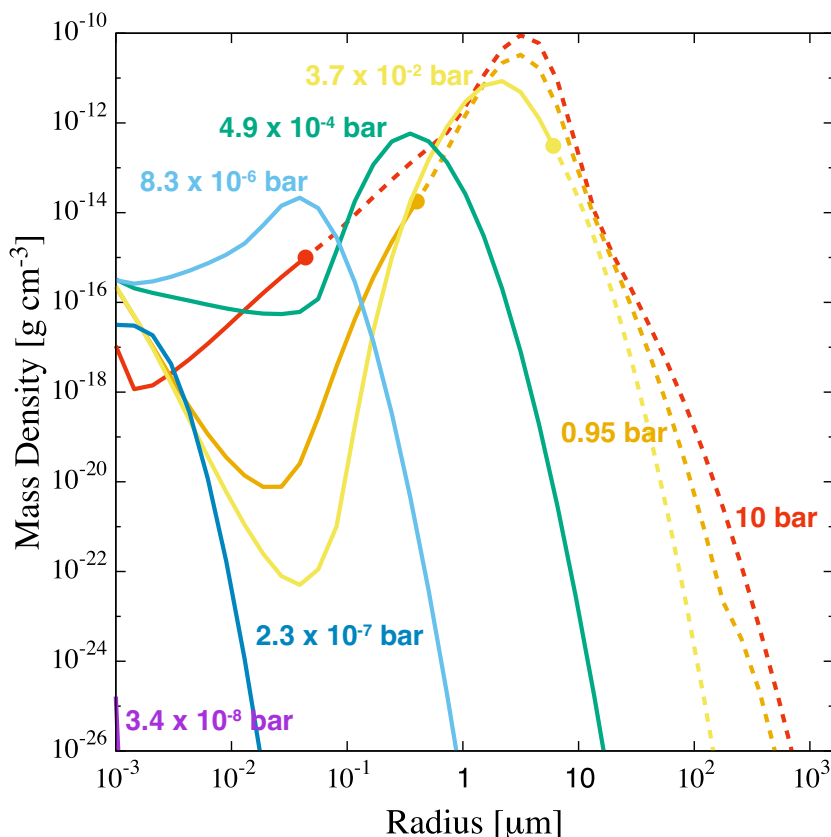
Figure 4.7: Same as Fig. 4.6 but the distribution of mass density.

In Figure 4.7, we plot the distributions of mass density for all the size bins at the same set of seven different pressure levels as shown in Fig. 4.6. It can be noticed that there are dominant sizes that account for most of the total haze mass for all the seven pressure levels. And the dominant size becomes larger, as pressure increases, because of the coagulational growth.

4.3   Transmission spectrum models

Figure 4.8 shows the transmission spectrum models for the atmosphere with haze (green line) and without haze (black line). Also, the relative cross section of the planetary disk with radius corresponding to a certain pressure level, which is defined as

$$D_P = \frac{R_P^2}{R_s^2},\tag{4.4}$$

is presented by horizontal dotted lines from $P = 1 \times 10^{-6}$ bar to 1 bar for the atmosphere without haze. In equation (4.4), R_P and R_s are the radius at the pressure level P and the stellar radius, respectively. Roughly at these pressure levels, there exist the molecules accountable for the spectral features. We have confirmed that the chord optical depth at the pressure that corresponds to the transit radius is between 0.1 and 1, depending on wavelength. Note that the transmission spectrum models are smoothed for clarity by averaging over the nearest 633 wavenumber points, namely 63.2 cm^{-1}, for each point. We use the same smoothing method for the results of spectrum models hereafter.

In the spectrum model for the atmosphere without haze (black line), several characteristic spectral features can be seen. For example, prominent features of H_2O are found around $\lambda = 0.7$ μm, 0.8 μm, 0.9 μm, 1.2 μm, 1.3-1.6 μm, 1.9 μm, and 2.5-3.0 μm, those of CH_4 around 1.7 μm, 2.2-2.4 μm, and 3.3 μm, and that of HCN around 3.0 μm. The Rayleigh scattering feature mainly due to H_2 can be seen in the optical wavelength region.

The spectrum for the atmosphere with haze (green line) is relatively featureless, compared to that for the atmosphere without haze (black line). This is because the haze particles in the upper atmosphere ($P \lesssim 10^{-4}$ bar) makes the atmosphere optically thick and prevent the molecules in the lower atmosphere ($P \gtrsim 10^{-4}$ bar) from showing their absorption features. However, the small features of CH_4 above 10^{-4} bar can be seen at 2.2-2.4 μm and 3.3 μm because of their large extinction cross sections at these wavelengths. Also, the spectral features due to the C-H and C$\equiv$N bonds of the haze particles appear at 3.0 and 4.6 μm, respectively.

In the wavelength region of 0.3-1 μm (green line), the spectral slope due to Rayleigh scattering by small ($\lesssim 0.1$ μm) haze particles in the upper atmosphere ($P \lesssim 10^{-4}$ bar) can be seen. Previous studies demonstrated that the existence of two separate cloud layers were needed to explain both the spectral slope in the optical and the lack of the absorption features in the near-infrared simultaneously; A layer composed of small size ($\lesssim 0.1$ μm) particles in the upper atmosphere responsible for the spectral slope
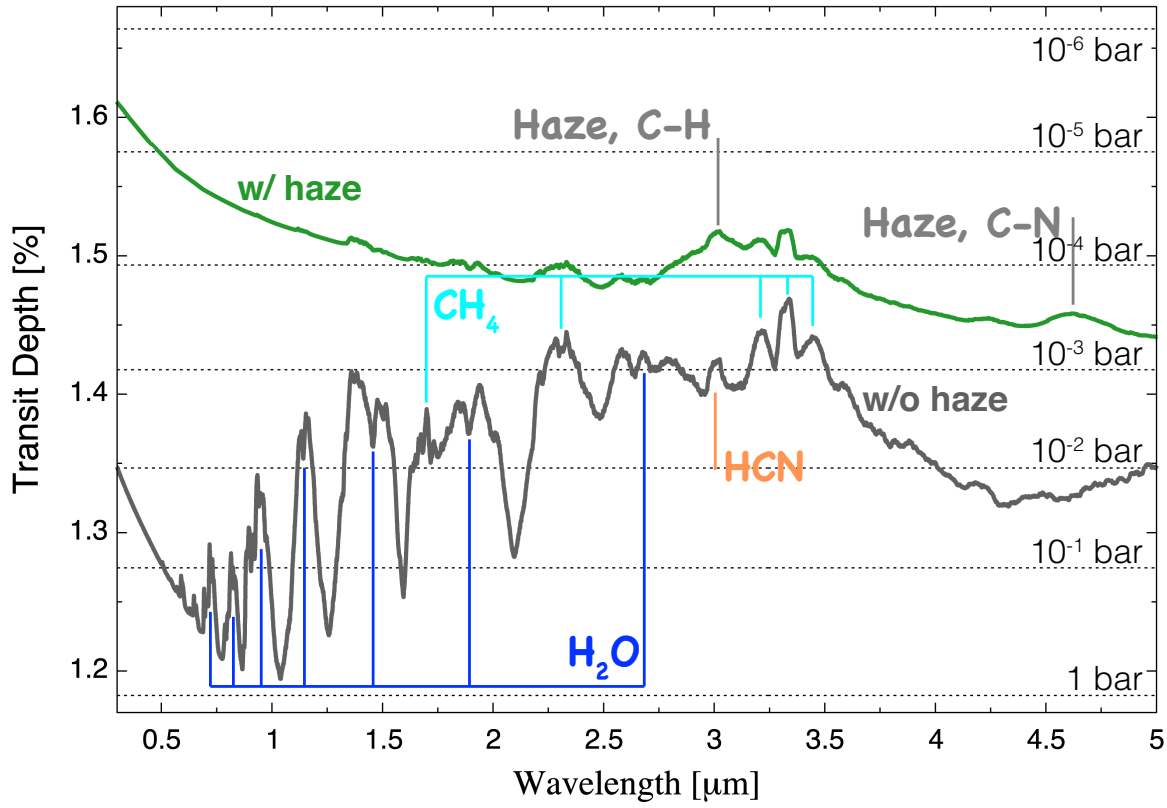
Figure 4.8: Transmission spectrum models for the atmosphere with haze (green line) and without haze (black line). Horizontal dotted lines represent the transit depths corresponding to the pressure levels from 1×10^{-6} bar to 1 bar for the atmosphere without haze. Note that the transmission spectrum models are smoothed for clarity by averaging over the nearest 633 wavenumber points, namely 63.2 cm^{-1}, for each point.

due to Rayleigh scattering and the dense cloud layer that prevents the molecules from showing their absorption features (Ehrenreich et al., 2014; Sing et al., 2015; Dragomir et al., 2015). This study is the first to produce the transmission spectrum that has the spectral slope, but no distinct molecular absorption features, without assuming such cloud layers, by calculating the distribution of the size and number density of haze particles in the atmosphere directly.

4.4   Dependence on UV irradiation intensity for UV-limited case

Here, we explore the dependence of the vertical distribution of haze particles and the gaseous species, and the transmission spectrum on β (UV irradiation intensity) by changing its value from 5 orders of magnitude smaller to 5 orders of magnitude larger than the fiducial case, assuming the UV-limited case (§ 3.1.1) for the monomer production rate, $\dot{M}$. The values of the other model parameters are set to those used in the fiducial case.

The difference in β of 10 orders of magnitude might come from the differences in UV irradiation intensity and metallicity, and uncertainty of the dependence of $\dot{M}$ on $I_{\mathrm{Ly}\alpha}$. Observation shows there is $\sim$1 order of magnitude difference in UV emission intensity of M dwarfs (Linsky et al., 2013). Considering the semi-major axes of planets from currently observable ones to those of future targets, 0.01-1 AU, there are $\sim$5 orders of magnitude difference in UV irradiation intensity among the current and future targets around M dwarfs. Although we assume linear dependence of $\dot{M}$ on $I_{\mathrm{Ly}\alpha}$, quadratic dependence is also proposed (Trainer et al., 2006). Assuming quadratic dependence results in $\sim$10 orders of magnitude difference in $\dot{M}$. Also, the difference in atmospheric metallicity has to be considered. Considering 1000 $\times$ metal-rich atmosphere than solar abundance atmosphere, the volume mixing ratio of CH_4 is 5×10^{-2} (5×10^{-4} for solar abundance atmosphere) and there can be $\sim$2 orders of magnitude difference in CH_4 abundance. Since both the UV irradiation intensity and CH_4 abundance affect the value of $\dot{M}$, we vary the value of β by 10 orders of magnitude, also considering the uncertainty of the dependence of $\dot{M}$ on $I_{\mathrm{Ly}\alpha}$ to some extent.

4.4.1 Photochemical calculations
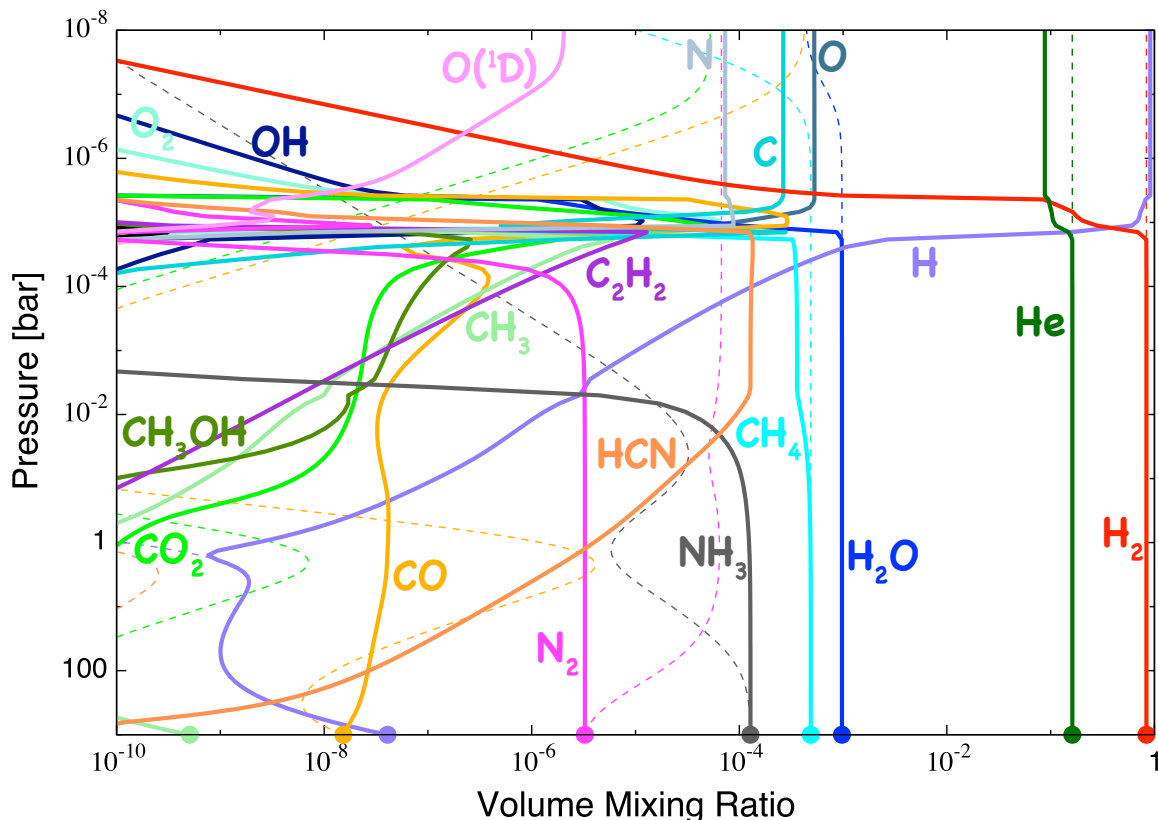
Figure 4.9: Same as Fig. 4.1 but for haze monomer production parameter $\beta = 10^5$. See Eq. (3.9) for the definition of β.

Figures 4.9, 4.10, 4.11, and 4.12 show the calculated vertical distributions of gaseous species for four different values of β, 10^5, $10^{2.5}$, $10^{-2.5}$, and 10^{-5}, respectively. We have confirmed the dependence of the molecular vertical distributions on the incident UV flux reported by previous works (e.g., Miguel & Kaltenegger, 2014; Venot et al., 2014), as shown in Fig. 4.9-4.12. In the high UV cases ($\beta = 10^5$ and $10^{2.5}$), the photodissociation of the molecules such as H_2, H_2O, CH_4, and NH_3 occurs and produces H, O, C, HCN, N, O_2, C_2H_2, CH_3, OH, $O(^1D)$, and CH_3OH at deeper levels than in the fiducial case (Fig. 4.1). On the other hand, in the low UV cases ($\beta = 10^{-2.5}$ and 10^{-5}), the photodissociation does not occur effectively and the eddy diffusion evens out the abundance of the molecules such as H_2O, CH_4, and NH_3 up to higher altitudes.

As for the haze precursors, HCN is always more abundant than C_2H_2, irrespective of UV flux. Note that assumed values of C/O, O/H, and N/H are 5.010×10^{-1}, 5.812×10^{-4}, and 8.021×10^{-5}, respectively. It can be seen that the higher (lower) the incident UV

flux is, the lower (higher) the region where the precursors are produced photochemically becomes, because of the effective photodissociation.
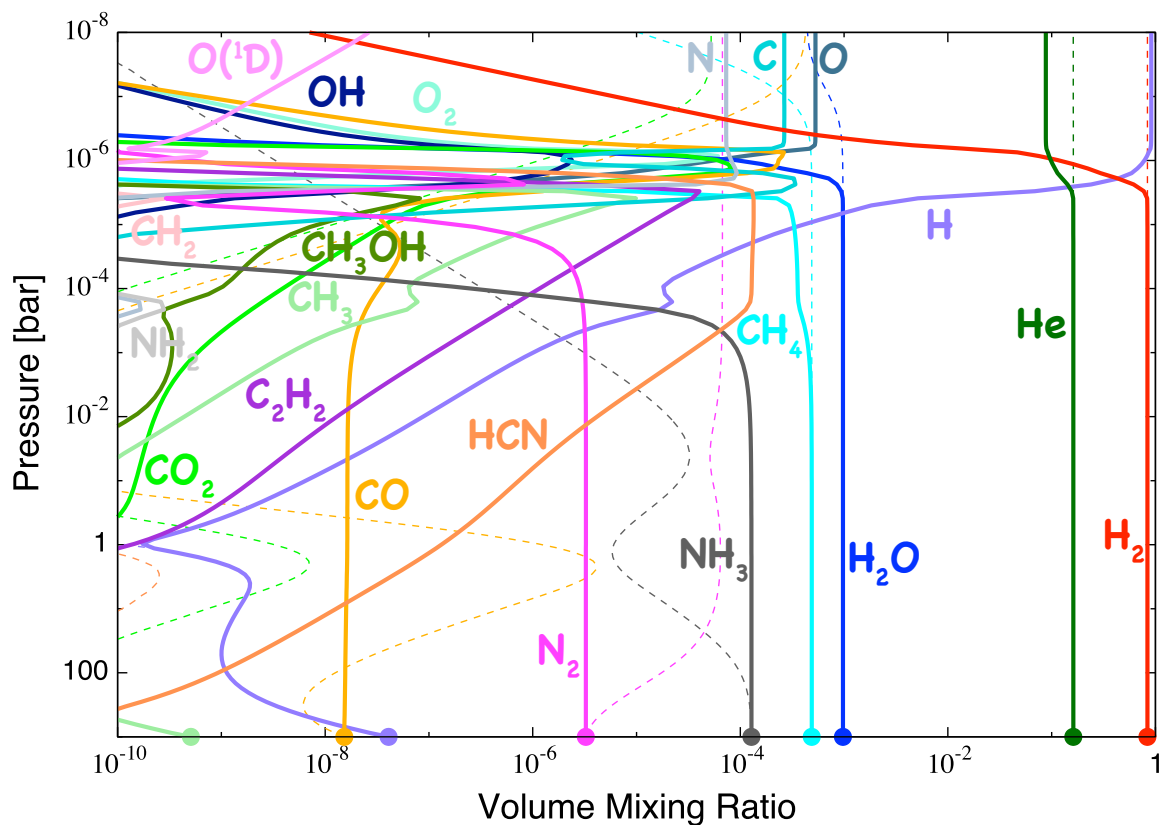
Figure 4.10: Same as Fig. 4.1 but for haze monomer production parameter $\beta = 10^{2.5}$.
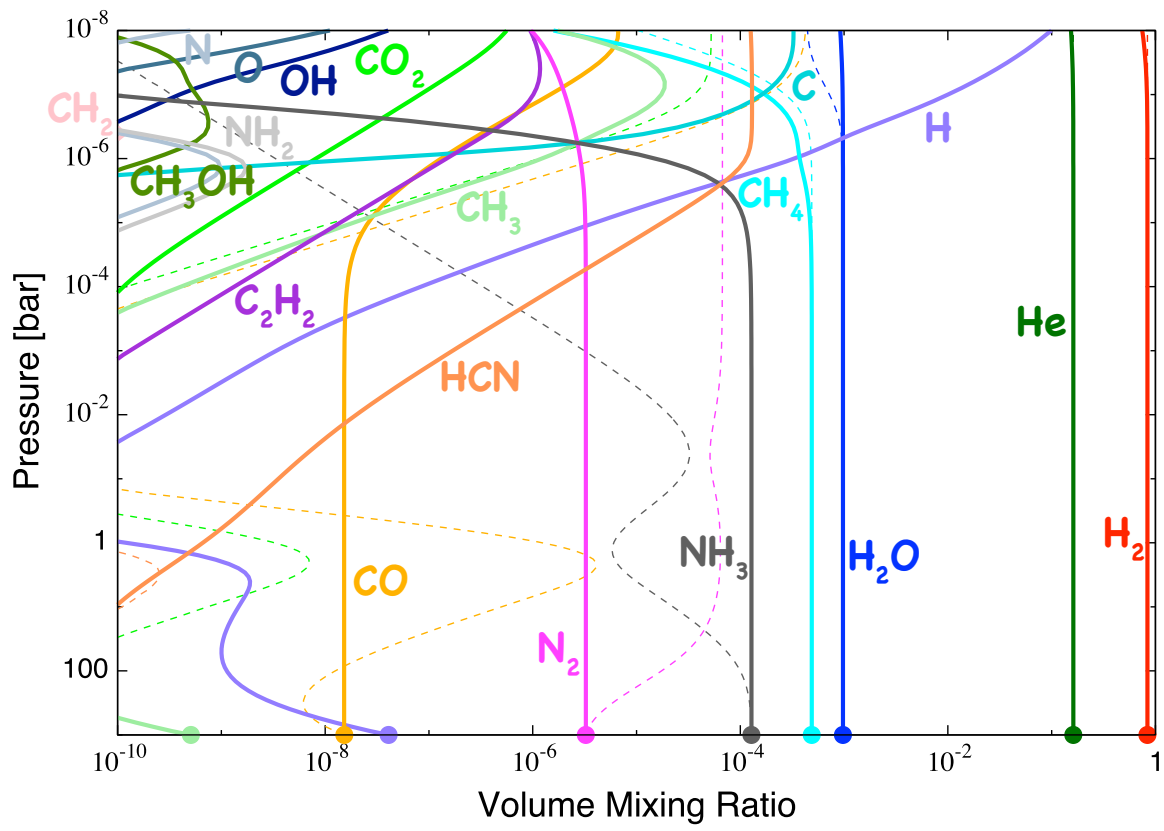
Figure 4.11: Same as Fig. 4.1 but for haze monomer production parameter $\beta = 10^{-2.5}$.
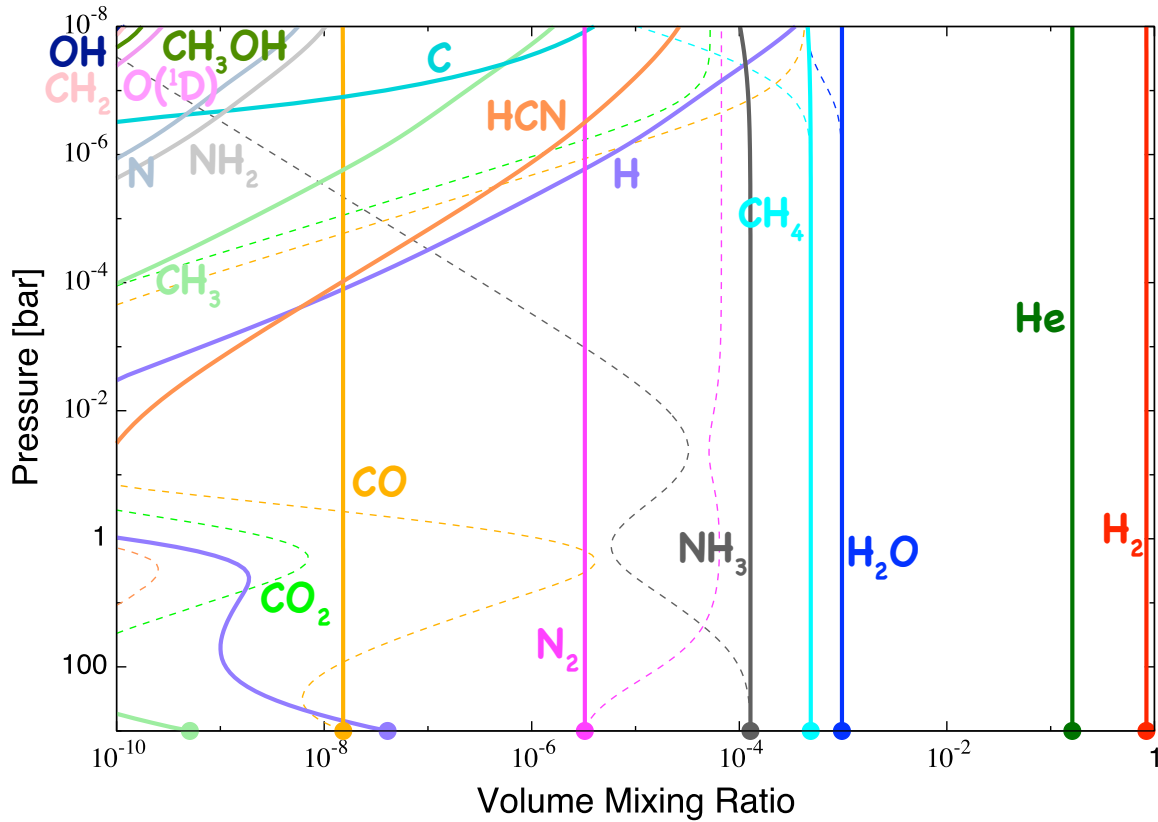
Figure 4.12: Same as Fig. 4.1 but for haze monomer production parameter $\beta = 10^{-5}$.

4.4.2   Particle growth calculations

Figures 4.13, 4.14, 4.15, and 4.16 show the vertical profiles of the surface average radius s_{surf} (orange solid line) and number density n_{surf} (orange dashed line), and the volume average radius s_{vol} (red solid line) and number density n_{vol} (red dashed line) along with that of the monomer mass production rate $\dot{M}$ (green solid line) for four different values of β, 10^5, $10^{2.5}$, $10^{-2.5}$, and 10^{-5}, respectively. The mass densities for all the size bins at each pressure level are also plotted with the blue color contour. The average radii are found to depend on the value of β dramatically: s_{vol} becomes as large as 10^3 μm in the case of $\beta = 10^5$, while it grows only to less than 1 μm in the case of $\beta = 10^{-5}$ at the lower boundary where the pressure is 10 bar. For the high UV cases ($\beta = 10^5$, and $10^{2.5}$), the disagreement between s_{surf} and s_{vol} is significantly larger compared to that in the fiducial case (Fig. 4.5) and one clearly finds bimodal distributions due to the large monomer production rate, as explained in detail below.
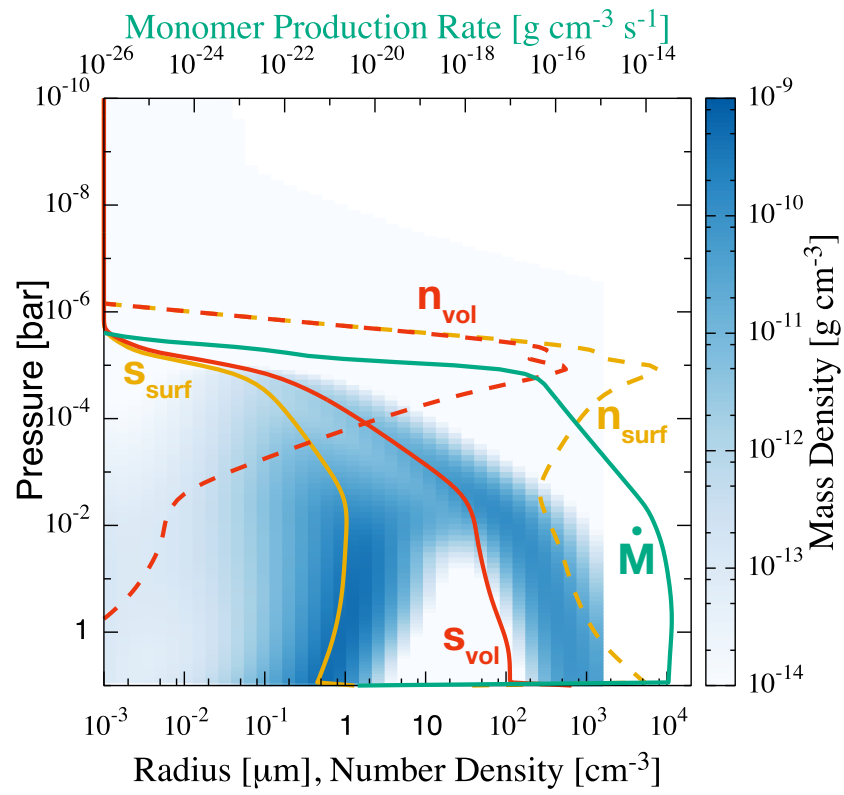
Figure 4.13: Same as Fig. 4.5 but for $\beta = 10^5$. See Eq. (3.9) for the definition of β.
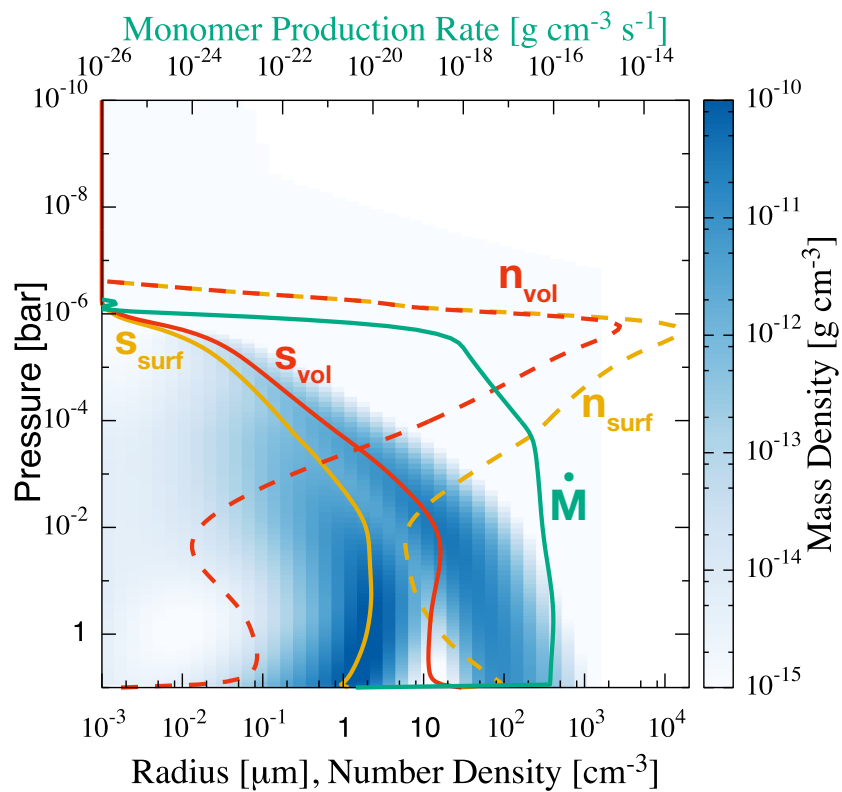
Figure 4.14: Same as Fig. 4.5 but for $\beta = 10^{2.5}$.
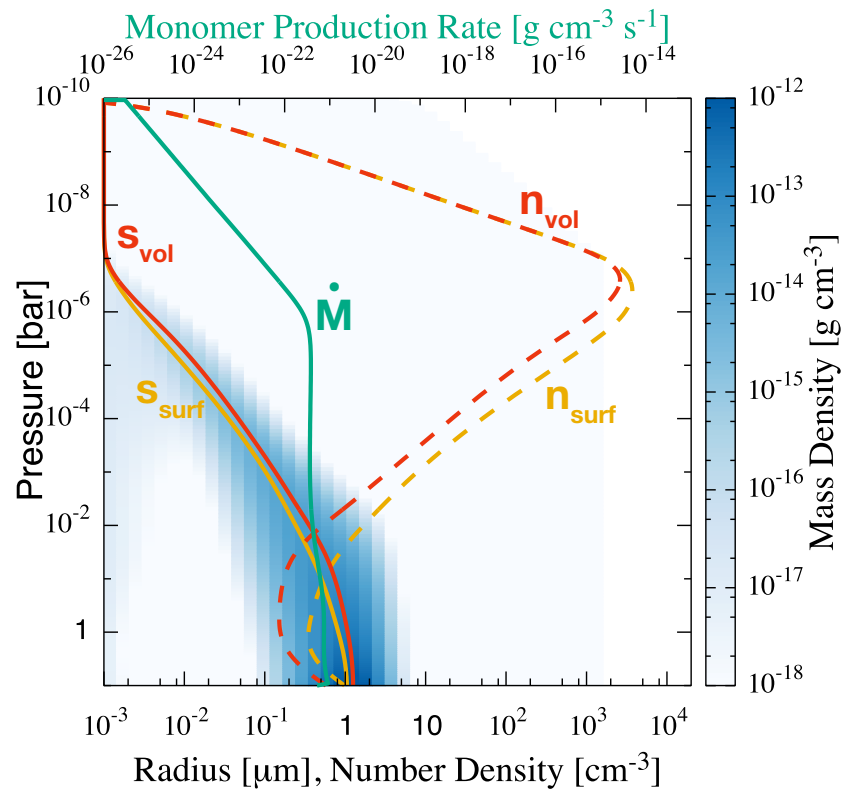
Figure 4.15: Same as Fig. 4.5 but for $\beta = 10^{-2.5}$.
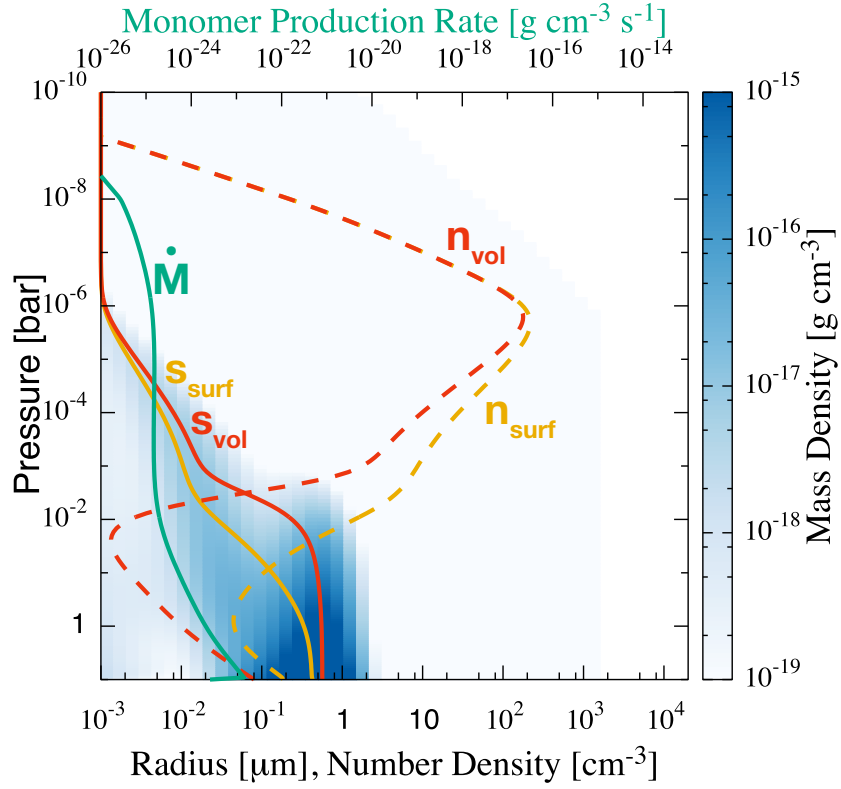
Figure 4.16: Same as Fig. 4.5 but for $\beta = 10^{-5}$.

In Figure 4.17, we plot the distributions of number density for all the size bins at seven different pressure levels, 3.3×10^{-8} bar, 2.3×10^{-7} bar, 8.7×10^{-6} bar, 4.7×10^{-4} bar, 3.9×10^{-2} bar, 0.90 bar, and 10 bar for the case of $\beta = 10^5$. Same as in Fig. 4.6, the slip flow and Stokes regimes are indicated by solid and dashed lines, respectively, and the transition points are marked by filled circles. First, similarly to the case of $\beta = 1$ (Fig. 4.6), the number density of the monomer size, 10^{-3} μm, is the largest at all the pressure levels, because of the large monomer production rate. Like in the fiducial case, for $P \lesssim 10^{-5}$ bar, the coagulation due to brownian diffusion is the dominant process, whereas that due to gravitational collection hardly occurs. On the other hand, at high pressures of $P \gtrsim 10^{-5}$ bar, both coagulation mechanisms contribute to the particle growth. One finds a bimodal distribution with a wide gap whose center is around 40 μm for 3.9×10^{-2} bar, 0.90 bar, and 10 bar (note that the vertical range of Fig. 4.17 differs greatly from that of Fig. 4.6). In contrast to the fiducial case, the particle growth proceeds rapidly as a whole and, then, the large-size particles ($\gtrsim$ 400 μm) enter to the Stokes regime (see the green line) before development of any peak like ones observed in Fig. 4.6. Thus, the largest-size ($\gtrsim$ 400 μm) group stops growing and the small particles

in the slip flow regime (40 μm $\lesssim s \lesssim$ 400 μm) grow and catch up with the largest ($\gtrsim$ 400 μm) particles in the Stokes regime. However, in this case, even relatively small ($\lesssim$ 40 μm) particles are already in the Stokes regime at 3.9×10^{-2} bar, 0.90 bar, and 10 bar. Thus, the transition points place limits on growth for these relatively small particles. The reason why the gap continues to deepen is that smaller particles settle more slowly than larger ones in the Stokes regime.
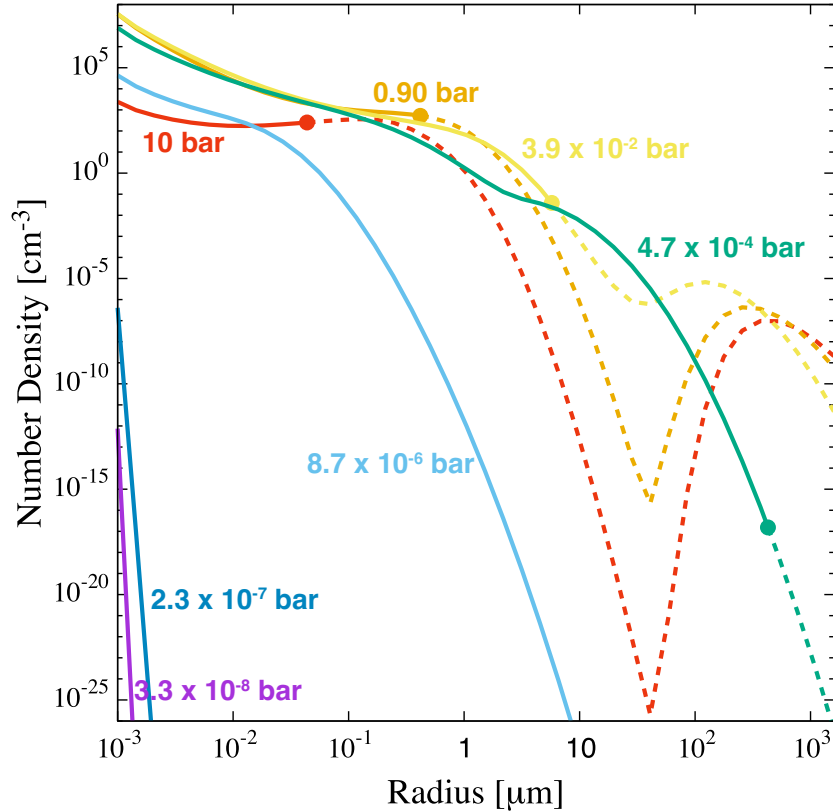
Figure 4.17: Distributions of number density for all the size bins at seven different pressure levels, 3.3×10^{-8} bar (purple line), 2.3×10^{-7} bar (blue line), 8.7×10^{-6} bar (light blue line), 4.7×10^{-4} bar (green line), 3.9×10^{-2} bar (yellow line), 0.90 bar (orange line), and 10 bar (red line) for the case of $\beta = 10^5$. The Stokes regime is indicated by dashed lines, while the slip flow regime is indicated by solid lines; The transition points are marked by filled circles.

In Figure 4.18, we plot the distributions of mass density for all the size bins at the same seven different pressure levels as shown in Fig. 4.17 for the case of $\beta = 10^5$. In contrast to the case of $\beta = 1$ (Fig. 4.7), the distribution is clearly bimodal for the pressure levels, 3.9×10^{-2} bar, 0.15 bar, and 10 bar. The distributions of mass density are qualitatively similar to those of number density (Fig. 4.17). The obvious difference

is that the two peaks of mass density are comparable in value.
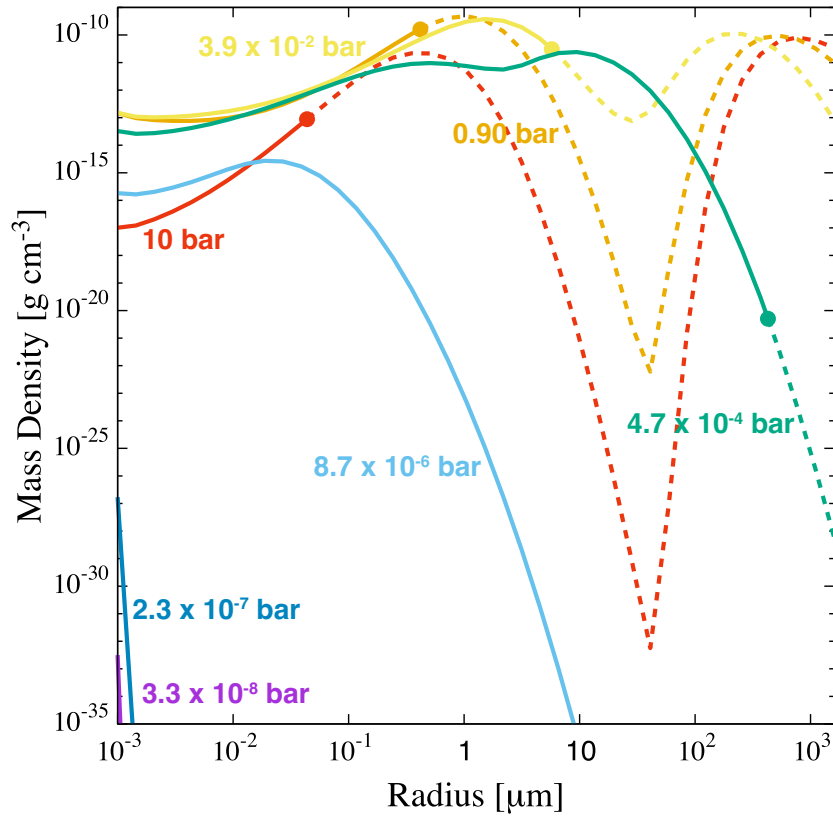
Figure 4.18: Same as Fig. 4.17 but the distribution of mass density.

4.4.3   Transmission spectrum models

Figure 4.19 shows the transmission spectrum models for the atmosphere with haze for the five cases where β is 10^5 (red line), $10^{2.5}$ (yellow line), 1 (green line, same as the green line in Fig. 4.8), $10^{-2.5}$ (blue line), and 10^{-5} (purple line). The transmission spectrum model for the atmosphere without haze in the case of $\beta = 1$ (black line) is also plotted, but can be hardly seen as it overlaps with that for the atmosphere with haze for $\beta = 10^{-5}$ (purple line). Similarly to Fig. 4.8, the horizontal dotted lines represent the transit depths corresponding to the pressure levels from 1×10^{-6} bar to 1 bar for the atmosphere in the case of $\beta = 1$. From this figure, we can see that the transmission spectrum varies with the value of β significantly. In the case of $\beta = 10^5$ (red line), the overall spectrum is rather flat. This is because the floating haze particles at high altitudes ($P \sim 10^{-5}$ bar) make the atmosphere so optically thick that their absorption obscures spectral absorption features due to the molecules in the lower ($P \gtrsim 10^{-5}$ bar)

atmosphere. Also, it turns out that the bimodal size distribution seen in the range of $P \gtrsim 10^{-5}$ bar (see Fig. 4.13) hardly affects the resultant transmission spectrum. In the case of $\beta = 10^{2.5}$ (yellow line), some features of the haze can been seen, which include the spectral slope due to Rayleigh scattering in the optical and the absorption features at 3.0 μm and 4.6 μm coming from the vibrational transitions of the C-H and C≡N bonds, respectively. As β decreases, the overall transit depth becomes lower. This is because the altitude at which the atmosphere becomes optically thick also decreases. In the case of $\beta = 10^{-5}$ (purple line), the spectrum is almost the same as that of the atmosphere without haze (black line). In conclusion, these results demonstrate that the difference in monomer production rate, which relates to the UV irradiation intensity from the host star, makes the diversity of transmission spectrum: completely flat spectrum, spectrum with only extinction features of hazes (i.e., spectral slope due to Rayleigh scattering and absorption features of hazes), spectrum with slope due to Rayleigh scattering and some molecular absorption features, and spectrum with only molecular absorption features.
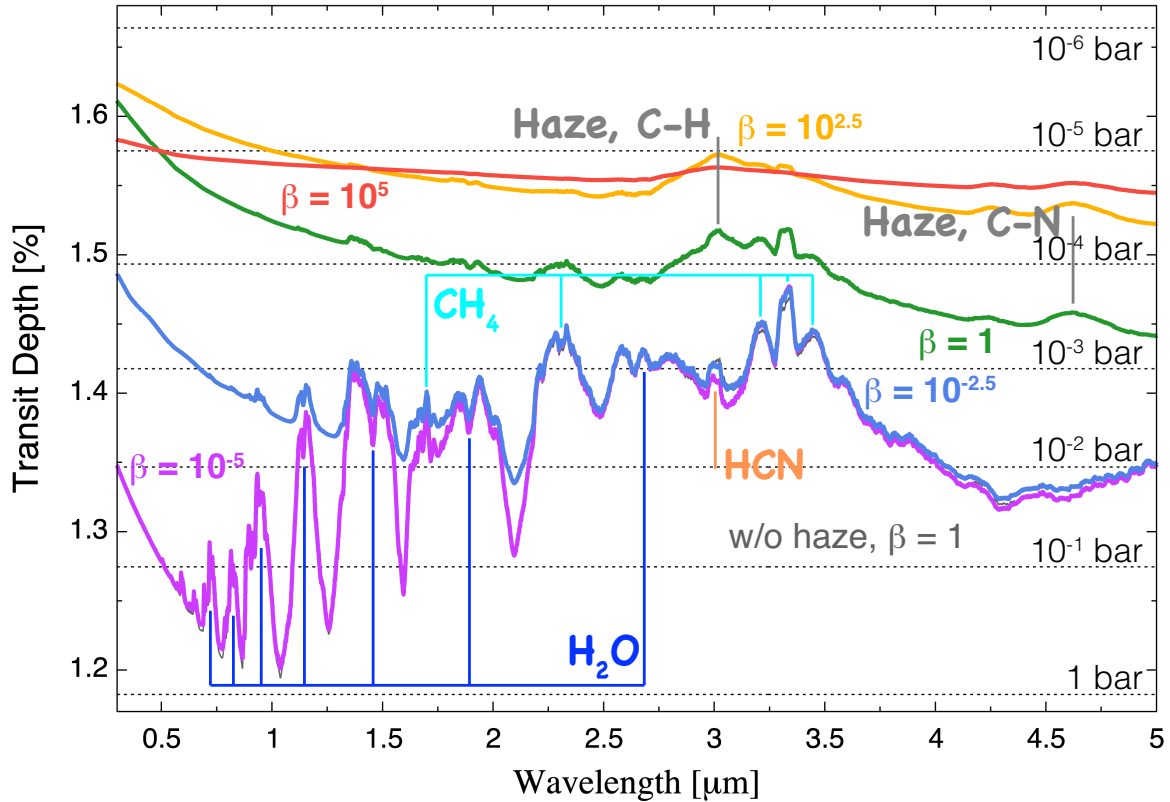
Figure 4.19: Transmission spectrum models for the atmosphere with haze for the five cases where β is 10^5 (red line), $10^{2.5}$ (yellow line), 1 (green line, same as the green line in Fig. 4.8), $10^{-2.5}$ (blue line), and 10^{-5} (purple line). The transmission spectrum model for the atmosphere without haze in the case of $\beta = 1$ (black line) is also plotted, but can be hardly seen as it overlaps with that for the atmosphere with haze in the case of $\beta = 10^{-5}$ (purple line). Same as Fig. 4.8, horizontal dotted lines represent the transit depths corresponding to the pressure levels from 1×10^{-6} bar to 1 bar for the atmosphere without haze in the case of $\beta = 1$. Note that the transmission spectrum models are smoothed for clarity.

4.5 Dependence on UV irradiation intensity for carbon-limited case

本章の以下の部分については、５年以内に雑誌掲載等の形で刊行されるため非公開とする。

Chapter 5

Validity of Characteristic Size Approximation in Particle Growth Calculation

When comparing theoretical transmission spectra of hazy atmospheres with high-precision observational data, the distribution of haze particles has to be determined with multiple-size growth calculations (§ 3.3). To explore the possibility of reducing the computational cost and understand the effect of bimodality on transmission spectra, we examine the validity of characteristic size approximation quantitatively, applying the grain growth model of Ormel (2014). The characteristic size approximation assumes that there are particles of a single size and monomers in the atmosphere. This approximation is validated, at least, in the studies of the dynamics of dust grains in protoplanetary disks (Okuzumi et al., 2011) and proto-envelopes of gas giants (Ormel, 2014).

Below, we describe the characteristic-size-assumed particle growth model in § 5.1 and then present the results in § 5.2.

5.1 Characteristic-size-assumed particle growth model

Before explaining the details of this model, we first describe the assumptions and treatments made in this model. Because focusing on the effect of size distribution, we neglect the gravitational collection and eddy diffusion, which are included in our particle growth module developed in § 3.3. Thus, we assume that coagulation occurs due to the Brownian collision only.

In Figures 5.1, 5.2, and 5.3, we show the ertical profiles of the volume average ra-

dius s_{vol} (solid line) and number density n_{vol} (dashed line) obtained with the model that includes both gravitational collection and eddy diffusion (red lines), one that include gravitational collection but ignores eddy diffusion (blue lines), one that include eddy diffusion but ignores gravitational collection (green lines), one that ignores both gravitational collection and eddy diffusion (purple lines) for $\beta = 10^5$ for $\beta = 10^5$, 1, and 10^{-5}, respectively. The gravitational collection is important when both small and large particles are abundant. Thus, as shown in Fig. 5.1, this has a significant influence on the vertical profile of haze particles in the case of $\beta = 10^5$. However, as also shown above because the altitude where gravitational collection becomes important is optically thick enough for transmitted radiation, the exclusion of gravitational collection has a little effect on resultant transmission spectra. Also, as the particle transport mechanism, we take only gravitational sedimentation into account and ignore eddy diffusion. While the eddy diffusion affects the vertical profile of haze particles in the lower atmosphere in the case of $\beta = 10^{-5}$ to some extent (see Fig. 5.3), we ignore the effect because we want to focus on the effect of size distribution.
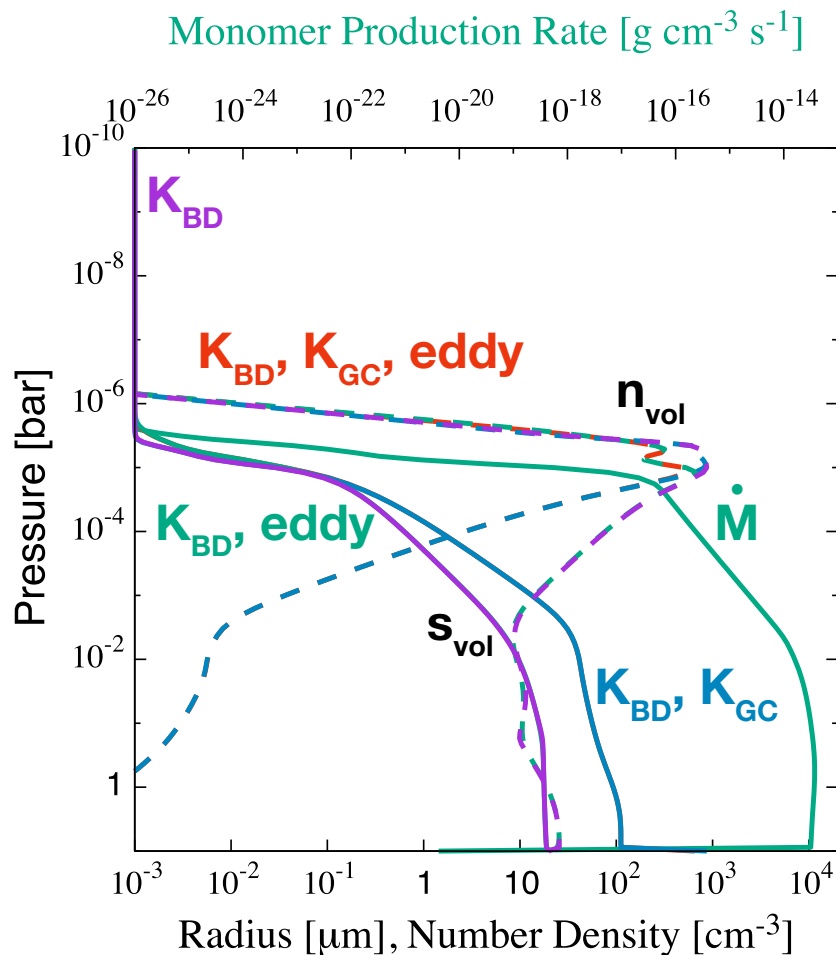
Figure 5.1: Vertical profiles of the volume average radius s_{vol} (solid line) and number density n_{vol} (dashed line) obtained with the model that includes both gravitational collection and eddy diffusion (red lines), one that include gravitational collection but ignores eddy diffusion (blue lines), one that include eddy diffusion but ignores gravitational collection (green lines), one that ignores both gravitational collection and eddy diffusion (purple lines) for $\beta = 10^5$. Also, vertical profile of the monomer mass production rate are plotted with green solid line. Note that red lines and green lines can be hardly seen as they overlaps with blue liens and purple lines, respectively, in most of the region.
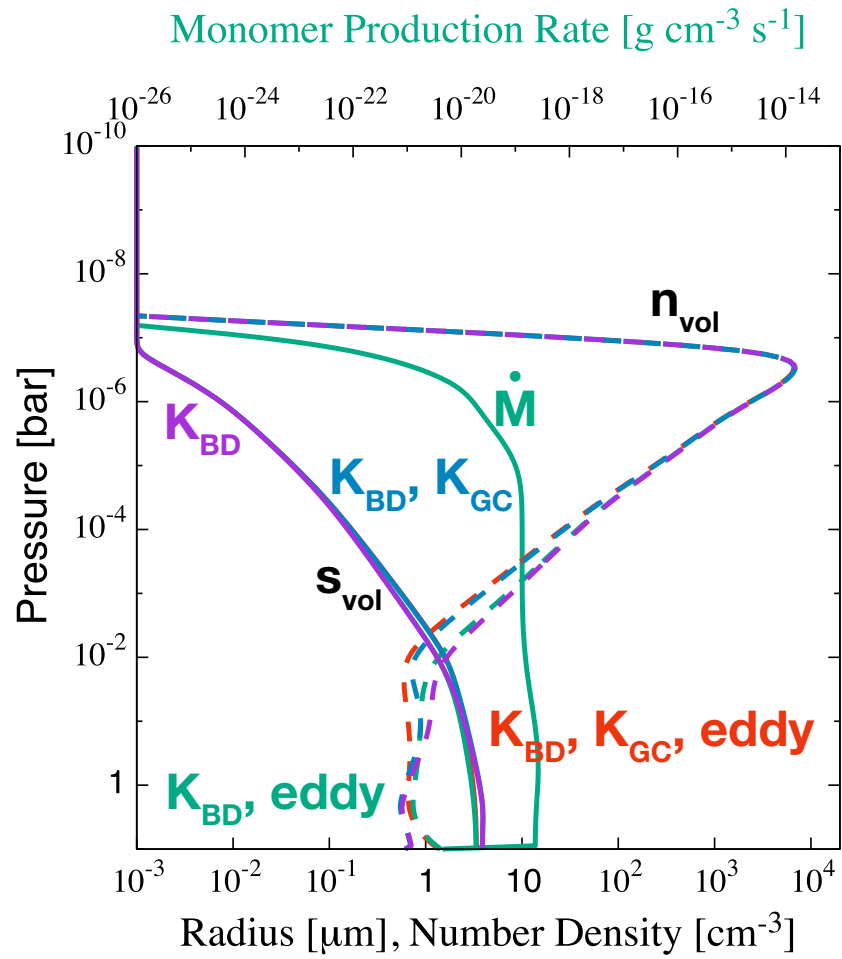
Figure 5.2: Same as Fig. 5.1, but for $\beta = 1$.
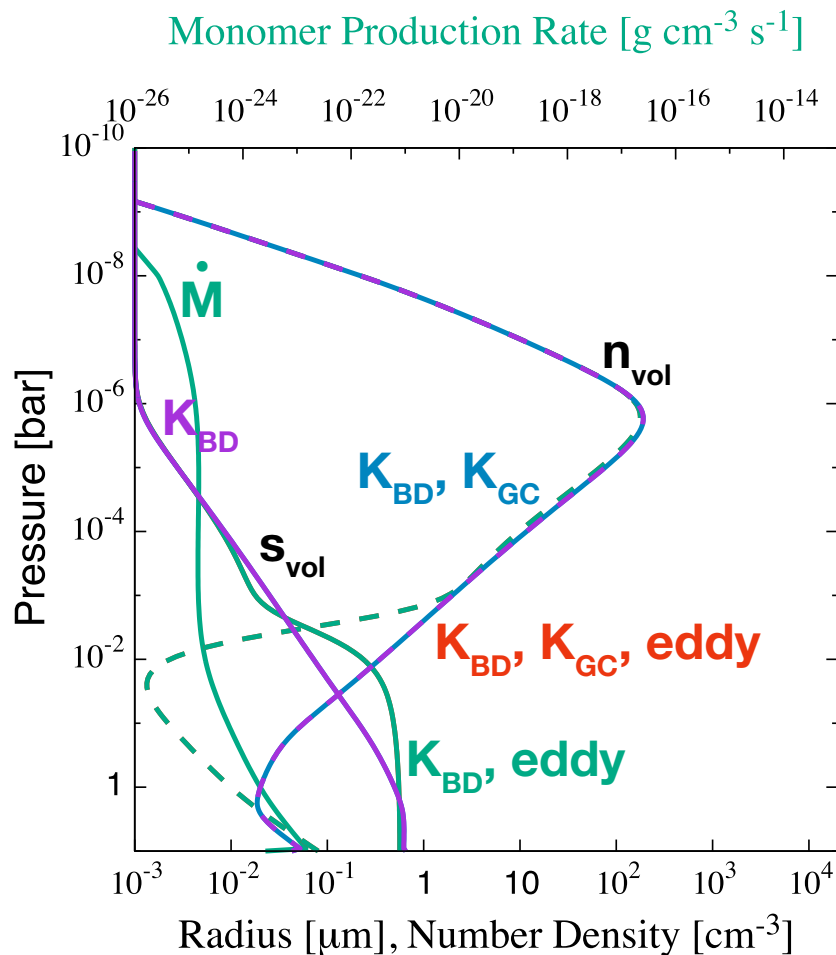
Figure 5.3: Same as Fig. 5.1, but for $\beta = 10^{-5}$. Note that red lines and blue lines can be hardly seen as they overlaps with green liens and blue lines, respectively, in most of the region.

Figure 5.4 shows the transmission spectrum models for the atmosphere with haze for the five cases where β is 10^5 (red line), $10^{2.5}$ (yellow line), 1 (green line), $10^{-2.5}$ (blue line), and 10^{-5} (purple line). Models obtained from the multiple size calculations with and without two effects (gravitational collection and eddy diffusion) are shown with thick and thin lines, respectively. The model for the haze-free atmosphere for $\beta = 1$ (black line) is also plotted. Same as Fig. 4.8, the horizontal dotted lines represent the transit depths corresponding to the pressure levels from 1×10^{-6} bar to 1 bar for the atmosphere without haze in the case of $\beta = 1$. The maximum differences in transit depth between the two models in the wavelength range of 0.3-5 μm are 38, 64, 43, 202, and 85ppm for $\beta = 10^5$, $10^{2.5}$, 1, $10^{-2.5}$, and 10^{-5}, respectively. The relatively large difference for $\beta = 10^{-2.5}$ case comes from the eddy diffusion effect.

Figure 5.4: Transmission spectrum models for the atmosphere with haze for the five cases where the haze monomer production parameter β is 10^5 (red lines), $10^{2.5}$ (yellow lines), 1 (green lines), $10^{-2.5}$ (blue lines), and 10^{-5} (purple lines). Models obtained from the multiple size calculations with and without two effects (gravitational collection and eddy diffusion) are shown with thick and thin lines, respectively. Transmission spectrum model for the atmosphere without haze in the case of $\beta = 1$ (black line) is also plotted. Same as Fig. 4.8, the horizontal dotted lines represent the transit depths corresponding to the pressure levels from 1×10^{-6} bar to 1 bar for the atmosphere without haze in the case of $\beta = 1$. Note that the transmission spectra are smoothed for clarity.

We assume that the haze particle size distribution at any altitude z is characterized by a characteristic mass m^*, defined as (Ormel, 2014)

$$m^* \equiv \frac{\int \xi(m,t)\, m\, \mathrm{d}m}{\int \xi(m,t)\, \mathrm{d}m}, \tag{5.1}$$

where $\xi(m)$ is the distribution function of particles of mass m. Temporal change in m^*

at position z is calculated as

$$\frac{\partial m^*}{\partial t} = \rho^{-1}\left(\int m\frac{\partial \xi}{\partial t}\mathrm{d}m - m^*\int \frac{\partial \xi}{\partial t}\mathrm{d}m\right), \tag{5.2}$$

where ρ is the mass density of particles, defined by

$$\rho(t) \equiv \int \xi(m,t)\,\mathrm{d}m. \tag{5.3}$$

Here we divide the change in the distribution function ξ into three contributions, namely changes due to advection, collisional growth and monomer production:

$$\begin{aligned}\frac{\partial m^*}{\partial t} &= V_s\frac{\partial m^*}{\partial z} + \frac{\partial m^*}{\partial t}\bigg|_{\mathrm{grow}}\\&+ \rho^{-1}\left(\int m\,\frac{\partial \xi}{\partial t}\bigg|_{\mathrm{prod}}\mathrm{d}m - m^*\int \frac{\partial \xi}{\partial t}\bigg|_{\mathrm{prod}}\mathrm{d}m\right),\end{aligned} \tag{5.4}$$

where V_s is the sedimentation velocity of haze particles and given by Eq. (3.22). Note that we neglect the eddy diffusion as mentioned at the beginning of this subsection. The calculation method we describe below is basically the same as the one that Ormel (2014) developed for calculating the opacity of dust grains in accreting envelopes of proto-gas giants.

The collisional growth rate can be written as

$$\frac{\partial m^*}{\partial t}\bigg|_{\mathrm{grow}} \simeq \frac{m^*}{t_{\mathrm{grow}}}, \tag{5.5}$$

where t_{grow} is a mean collision time. Assuming mutual collision of rigid spherical particles of mass m^*,

$$t_{\mathrm{grow}} = \frac{1}{4\pi s^{*2}\,n^*\,\Delta v}, \tag{5.6}$$

where s^* and Δv are the radius and relative velocity of the haze particles, respectively. n^* is the number density of the haze particles and defined as

$$n^* = \frac{\rho}{m^*}. \tag{5.7}$$

As mentioned at the beginning of this subsection, we assume that coagulation occurs

due to the Brownian collision only and neglect the gravitational collection. Thus,

$$\Delta v = \sqrt{16 k_{\mathrm{B}} T / \pi m^*}. \tag{5.8}$$

In equation (5.4), the third and fourth terms on the righthand side represent the mass production rate of monomers,

$$\dot{\rho} = \int \left. \frac{\partial \xi}{\partial t} \right|_{\mathrm{prod}} \mathrm{d}m, \tag{5.9}$$

and the produced monomer mass

$$m_1 = \dot{\rho}^{-1} \int m \left. \frac{\partial \xi}{\partial t} \right|_{\mathrm{prod}} \mathrm{d}m. \tag{5.10}$$

We introduce the cumulative mass flux of monomers integrated from the top of the atmosphere, defined by

$$\dot{M}_{\mathrm{prod}} \equiv - \int_{\infty}^{z} \dot{\rho} \, \mathrm{d}z' \quad \text{or} \quad \dot{\rho} = - \frac{\partial \dot{M}_{\mathrm{prod}}}{\partial z} \tag{5.11}$$

for convenience of modeling (see below). In a steady state,

$$\rho V_s = \dot{M}_{\mathrm{prod}}. \tag{5.12}$$

Equations (5.5) and (5.9)–(5.12) being used in equation (5.4), the equation for the steady state distribution of m^* is given by

$$\frac{\partial m^*}{\partial z} = - \frac{m^*}{V_s t_{\mathrm{grow}}} + \frac{m_1 - m^*}{\dot{M}_{\mathrm{prod}}} \frac{\partial \dot{M}_{\mathrm{prod}}}{\partial z}. \tag{5.13}$$

5.2 Results

5.2.1 Particle growth calculations
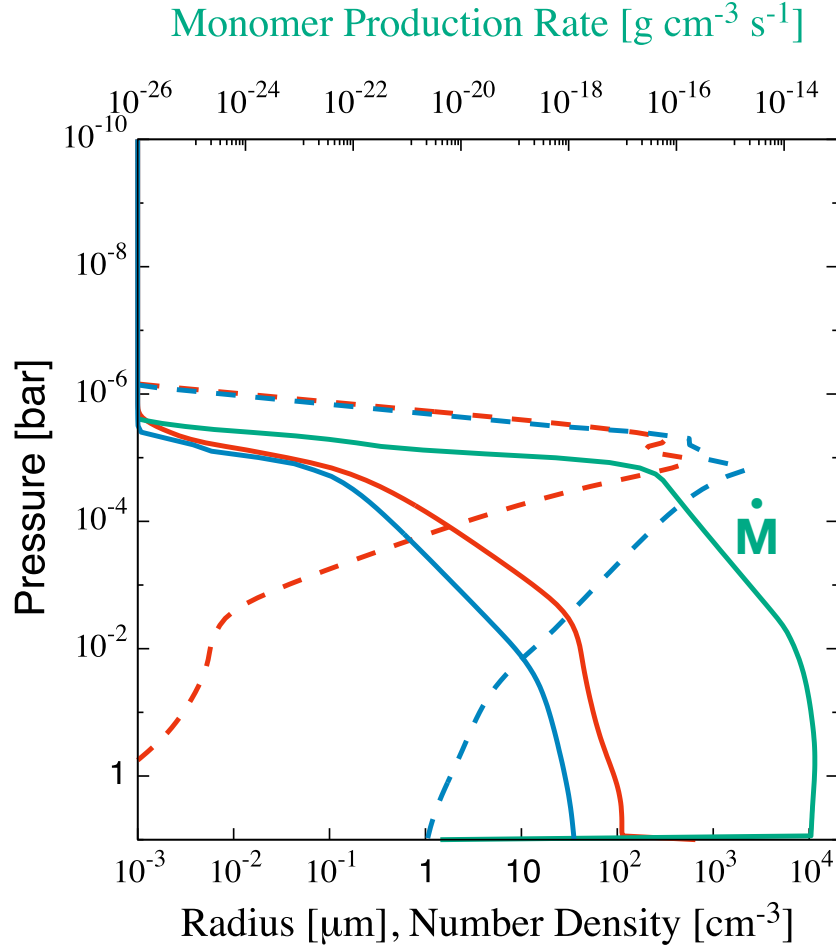
Figure 5.5: Vertical profiles of the characteristic size (blue solid line) and number density (blue dashed line) calculated by characteristic-size-assumed particle growth model and those of the volume average radius s_{vol} (red solid lines) and number density n_{vol} (red dashed line) calculated by the particle growth model of § 3.3 along with that of the monomer mass production rate (green solid line) for the case of $\beta = 10^5$.

Figures 5.5, 5.6, 5.7, 5.8, and 5.9 show the vertical profiles of the characteristic size (blue solid line) and number density (blue dashed line) calculated by characteristic-size-assumed particle growth model and those of the volume average radius s_{vol} (red solid lines) and number density n_{vol} (red dashed line) calculated by the particle growth model of § 3.3 along with that of the monomer mass production rate (green solid line) for five different values of β, 10^5, $10^{2.5}$, 1, $10^{-2.5}$, and 10^{-5}, respectively.. We compare

the characteristic sizes and number densities with those averaged by volume because characteristic mass is determined by the distribution function of particle mass.

The differences between the characteristic and the volume average radius, and those between the characteristic and the volume average number density are larger increasing β.
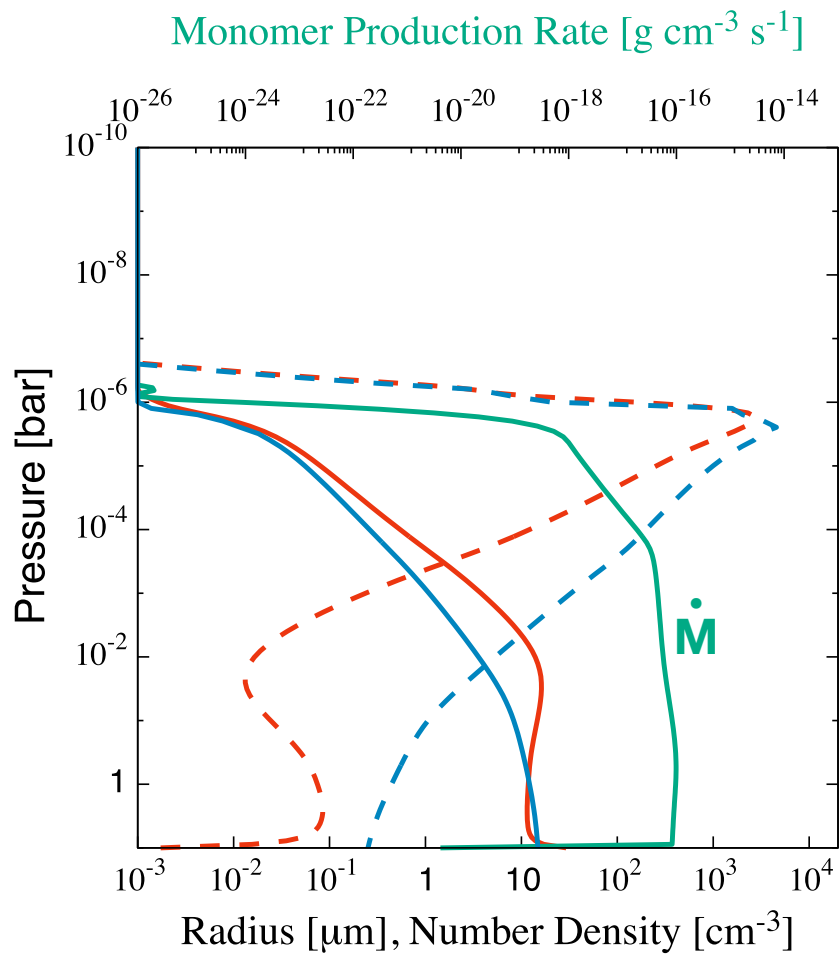
Figure 5.6: Same as Fig. 5.5 but for the case of $\beta = 10^{2.5}$.
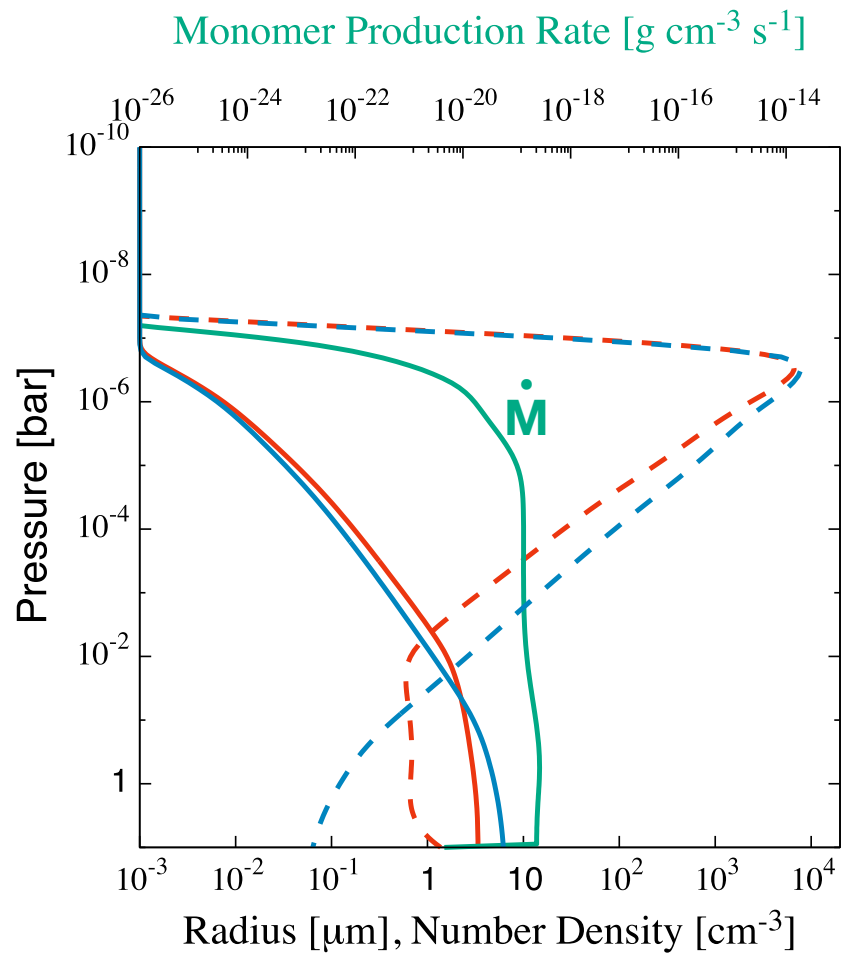
Figure 5.7: Same as Fig. 5.5 but for the case of $\beta = 1$.
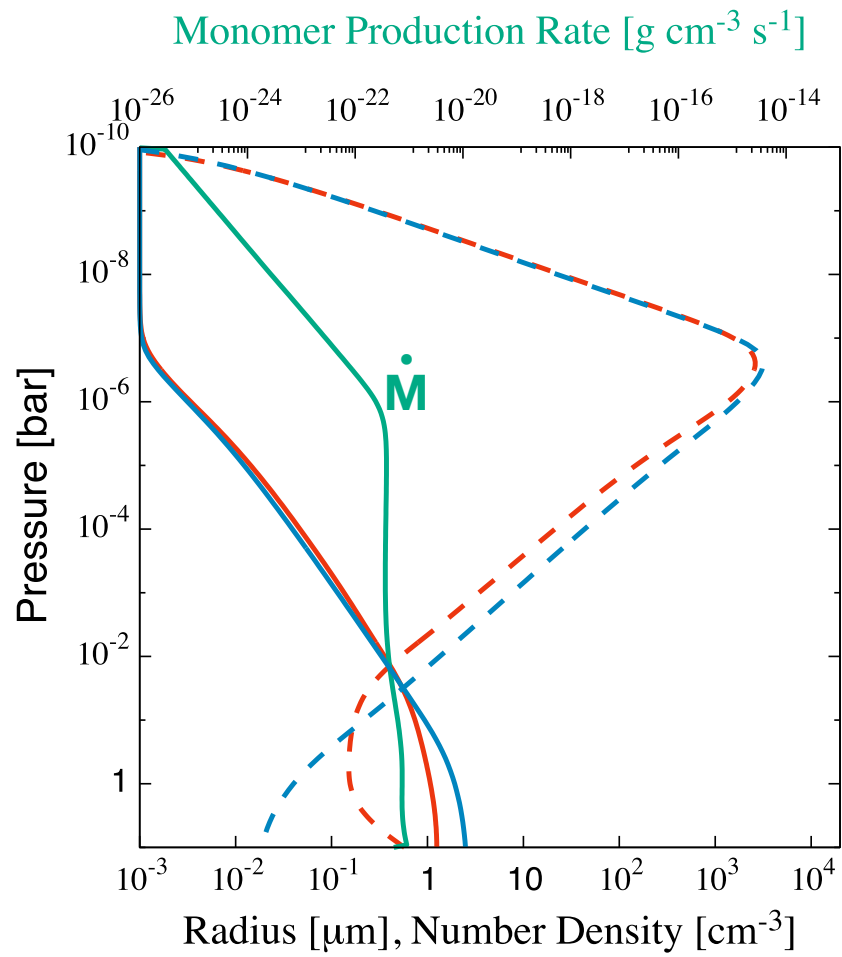
Figure 5.8: Same as Fig. 5.5 but for the case of $\beta = 10^{-2.5}$.
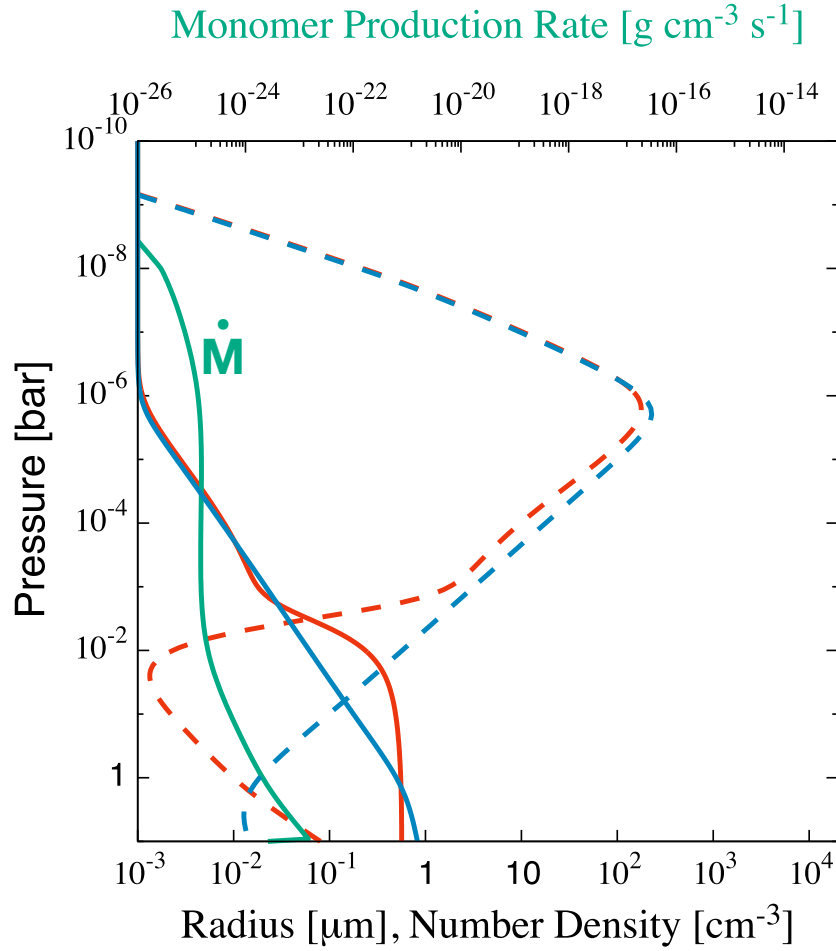
Figure 5.9: Same as Fig. 5.9 but for the case of $\beta = 10^{-5.0}$.

5.2.2 Transmission spectrum models

Figure 5.10 shows the transmission spectrum models for the atmosphere with haze for the five cases where β is 10^5 (red line), $10^{2.5}$ (yellow line), 1 (green line), $10^{-2.5}$ (blue line), and 10^{-5} (purple line). Models obtained from the multiple size calculations (§ 3.3) are shown with thick lines, while those calculated with the characteristic size approximation are plotted with thin lines. The model for the haze-free atmosphere for $\beta = 1$ (black line) is also plotted. Same as Fig. 4.8, the horizontal dotted lines represent the transit depths corresponding to the pressure levels from 1×10^{-6} bar to 1 bar for the atmosphere without haze in the case of $\beta = 1$. Again, we ignore the gravitational collection and eddy diffusion also in the multiple-size particle growth calculations to compare the results from those with the characteristic size approximation.

In the case of $\beta = 10^5$ (red lines), although the size distribution is obviously bimodal

in the lower atmosphere (see Figs. 4.17 and 4.18), the difference between the two spectrum models are very small. This is because haze particles are so abundant that the atmosphere is optically thick at low pressures ($P \sim 10^{-5}$ bar) and therefore the difference in haze particle distribution in the lower atmosphere ($P \gtrsim 10^{-5}$ bar) hardly affects the resultant spectrum. In the case of the intermediate values of $\beta = 10^{2.5}$ (yellow lines), 1 (green lines), and $10^{-2.5}$ (blue lines), the differences between the two models are relatively large, because the size multiplicity is important. In the case of $\beta = 10^{-5}$ (purple lines), the difference in transit depth between the two models are relatively small because of their small abundance of haze in the atmosphere.

The maximum differences in transit depth between the two models in the wavelength range of 0.3-5 μm for $\beta = 10^5$, $10^{2.5}$, 1, $10^{-2.5}$, and 10^{-5} are 87, 205, 393, 393, and 101ppm, respectively. Also, the maximum differences in transit depth between spectrum models obtained from the multiple size calculations with the effects of the gravitational collection and eddy diffusion and those calculated with the characteristic-size calculations without the two effects in the wavelength range of 0.3-5 μm for $\beta = 10^5$, $10^{2.5}$, 1, $10^{-2.5}$, and 10^{-5} are 86, 157, 356, 587, and 38ppm, respectively. Precision of observed transit depths depends on properties of the planet, host star, observational instrument, and so on. If the precision of observed transit depths is larger than the difference in transit depth between the multiple-size models with the two effects (gravitational collection and eddy diffusion) and the characteristic-size models without the two effects, the characteristic size approximation is useful because of its low computational cost and the ignorance of the two effects is appropriate. For example, among the studies of the multi-wavelength transit observation of GJ 1214b, Kreidberg et al. (2014) reported the transit depths with the highest precision of $\sim$ 30ppm using the *Hubble Space Telescope (HST)*. Thus, for this observation, the characteristic size approximation cannot be useful and the ignorance of the two effects is inappropriate. One has to use the multiple-size models with the two effects when calculating the distribution of the haze particles for the spectrum models. On the other hand, for example, Cáceres et al. (2014) reported the transit depths of GJ 1214b with the precisions of 540ppm at I-Bessel band and 170ppm at 2.14 μm from the ground-based transit observations. In this case, the characteristic size approximation is useful and the ignorance of the two effects is appropriate for $\beta = 10^5$, $10^{2.5}$, and 10^{-5} cases.

Recently, to derive the information of planetary atmospheres such as compositions and temperatures from the observed spectra with statistical quantitativeness, retrieval method, based on Bayesian statistics, has come into use. However, the treatments of clouds/haze in previous retrieval models were quite simplified. For example, their

particle size was regarded as a parameter, but the derived parameter was not examined with physical basis. One of the reason is that it is hard to include the computationally-high-cost particle growth calculation in retrieval calculation whose computational cost is also high. The characteristic size approximation raises the possibility to include the particle growth calculation in computationally-high-cost retrieval calculation.
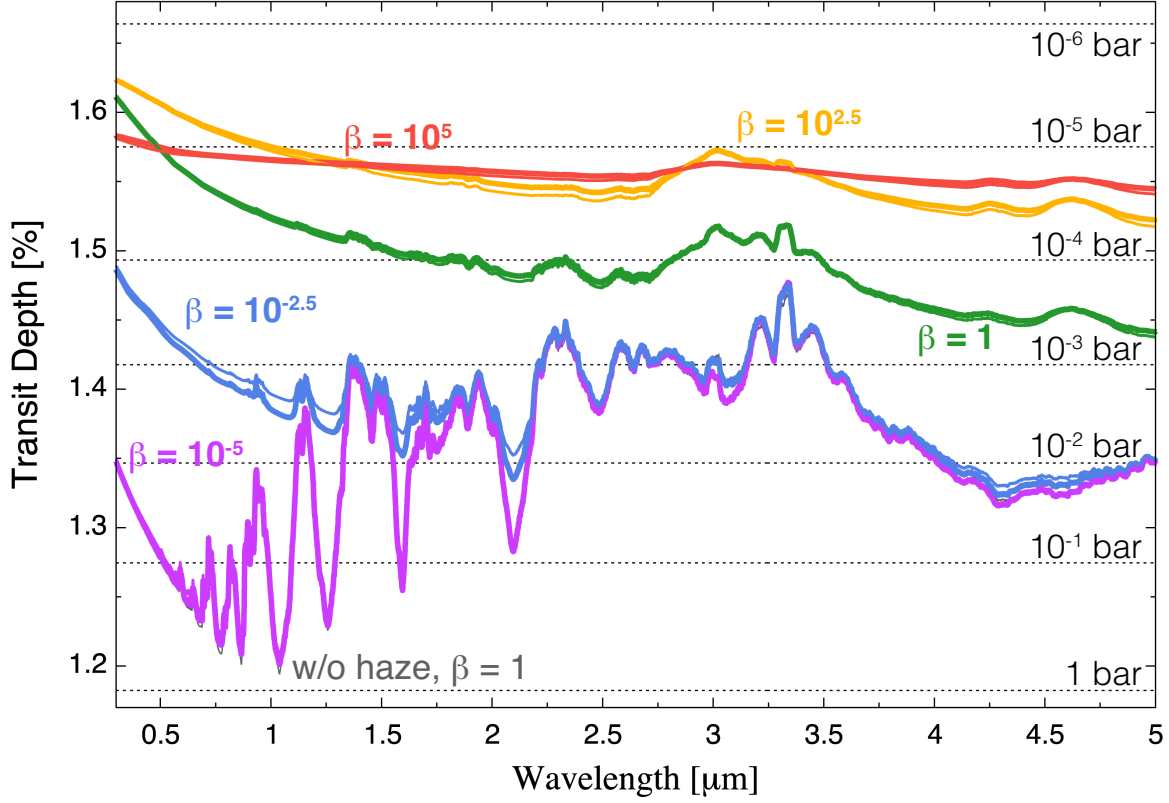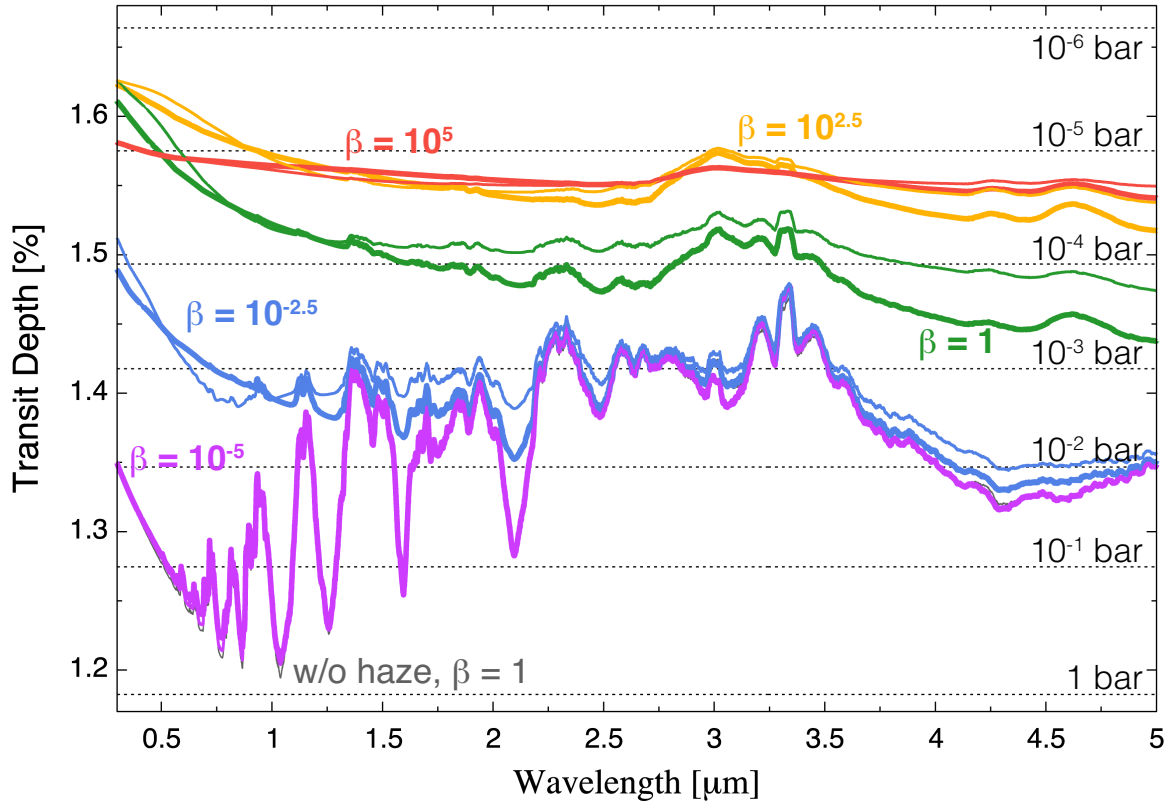
Figure 5.10: Transmission spectrum models for the atmosphere with haze for the five cases where the haze monomer production parameter β is 10^5 (red lines), $10^{2.5}$ (yellow lines), 1 (green lines), $10^{-2.5}$ (blue lines), and 10^{-5} (purple lines). Models obtained from the multiple size calculations (§ 3.3) are shown with thick lines, while those calculated with the characteristic size approximation are plotted with thin lines. Transmission spectrum model for the atmosphere without haze in the case of $\beta = 1$ (black line) is also plotted. Same as Fig. 4.8, the horizontal dotted lines represent the transit depths corresponding to the pressure levels from 1×10^{-6} bar to 1 bar for the atmosphere without haze in the case of $\beta = 1$. Note that the transmission spectra are smoothed for clarity.

Chapter 6

Discussion

本章ついては、5 年以内に雑誌掲載等の形で刊行されるため非公開とする。

Chapter 7

Summary of Part I

本章ついては、5年以内に雑誌掲載等の形で刊行されるため非公開とする。

Part II

Applications of Transmission Spectrum Models of Exoplanet Atmospheres with Hydrocarbon Haze to Multi-Wavelength Transit Observations

Chapter 8

Introduction of Part II

本章ついては、5年以内に雑誌掲載等の形で刊行されるため非公開とする。

Chapter 9

Method Description

本章ついては、5 年以内に雑誌掲載等の形で刊行されるため非公開とする。

Chapter 10

Results

本章ついては、5年以内に雑誌掲載等の形で刊行されるため非公開とする。

Chapter 11

Application to Titan

本章ついては、5 年以内に雑誌掲載等の形で刊行されるため非公開とする。

Chapter 12

Summary of Part II

本章ついては、5年以内に雑誌掲載等の形で刊行されるため非公開とする。

Chapter 13

Conclusions

本章ついては、５年以内に雑誌掲載等の形で刊行されるため非公開とする。

Bibliography

Allen, M., Yung, Y. L., & Waters, J. W. 1981, J. Geophys. Res., 86, 3617

Alonso, R., Barbieri, M., Rabus, M., et al. 2008, A&A, 487, L5

Anglada-Escudé, G., Rojas-Ayala, B., Boss, A. P., Weinberger, A. J., & Lloyd, J. P. 2013, A&A, 551, A48

Armitage, P. J. . 2010, Astrophysics of Planet Formation (New York: Cambridge University Press)

Asplund, M., Grevesse, N., & Sauval, A. J. 2005, in Astronomical Society of the Pacific Conference Series, Vol. 336, Cosmic Abundances as Records of Stellar Evolution and Nucleosynthesis, ed. T. G. Barnes, III & F. N. Bash, 25

Awiphan, S., Kerins, E., Pichadee, S., et al. 2016a, MNRAS, 463, 2574

—. 2016b, MNRAS, 463, 2574

Backx, C., Wight, G. R., & Van der Wiel, M. J. 1976, Journal of Physics B Atomic Molecular Physics, 9, 315

Barman, T. S., Macintosh, B., Konopacky, Q. M., & Marois, C. 2011, ApJ, 733, 65

Bean, J. L., Miller-Ricci Kempton, E., & Homeier, D. 2010, Nature, 468, 669

Bean, J. L., Désert, J.-M., Kabath, P., et al. 2011, ApJ, 743, 92

Beaulieu, J.-P., Tinetti, G., Kipping, D. M., et al. 2011, ApJ, 731, 16

Bénilan, Y., Smith, N., Jolly, A., & Raulin, F. 2000, Planet. Space Sci., 48, 463

Berta, Z. K., Charbonneau, D., Désert, J.-M., et al. 2012, ApJ, 747, 35

Biddle, L. I., Pearson, K. A., Crossfield, I. J. M., et al. 2014, MNRAS, 443, 1810

Bohren, C. F., & Huffman, D. R. 2004, Absorption and Scattering of Light by Small Particles (Weinheim: Wiley-VCH)

Borucki, W. J., & Summers, A. L. 1984, Icarus, 58, 121

Bouchy, F., Udry, S., Mayor, M., et al. 2005, A&A, 444, L15

Brion, C., Tan, K., van der Wiel, M., & van der Leeuw, P. 1979, Journal of Electron Spectroscopy and Related Phenomena, 17, 101

Brown, T. M. 2001, ApJ, 553, 1006

Burton, G. R., Chan, W. F., Cooper, G., & Biron, C. E. 1992, Chemical Physics, 167, 349

Cáceres, C., Ivanov, V. D., Minniti, D., et al. 2009, A&A, 507, 481

Cáceres, C., Kabath, P., Hoyer, S., et al. 2014, A&A, 565, A7

Cantrell, J. R., Henry, T. J., & White, R. J. 2013, AJ, 146, 99

Carter, J. A., Winn, J. N., Holman, M. J., et al. 2011, ApJ, 730, 82

Chan, T., Ingemyr, M., Winn, J. N., et al. 2011, AJ, 141, 179

Chan, W. F., Cooper, G., & Brion, C. E. 1993a, Chemical Physics, 178, 387

—. 1993b, Chemical Physics, 170, 123

Chan, W. F., Cooper, G., Sodhi, R. N. S., & Brion, C. E. 1993c, Chemical Physics, 170, 81

Charbonneau, D., Brown, T. M., Latham, D. W., & Mayor, M. 2000, ApJL, 529, L45

Charbonneau, D., Brown, T. M., Noyes, R. W., & Gilliland, R. L. 2002, ApJ, 568, 377

Charbonneau, D., Berta, Z. K., Irwin, J., et al. 2009, Nature, 462, 891

Chen, F. Z., & Wu, C. Y. R. 2004, JQSRT, 85, 195

Chen, G., Guenther, E. W., Pallé, E., et al. 2017, A&A, 600, A138

Cheng, B.-M., Bahou, M., Lee, Y.-P., & Lee, L. C. 2002, Journal of Geophysical Research (Space Physics), 107, 1161

Cheng, B.-M., Lu, H.-C., Chen, H.-K., et al. 2006, ApJ, 647, 1535

Colón, K. D., & Gaidos, E. 2013, ApJ, 776, 49

Cook, G. R., & Metzger, P. H. 1964, Journal of the Optical Society of America (1917-1983), 54, 968

Cooper, G., Olney, T. N., & Brion, C. E. 1995, Chemical Physics, 194, 175

Croll, B., Albert, L., Jayawardhana, R., et al. 2011, ApJ, 736, 78

Crossfield, I. J. M., Barman, T., Hansen, B. M. S., & Howard, A. W. 2013, A&A, 559, A33

Davies, C. N. 1945, Proceedings of the Physical Society, 57, 259

de Mooij, E. J. W., Brogi, M., de Kok, R. J., et al. 2012, A&A, 538, A46

—. 2013, ApJ, 771, 109

Demory, B.-O., Torres, G., Neves, V., et al. 2013, ApJ, 768, 154

Désert, J.-M., Bean, J., Miller-Ricci Kempton, E., et al. 2011, ApJL, 731, L40

Dragomir, D., Benneke, B., Pearson, K. A., et al. 2015, ApJ, 814, 102

Ehrenreich, D., Bonfils, X., Lovis, C., et al. 2014, A&A, 570, A89

Fischer, J., Gamache, R. R., Goldman, A., Rothman, L. S., & Perrin, A. 2003, JQSRT, 82, 401

Fraine, J. D., Deming, D., Gillon, M., et al. 2013, ApJ, 765, 127

France, K., Parke Loyd, R. O., Youngblood, A., et al. 2016, ApJ, 820, 89

Fukui, A., Narita, N., Kurosaki, K., et al. 2013, ApJ, 770, 95

Fukui, A., Kawashima, Y., Ikoma, M., et al. 2014, ApJ, 790, 108

Grassi, T., Bovino, S., Schleicher, D. R. G., et al. 2014, MNRAS, 439, 2386

Gray, D. F. 1992, The observation and analysis of stellar photospheres.

Guillot, T. 2010, A&A, 520, A27

Haynes, W. M. 2012, CRC HANDBOOK OF CHEMISTRY and PHYSICS, 92nd edn. (CRC Press)

Hebb, L., Collier-Cameron, A., Loeillet, B., et al. 2009, ApJ, 693, 1920

Helling, C., & Woitke, P. 2006, A&A, 455, 325

Heng, K. 2016, ApJL, 826, L16

Heng, K., & Kitzmann, D. 2017, MNRAS, 470, 2972

Henry, G. W., Marcy, G. W., Butler, R. P., & Vogt, S. S. 2000, ApJL, 529, L41

Hindmarsh, A. C. 1982, IMACS Trans. Sci. Comput., 1, 55

Howe, A. R., & Burrows, A. S. 2012, ApJ, 756, 176

Hu, R., Seager, S., & Bains, W. 2012, ApJ, 761, 166

Huestis, D. L., & Berkowitz, J. 2010, in Bulletin of the American Astronomical Society, Vol. 42, AAS/Division for Planetary Sciences Meeting Abstracts #42, 972

Husser, T.-O., Wende-von Berg, S., Dreizler, S., et al. 2013, A&A, 553, A6

Ityaksov, D., Linnartz, H., & Ubachs, W. 2008, Chemical Physics Letters, 462, 31

Jacobson, M. Z. M. Z. 2005, Fundamentals of atmospheric modeling / Mark Z. Jacobson, 2nd edn., Vol. : pbk; : hard (New York: Cambridge University Press), xiv, 813 p.

Kalas, P., Graham, J. R., Chiang, E., et al. 2008, Science, 322, 1345

Kameta, K., Kouchi, N., Ukai, M., & Hatano, Y. 2002, Journal of Electron Spectroscopy and Related Phenomena, 123, 225 , determination of cross-sections and momentum profiles of atoms, molecules and condensed matter

Kataria, T., Showman, A. P., Fortney, J. J., Marley, M. S., & Freedman, R. S. 2014, ApJ, 785, 92

Khare, B. N., Sagan, C., Arakawa, E. T., et al. 1984, Icarus, 60, 127

Kirkpatrick, J. D., Henry, T. J., & McCarthy, Jr., D. W. 1991, ApJS, 77, 417

Knutson, H. A., Benneke, B., Deming, D., & Homeier, D. 2014, Nature, 505, 66

Knutson, H. A., Madhusudhan, N., Cowan, N. B., et al. 2011, ApJ, 735, 27

Kockarts, G. 1976, Planet. Space Sci., 24, 589

Kopparapu, R. k., Kasting, J. F., & Zahnle, K. J. 2012, ApJ, 745, 77

Krasnopolsky, V. A. 2009, Icarus, 201, 226

Kreidberg, L., Bean, J. L., Désert, J.-M., et al. 2014, Nature, 505, 69

Kuntz, M. 1997, JQSRT, 57, 819

Lanotte, A. A., Gillon, M., Demory, B.-O., et al. 2014, A&A, 572, A73

Läuter, A., Lee, K. S., Jung, K. H., et al. 2002, Chemical Physics Letters, 358, 314

Lavvas, P., Yelle, R. V., & Griffith, C. A. 2010, Icarus, 210, 832

Lavvas, P., Yelle, R. V., & Vuitton, V. 2009, Icarus, 201, 626

Lecavelier Des Etangs, A., Pont, F., Vidal-Madjar, A., & Sing, D. 2008, A&A, 481, L83

Lee, A. Y. T., Yung, Y. L., Cheng, B.-M., et al. 2001, ApJL, 551, L93

Lee, L. C., Carlson, R. W., & Judge, D. L. 1976, JQSRT, 16, 873

Lépine, S., Hilton, E. J., Mann, A. W., et al. 2013, AJ, 145, 102

Lewis, N. K., Showman, A. P., Fortney, J. J., et al. 2010, ApJ, 720, 344

Lilly, R., Rebbert, R., & Ausloos, P. 1973, Journal of Photochemistry, 2, 49

Line, M. R., Vasisht, G., Chen, P., Angerhausen, D., & Yung, Y. L. 2011, ApJ, 738, 32

Linsky, J. L., Fontenla, J., & France, K. 2014, ApJ, 780, 61

Linsky, J. L., France, K., & Ayres, T. 2013, ApJ, 766, 69

Liou, K. N. 2002, An Introduction to Atmospheric Radiation, 2nd edn. (Amsterdam: Academic Press)

Lissauer, J. J., Fabrycky, D. C., Ford, E. B., et al. 2011, Nature, 470, 53

Lodders, K. 2003, ApJ, 591, 1220

Lodders, K., Palme, H., & Gail, H.-P. 2009, Landolt Börnstein, arXiv:0901.1149

Loyd, R. O. P., France, K., Youngblood, A., et al. 2016, ApJ, 824, 102

Lurie, J. C., Henry, T. J., Jao, W.-C., et al. 2014, AJ, 148, 91

Macpherson, M. T., & Simons, J. P. 1978, J. Chem. Soc., Faraday Trans. 2, 74, 1965

Mancini, L., Southworth, J., Ciceri, S., et al. 2014, A&A, 562, A126

Marois, C., Macintosh, B., Barman, T., et al. 2008, Science, 322, 1348

Mayor, M., & Queloz, D. 1995, Nature, 378, 355

McKay, C. P., Coustenis, A., Samuelson, R. E., et al. 2001, Planet. Space Sci., 49, 79

Mentall, J. E., & Gentieu, E. P. 1970, JChPh, 52, 5641

Mie, G. 1908, Annalen der Physik, 330, 377

Miguel, Y., & Kaltenegger, L. 2014, ApJ, 780, 166

Miller-Ricci, E., & Fortney, J. J. 2010, ApJL, 716, L74

Miller-Ricci Kempton, E., Zahnle, K., & Fortney, J. J. 2012, ApJ, 745, 3

Morley, C. V., Fortney, J. J., Kempton, E. M.-R., et al. 2013, ApJ, 775, 33

Moses, J. I., Visscher, C., Fortney, J. J., et al. 2011, ApJ, 737, 15

Moses, J. I., Line, M. R., Visscher, C., et al. 2013, ApJ, 777, 34

Murgas, F., Pallé, E., Cabrera-Lavers, A., et al. 2012, A&A, 544, A41

Narita, N., Nagayama, T., Suenaga, T., et al. 2013a, PASJ, 65, 27

Narita, N., Fukui, A., Ikoma, M., et al. 2013b, ApJ, 773, 144

Nascimbeni, V., Piotto, G., Pagano, I., et al. 2013, A&A, 559, A32

Nascimbeni, V., Mallonn, M., Scandariato, G., et al. 2015a, A&A, 579, A113

—. 2015b, A&A, 579, A113

Nee, J. B., Suto, M., & Lee, L. C. 1985, Chemical Physics, 98, 147

Öberg, K. I., Murray-Clay, R., & Bergin, E. A. 2011, ApJL, 743, L16

Ogawa, S., & Ogawa, M. 1975, Canadian Journal of Physics, 53, 1845

Okuzumi, S., Tanaka, H., Takeuchi, T., & Sakagami, M.-a. 2011, ApJ, 731, 95

Ormel, C. W. 2014, ApJL, 789, L18

Petty, G. W. 2006, A First Course in Atmospheric Radiation, 2nd edn. (Madison, Wis.: Sundog Pub.)

Pickles, A. J. 1998, PASP, 110, 863

Pont, F., Gilliland, R. L., Knutson, H., Holman, M., & Charbonneau, D. 2009, MNRAS, 393, L6

Rackham, B., Espinoza, N., Apai, D., et al. 2017, ApJ, 834, 151

Robinson, T. D., Maltagliati, L., Marley, M. S., & Fortney, J. J. 2014, Proceedings of the National Academy of Science, 111, 9042

Rothman, L. S., Rinsland, C. P., Goldman, A., et al. 1998, JQSRT, 60, 665

Rothman, L. S., Gordon, I. E., Babikov, Y., et al. 2013, JQSRT, 130, 4

Ruyten, W. 2004, JQSRT, 86, 231

Sagan, C., & Chyba, C. 1997, Science, 276, 1217

Samson, J. A. R., Haddad, G. N., & Kilcoyne, L. D. 1987, JChPh, 87, 6416

Sander, S. P., Friedl, R. R., Abbatt, J. P. D., et al. 2011, Chemical Kinetics and Photochemical Data for Use in Atmospheric Studies Evaluation Number 17 (JPL Publication)

Sharp, C. M., & Burrows, A. 2007, ApJS, 168, 140

Showman, A. P., & Guillot, T. 2002, A&A, 385, 166

Sing, D. K., Wakeford, H. R., Showman, A. P., et al. 2015, MNRAS, 446, 2428

Sing, D. K., Fortney, J. J., Nikolov, N., et al. 2016, Nature, 529, 59

Smith, N. S., & Raulin, F. 1999, J. Geophys. Res., 104, 1873

Smith, P. L., Yoshino, K., Parkinson, W. H., Ito, K., & Stark, G. 1991, J. Geophys. Res., 96, 17

Smith, R. K., Brickhouse, N. S., Liedahl, D. A., & Raymond, J. C. 2001, ApJL, 556, L91

Smith, W. R., & Missen, R. W. 1982, Chemical Reaction Equilibrium Analysis: Theory and Algorithms (New York: A Wiley-Interscience Publication)

Stevenson, K. B. 2016, ApJL, 817, L16

Teske, J. K., Turner, J. D., Mueller, M., & Griffith, C. A. 2013, MNRAS, 431, 1669

Tomasko, M. G., Doose, L. R., Dafoe, L. E., & See, C. 2009, Icarus, 204, 271

Toon, O. B., McKay, C. P., Griffith, C. A., & Turco, R. P. 1992, Icarus, 95, 24

Toon, O. B., Turco, R. P., & Pollack, J. B. 1980, Icarus, 43, 260

Torres, G., Winn, J. N., & Holman, M. J. 2008, ApJ, 677, 1324

Trainer, M. G., Pavlov, A. A., Dewitt, H. L., et al. 2006, Proceedings of the National Academy of Science, 103, 18035

Tsai, S.-M., Lyons, J. R., Grosheintz, L., et al. 2017, ApJS, 228, 20

Venot, O., Agúndez, M., Selsis, F., Tessenyi, M., & Iro, N. 2014, A&A, 562, A51

Venot, O., Hébrard, E., Agúndez, M., Decin, L., & Bounaceur, R. 2015, A&A, 577, A33

Venot, O., Hébrard, E., Agúndez, M., et al. 2012, A&A, 546, A43

Visscher, C., & Moses, J. I. 2011, ApJ, 738, 72

Wilson, P. A., Colón, K. D., Sing, D. K., et al. 2014, MNRAS, 438, 2395

Woitke, P., & Helling, C. 2003, A&A, 399, 297

—. 2004, A&A, 414, 335

Wu, Y.-J., Lu, H.-C., Chen, H.-K., et al. 2007, JChPh, 127, 154311

Yoshino, K., Parkinson, W. H., Ito, K., & Matsui, T. 2005, Journal of Molecular Spectroscopy, 229, 238

Youngblood, A., France, K., Parke Loyd, R. O., et al. 2016, ApJ, 824, 101

Yung, Y. L., Allen, M., & Pinto, J. P. 1984, ApJS, 55, 465

Yung, Y. L., & Demore, W. B., eds. 1999, Photochemistry of planetary atmospheres

Zahnle, K., Marley, M. S., Morley, C. V., & Moses, J. I. 2016, ApJ, 824, 137

Zahnle, K. J., & Marley, M. S. 2014, ApJ, 797, 41

Appendix

A   Comparison with Tsai et al. (2017)

To verify our photochemical model presented in section 2.1, we first examine our thermochemical reaction networks. In this section, we attempt to reproduce the results of Tsai et al. (2017) for two hot Jupiters, HD 189733b and HD 209458b. They considered thermochemistry and eddy-diffusion transport, but ignored photochemistry. They then simulated the atmospheric chemistry of these two planets to compare their models with those of Moses et al. (2011).

For comparison, we adopt the same assumptions and values of input parameters that Tsai et al. (2017) adopted: The fluxes of all the species are zero both at the lower and upper boundaries. The temperature profiles are the dayside-averaged ones taken from the supplementary material of Moses et al. (2011). The value of eddy diffusion coefficient K_{zz} is 1×10^9 cm^2 s^{-1} and the solar elemental abundance ratios from Table 10 of Lodders et al. (2009). O abundance is multiplied by a factor of 0.793 to account for the effect of oxygen sequestration (see Moses et al., 2011). We prepare 90 layers with thickness of 50 km and 140 km for the simulations of HD 189733b and HD 209458b, respectively, and place the lower boundary pressure at 1000 bar. For the values of planet mass and 1000-bar radius, we use 1.15 M_J and 1.26 R_J for HD 189733b (Bouchy et al., 2005), and 0.685 M_J and 1.359 R_J for HD 209458b (Torres et al., 2008).

Figure A.1 shows the calculated vertical distributions of gaseous species (solid lines) for the atmospheres of HD 189733b, which are compared to the results of Tsai et al. (2017) (thin solid lines with crosses). HCN is not included in the model of Tsai et al. (2017), while the molecules indicated in italics are not included in our model. Vertical distributions of HCN from "no photon" models of Moses et al. (2011), in which they omit photochemistry, are also shown (thin solid lines with asterisks). We take these data by tracing their Figure 3 with the use of the software, PlotDigitizer X[1]. We also

---

[1]http://www.surf.nuqe.nagoya-u.ac.jp/ nakahara/software/plotdigitizerx/index-e.html

present the thermochemical equilibrium abundances with dashed lines for reference.
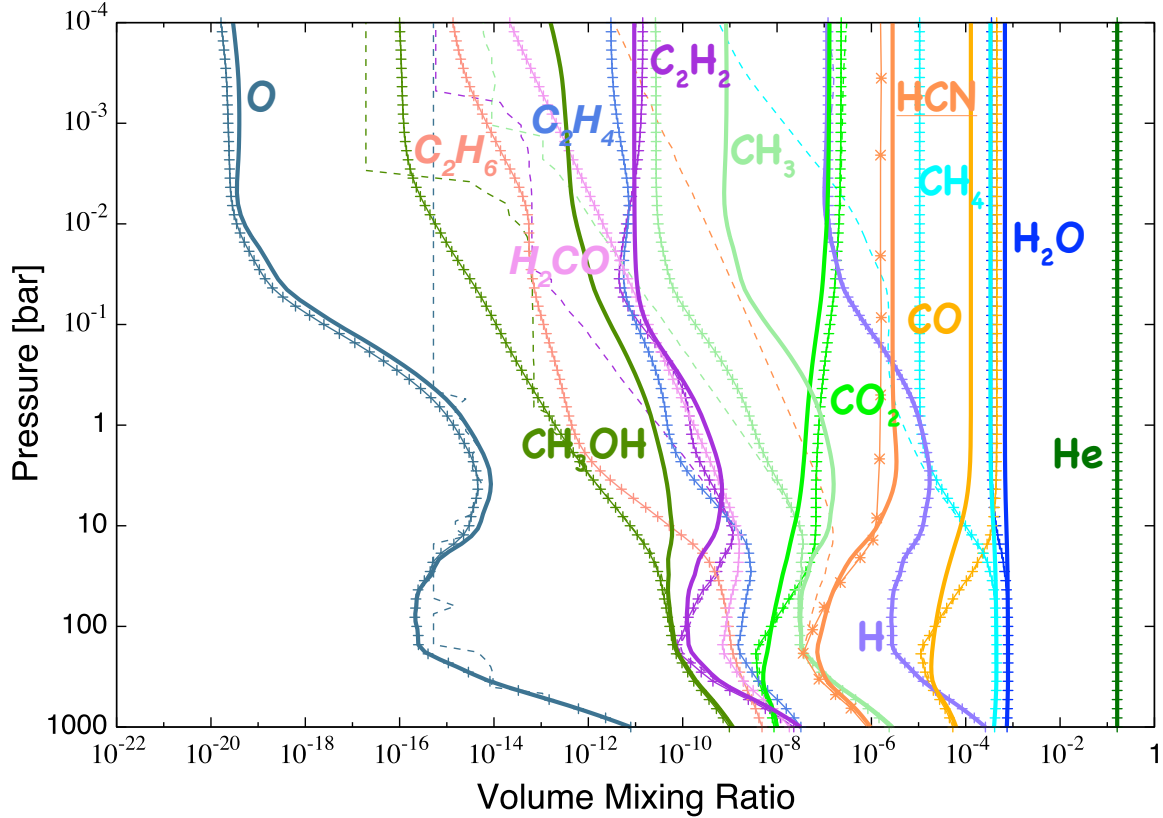
Figure A.1: Vertical distributions of gaseous species (solid lines) for the atmospheres of HD 189733b, compared to those from Tsai et al. (2017) (solid lines with crosses). HCN is not included in the model of Tsai et al. (2017) while the molecules indicated in italics are not included in our model. Vertical distributions of HCN from "no photon" models of Moses et al. (2011), in which they omit photochemistry, are also shown (thin solid lines with asterisks). We take these data by tracing their Figure 3 with the use of the software, PlotDigitizer X. We also present the thermochemical equilibrium abundances with dashed lines for reference. Note that the eddy diffusion transport is not included in the thermochemical equilibrium calculations.

The mixing ratios of ours and Tsai et al. (2017) differ by a factor of ~ 30 for CH_4, ~ 4 for CO, and ~ 2 for H_2O, because quench occurs at higher pressure in our model. Because of such difference in f_{CH_4}, our abundances of CH_3 and CH_3OH are larger by 1-2 and 1-3 orders of magnitude, respectively. The abundances of species in thermochemical equilibrium such as CO_2, H, and O match theirs well. As for haze precursors, since HCN is not considered in their models, we cannot do any comparison regarding HCN. However, the "no photon" models of Moses et al. (2011) (thin solid line with asterisks), in which they omit photochemistry, yield similar abundances to ours. The abundance

of C_2H_2 differs little between Tsai et al. (2017)'s and ours. This slight difference in C_2H_2 abundance never affects our results regarding haze distributions and transmission spectra, since the profile of the production rate of monomers is determined mainly by that of HCN abundance (see § 4.1 and 4.4).

Figure A.2 is same as Fig. A.1 but for the case of HD 209458b. In the case of HD 209458b, the abundances of the species, CO, H_2O, H, CH_4, CO_2, CH_3, CH_3OH, and O, match theirs well. This is because of higher temperature of HD 209458b, for which the molecules tend to be closer to thermochemical equilibrium. As for haze precursors, we again compare the HCN abundance from our model with that from the "no photon" models of Moses et al. (2011). In our model, the abundance of HCN deviates from its thermochemical equilibrium values at higher pressure ($\sim$ 100 bar) compared to Moses et al. (2011) ($\sim$ 1 bar), and HCN results in being quenched at larger abundance in the pressure range of 1×10^{-3} bar to 100 bar. If we used the result of Moses et al. (2011) as the distribution of the precursor molecules, we would assume smaller monomer production at high altitudes and larger at low altitudes. This would hamper particle growth a little and result in less flat transmission spectra. The abundance of C_2H_2 is larger than that of Tsai et al. (2017) in the region where C_2H_2 is not in thermochemical equilibrium (i.e., $P \lesssim 10^{-1}$ bar). However, again, this difference never affects our results regarding haze distributions and transmission spectra, because the profile of the production rate of monomers is determined mainly by that of HCN abundance.
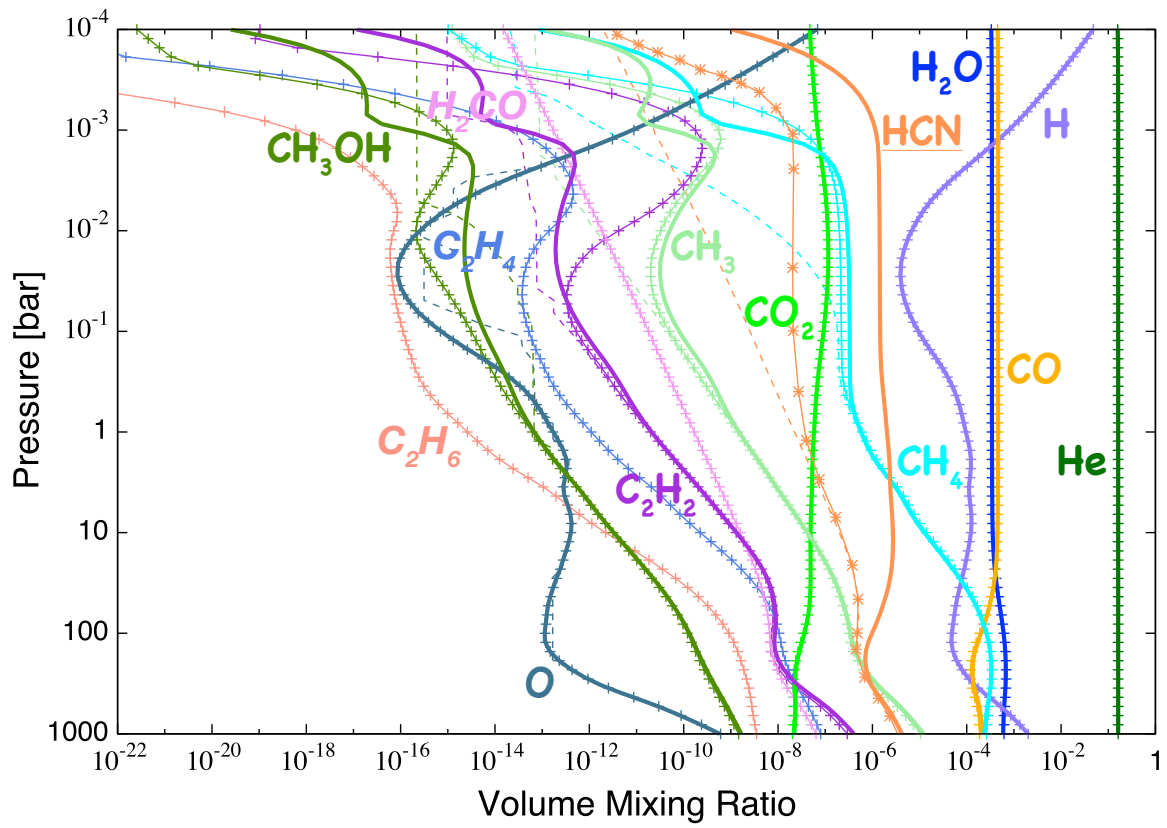
Figure A.2: Same as Fig. A.1 but for the case of HD 209458b.

B   Comparison with Kopparapu et al. (2012)

In this section, we compare our photochemical model with the model of Kopparapu et al. (2012) for the hot Jupiter WASP-12b, in which photochemistry is considered in addition to thermochemistry and transport by eddy diffusion.

For comparison, we use the same profiles of temperature and eddy diffusion coefficient by tracing the Figure 1 of Kopparapu et al. (2012) with use of PlotDigitizer X. Following them, we neglect transport of the short-lived species $O(^1D)$ and $^1CH_2$. Since the photodissociation reactions for CO, H_2, N_2, and CH_3OH are not taken into account in their model, we exclude photochemical reactions, P7, P10, P11, and P12, from our photochemical reaction list used in this section. Also, while we consider the following photochemical reaction,

$$P6 : CH_4 \rightarrow CH + H_2 + H,$$

which they do not consider, they consider the following photochemical reaction,

$$CH_4 \rightarrow CH_2 + H + H,$$

which we do not consider. The other photochemical reactions are identical to theirs. Following them, we use the G0V star spectrum from Pickles (1998) and convert it to suit for WASP-12 by using the relation between the flux at 5556 Å and the visual magnitude, V, from Gray (1992). We use $V = 11.69$ (Hebb et al., 2009), 427 pc as the distance to the star (Chan et al., 2011), and 0.0229 AU as the semi-major axis (Hebb et al., 2009). We take the solar elemental abundance ratios from Table 1 of Asplund et al. (2005) following them. For the simulation of the case for C/O = 1.08, we just double the C abundance keeping the other elemental abundances unchanged. We prepare 100 layers with thickness of 128 km placing the lower boundary pressure at 1 bar. For the values of planet mass and 1-bar radius, we use 1.41 M_J and 1.79 R_J, respectively (Hebb et al., 2009).

Figure B.3 shows the calculated vertical distributions of gaseous species (solid lines) for the case of C/O = 0.54, which are compared to the results of Kopparapu et al. (2012) (solid lines with symbols) that we also take by tracing their Figure 4 with the use of PlotDigitizer X. We also present the thermochemical equilibrium abundances with dashed lines for reference.

The abundances of the major ($f_i \gtrsim 10^{-10}$) species agree with Kopparapu et al. (2012)'s within one order of magnitude. The abundances at the lower boundary (1 bar) are slightly different from theirs, although we have used thermochemical equilibrium
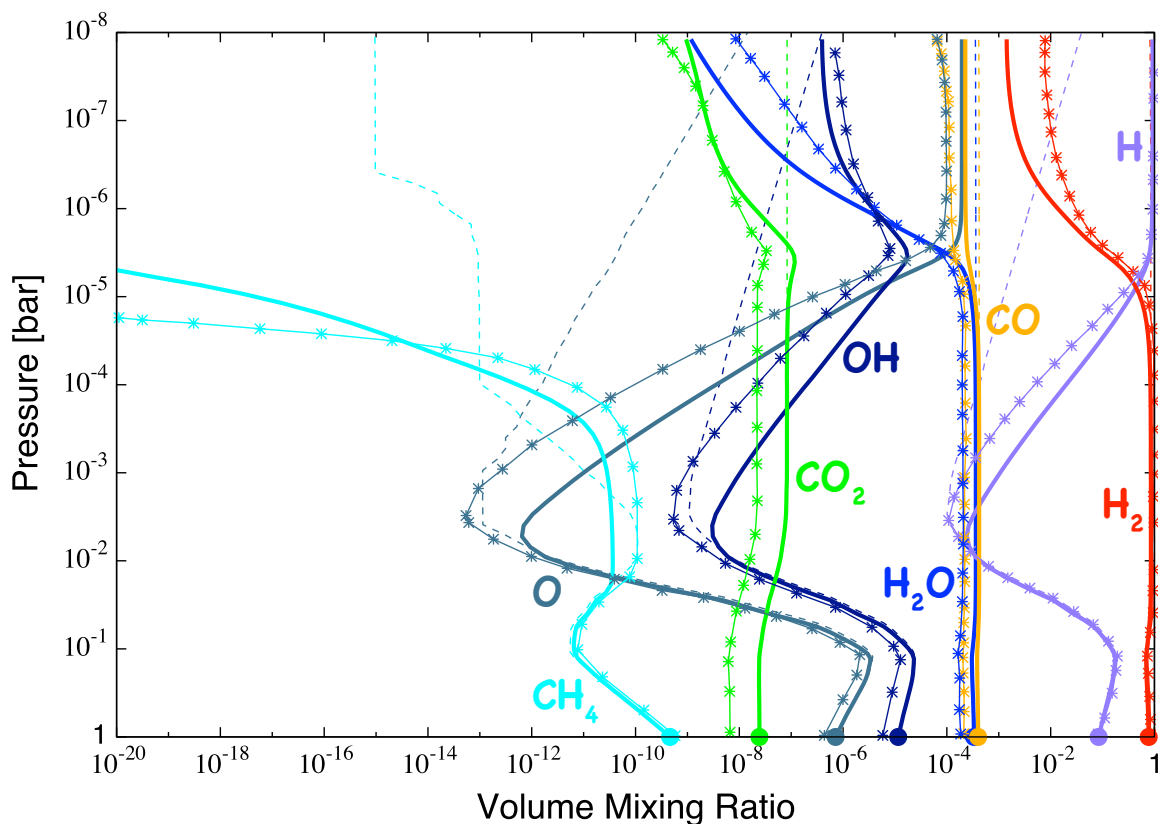
Figure B.3: Vertical distributions of gaseous species (solid lines) compared to those from Kopparapu et al. (2012) (solid lines with symbols) for the case of C/O = 0.54, which we take by tracing their Figure 4 with the use of PlotDigitizer X. Filled circles represent the thermochemical equilibrium values at the lower boundary. The thermochemical equilibrium abundances are shown with dashed lines for reference. Note that the eddy diffusion transport is not included in the thermochemical equilibrium calculations.

values for the lower boundary condition in the same way as they did and also used the same elemental abundance ratios. The differences in abundance profile may come from those in these lower boundary values.

Figure B.4 is same as Fig. B.3 but for the case of C/O = 1.08. The differences in abundance are larger compared to the case of C/O = 0.54, but the trends are similar. As for haze precursors, HCN and C_2H_2, both molecules are less photo-dissociated compared to their results. If we used the result of Kopparapu et al. (2012) as the distribution of the precursor molecules, we would assume smaller monomer production at high altitudes and larger at low altitudes. This would hamper particle growth a little and result in less flat transmission spectra.
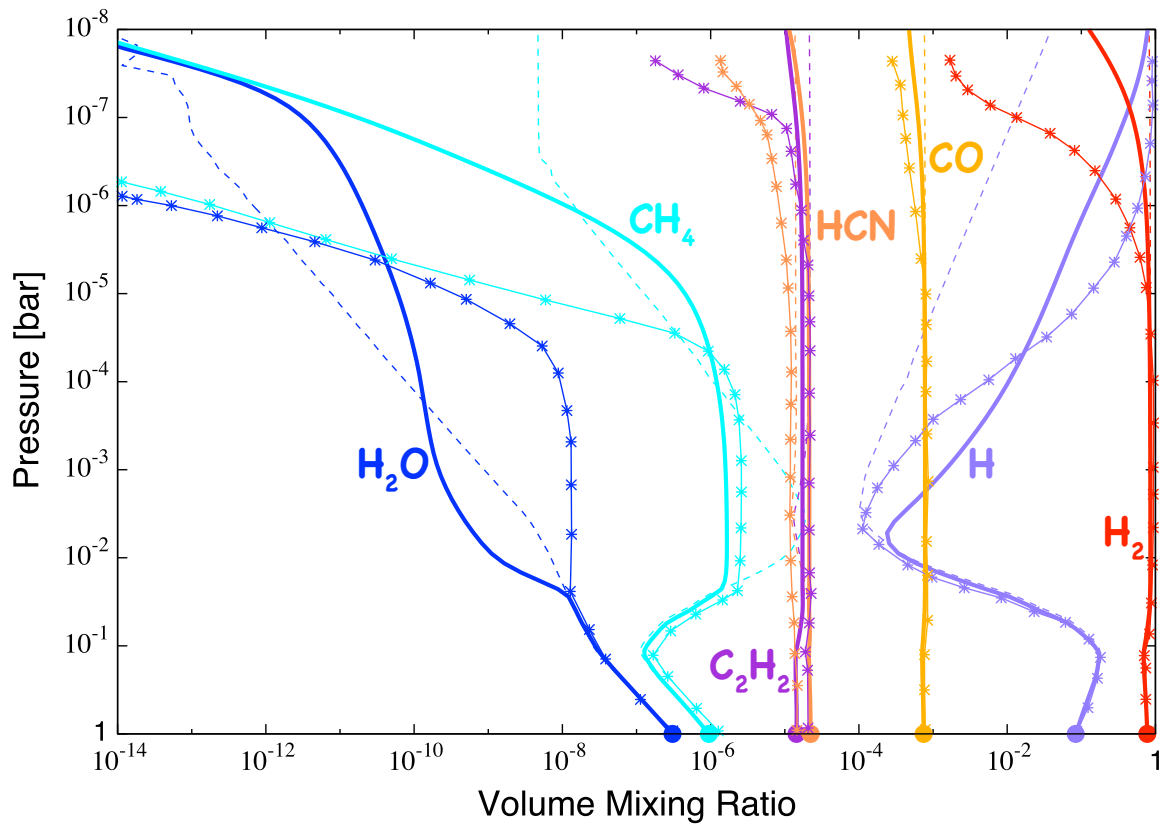
Figure B.4: Same as Fig. B.3 but for the case of C/O = 1.08.

C Thermochemical Reactions

Table C.1: Thermochemical Reactions

No.	No. Hu[a]	Reactants		Products	Rate Coefficients[b]	Ref.	Temp.[c]
R1	R1	$C + CH_2$	$\rightarrow$	$CH + CH$	$2.69 \times 10^{-12} e^{-23573.0/T}$	NIST	1000-4000
R2	R2	$C + CN$	$\rightarrow$	$C_2 + N$	$4.98 \times 10^{-10} e^{-18041.0/T}$	NIST	5000-8000
R3	R3	$C + H_2$	$\rightarrow$	$CH + H$	$6.64 \times 10^{-10} e^{-11700.0/T}$	NIST	1520-2540
R4	R5	$C + N_2$	$\rightarrow$	$CN + N$	$8.7 \times 10^{-11} e^{-22611.0/T}$	NIST	2000-5000
R5	R6	$C + O_2$	$\rightarrow$	$CO + O$	$5.1 \times 10^{-11} (T/298.0)^{-0.3}$	NIST	15-295
R6	R14	$C_2H + CH_3OH$	$\rightarrow$	$C_2H_2 + CH_3O$	2.0×10^{-12}	NIST	300-2500
R7	R17	$C_2H_2 + CN$	$\rightarrow$	$HCN + C_2H$	2.2×10^{-10}	NIST	294
R8	R31	$CH + CH$	$\rightarrow$	C_2H_2	2.0×10^{-10}	NIST	298
R9	R34	$CH_2 + C_2H$	$\rightarrow$	$C_2H_2 + CH$	3.0×10^{-11}	NIST	300-2500
R10	R40	$NH + OH$	$\rightarrow$	$NH_2 + O$	$2.94 \times 10^{-12} (T/298.0)^{0.1} e^{5800.0/T}$	NIST	298-3000
R11	R42	$CH_2 + CH_2$	$\rightarrow$	$C_2H_2 + H_2$	$2.62 \times 10^{-9} e^{-6010.0/T}$	NIST	1100-2700
R12	R43	$CH_2 + CH_2$	$\rightarrow$	$C_2H_2 + H + H$	$3.32 \times 10^{-10} e^{-5530.0/T}$	NIST	1100-2700
R13	R48	$CH_2 + CH_4$	$\rightarrow$	$CH_3 + CH_3$	$7.12 \times 10^{-12} e^{-5050.0/T}$	NIST	296-707
R14	R49	$CH_2 + CH_3OH$	$\rightarrow$	$CH_3 + CH_3O$	$1.12 \times 10^{-15} (T/298.0)^{3.1} e^{-3490.0/T}$	NIST	300-2500
R15	R50	$CH_2 + HCO$	$\rightarrow$	$CO + CH_3$	3.0×10^{-11}	NIST	300-2500
R16	R57	$CH_3 + C_2H_2$	$\rightarrow$	$CH_4 + C_2H$	$3.0 \times 10^{-13} e^{-8700.0/T}$	NIST	300-2500
R17	R69	$CH_3 + CH_3OH$	$\rightarrow$	$CH_4 + CH_3O$	$1.12 \times 10^{-15} (T/298.0)^{3.1} e^{-3490.0/T}$	NIST	300-2500
R18	R71	$CH_3 + HCO$	$\rightarrow$	$CH_4 + CO$	2.0×10^{-10}	NIST	300-2500
R19	R91	$CH_4 + C_2H$	$\rightarrow$	$C_2H_2 + CH_3$	$3.0 \times 10^{-12} e^{-250.0/T}$	NIST	300-2500
R20	R96	$CH_4 + CH_3O$	$\rightarrow$	$CH_3OH + CH_3$	$2.61 \times 10^{-13} e^{-4450.0/T}$	NIST	300-2500
R21	R99	$CH_4 + CN$	$\rightarrow$	$HCN + CH_3$	$5.11 \times 10^{-13} (T/298.0)^{2.64} e^{150.3/T}$	NIST	290-1500
R22	R101	$CH_3OH + CN$	$\rightarrow$	$HCN + CH_3O$	1.2×10^{-10}	NIST	294
R23	R108	$HCO + C_2H$	$\rightarrow$	$C_2H_2 + CO$	1.0×10^{-10}	NIST	300-2500
R24	R113	$HCO + CH_3O$	$\rightarrow$	$CH_3OH + CO$	1.5×10^{-10}	NIST	300-2500
R25	R116	$HCO + CN$	$\rightarrow$	$HCN + CO$	1.0×10^{-10}	NIST	500-2500
R26	R120	$CO + C_2H_2$	$\rightarrow$	$C_2H + HCO$	$8.0 \times 10^{-10} e^{-53641.4/T}$	NIST	300-2500
R27	R122	$CO + CH_3$	$\rightarrow$	$C_2H_2 + OH$	$6.3 \times 10^{-11} e^{-30428.9/T}$	NIST	1500-1900
R28	R127	$H + C_2H$	$\rightarrow$	C_2H_2	3.0×10^{-10}	NIST	300-2500
R29	R128	$H + C_2H$	$\rightarrow$	$H_2 + C_2$	$6.0 \times 10^{-11} e^{-14192.0/T}$	NIST	300-2500
R30	R129	$H + C_2H_2$	$\rightarrow$	$C_2H + H_2$	$1.0 \times 10^{-10} e^{-11200.0/T}$	NIST	300-2500
R31	R145	$H + CH$	$\rightarrow$	$C + H_2$	$1.31 \times 10^{-10} e^{-85.6/T}$	NIST	300-2000
R32	R146	$H + CH_2$	$\rightarrow$	$CH + H_2$	$1.0 \times 10^{-11} e^{900.0/T}$	NIST	300-3000
R33	R149	$H + CH_3$	$\rightarrow$	$CH_2 + H_2$	$1.0 \times 10^{-10} e^{-7600.0/T}$	NIST	300-2500
R34	R152	$H + CH_3O$	$\rightarrow$	CH_3OH	$2.89 \times 10^{-10} (T/298.0)^{0.04}$	NIST	300-2500
R35	R153	$H + CH_3O$	$\rightarrow$	$CH_3 + OH$	1.6×10^{-10}	NIST	300-2500
R36	R157	$H + CH_4$	$\rightarrow$	$CH_3 + H_2$	$5.83 \times 10^{-13} (T/298.0)^{3.0} e^{-4040.0/T}$	NIST	300-2500
R37	R158	$H + CH_3OH$	$\rightarrow$	$CH_3 + H_2O$	$3.32 \times 10^{-10} e^{-2670.0/T}$	NIST	1370-1840

Table C.1: Thermochemical Reactions

No.	No. Hu[a]	Reactants		Products	Rate Coefficients[b]	Ref.	Temp.[c]
R38	R159	$H + CH_3OH$	$\rightarrow$	$CH_3O + H_2$	$2.42 \times 10^{-12} \, (T/298.0)^{2.0} \, e^{-2270.0/T}$	NIST	300-2500
R39	R162	$H + HCO$	$\rightarrow$	$CO + H_2$	1.50×10^{-10}	NIST	300-2500
R40	R165	$H + CO_2$	$\rightarrow$	$CO + OH$	$2.51 \times 10^{-10} e^{-13350.0/T}$	NIST	300-2500
R41	R166	$H + H_2O$	$\rightarrow$	$H_2 + OH$	$6.82 \times 10^{-12} \, (T/298.0)^{1.6} \, e^{-9720.0/T}$	NIST	300-2500
R42	R184	$H + NH$	$\rightarrow$	$H_2 + N$	1.69×10^{-11}	NIST	1500-2500
R43	R185	$H + NH_2$	$\rightarrow$	$H_2 + NH$	$1.05 \times 10^{-10} e^{-4450.1/T}$	NIST	1100-1800
R44	R186	$H + NH_3$	$\rightarrow$	$H_2 + NH_2$	$7.80 \times 10^{-13} \, (T/298.0)^{2.4} \, e^{-4990.1/T}$	NIST	490-1780
R45	R191	$H + O_2$	$\rightarrow$	$O + OH$	$6.73 \times 10^{-10} \, (T/298.0)^{-0.59} \, e^{-8152.0/T}$	NIST	800-3500
R46	R193	$H_2 + C$	$\rightarrow$	$CH + H$	$6.64 \times 10^{-10} e^{-11700.0/T}$	NIST	1520-2540
R47	R194	$H_2 + C_2$	$\rightarrow$	$C_2H + H$	$1.1 \times 10^{-10} e^{-4000.0/T}$	NIST	2580-4650
R48	R195	$H_2 + C_2H$	$\rightarrow$	$C_2H_2 + H$	$8.95 \times 10^{-13} \, (T/298.0)^{2.57} \, e^{-130.0/T}$	NIST	200-2000
R49	R202	$H_2 + CH$	$\rightarrow$	$CH_2 + H$	$3.75 \times 10^{-10} e^{-1660.0/T}$	NIST	327-397
R50	R203	$H_2 + CH_3$	$\rightarrow$	$CH_4 + H$	$6.86 \times 10^{-14} \, (T/298.0)^{2.74} \, e^{-4740.0/T}$	NIST	300-2500
R51	R204	$H_2 + CH_3O$	$\rightarrow$	$CH_3OH + H$	$9.96 \times 10^{-14} \, (T/298.0)^{2} \, e^{-6720.0/T}$	NIST	300-2500
R52	R207	$H_2 + CN$	$\rightarrow$	$HCN + H$	$5.65 \times 10^{-13} \, (T/298.0)^{2.45} \, e^{-1131.0/T}$	NIST	300-2500
R53	R211	$H_2 + NH$	$\rightarrow$	$NH_2 + H$	$3.5 \times 10^{-11} e^{-7758.0/T}$	NIST	833-1432
R54	R212	$H_2 + NH_2$	$\rightarrow$	$NH_3 + H$	$6.75 \times 10^{-14} \, (T/298.0)^{2.6} \, e^{-3006.8/T}$	NIST	400-2200
R55	R214	$H_2O + C$	$\rightarrow$	$CH + OH$	$1.3 \times 10^{-12} e^{-19845.0/T}$	NIST	1000-4000
R56	R215	$H_2O + C_2H$	$\rightarrow$	$C_2H_2 + OH$	$7.74 \times 10^{-14} \, (T/298.0)^{3.05} \, e^{-376.0/T}$	NIST	300-2000
R57	R218	$H_2O + CH$	$\rightarrow$	CH_3O	$9.48 \times 10^{-12} e^{380.0/T}$	NIST	298-669
R58	R219	$H_2O + CN$	$\rightarrow$	$HCN + OH$	$1.3 \times 10^{-11} e^{-3760.0/T}$	NIST	500-2500
R59	R276	$N + C_2$	$\rightarrow$	$CN + C$	2.8×10^{-11}	NIST	298
R60	R280	$N + CH$	$\rightarrow$	$C + NH$	$3.0 \times 10^{-11} \, (T/298.0)^{0.65} \, e^{-1203.0/T}$	NIST	990-1010
R61	R281	$N + CH$	$\rightarrow$	$CN + H$	$1.66 \times 10^{-10} \, (T/298.0)^{-0.09}$	NIST	216-584
R62	R282	$N + CH_3$	$\rightarrow$	$H_2 + HCN$	$4.3 \times 10^{-10} e^{-420.0/T}$	NIST	200-423
R63	R284	$N + CN$	$\rightarrow$	$C + N_2$	3.0×10^{-10}	NIST	300-2500
R64	R287	$N + H_2O$	$\rightarrow$	$OH + NH$	$6.03 \times 10^{-11} \, (T/298.0)^{1.2} \, e^{-19243.6/T}$	NIST	800-3000
R65	R289	$N + NH$	$\rightarrow$	$N_2 + H$	$1.95 \times 10^{-11} \, (T/298.0)^{0.51} \, e^{-9.6/T}$	NIST	300-2500
R66	R290	$N + NH_2$	$\rightarrow$	$NH + NH$	$3.0 \times 10^{-13} e^{-7600.0/T}$	NIST	1000-4000
R67	R300	$NH + NH_3$	$\rightarrow$	$NH_2 + NH_2$	$5.25 \times 10^{-10} e^{-13470.0/T}$	NIST	1300-1700
R68	R305	$NH + O$	$\rightarrow$	$OH + N$	1.16×10^{-11}	NIST	250-3000
R69	R309	$NH + OH$	$\rightarrow$	$H_2O + N$	$3.1 \times 10^{-12} \, (T/298.0)^{1.2}$	NIST	298-3000
R70	R310	$NH_2 + C$	$\rightarrow$	$CH + NH$	$9.61 \times 10^{-13} e^{-10500.0/T}$	NIST	1000-4000
R71	R311	$NH_2 + C_2H_2$	$\rightarrow$	$C_2H + NH_3$	$8.2 \times 10^{-13} e^{-2780.0/T}$	NIST	340-510
R72	R316	$NH_2 + CH_3$	$\rightarrow$	$CH_4 + NH$	$8.4 \times 10^{-10} e^{-4834.9/T}$	NIST	300-2000
R73	R317	$NH_2 + CH_4$	$\rightarrow$	$CH_3 + NH_3$	$8.77 \times 10^{-15} \, (T/298.0)^{3} \, e^{-2130.0/T}$	NIST	300-2000
R74	R319	$NH_2 + H_2O$	$\rightarrow$	$OH + NH_3$	$2.1 \times 10^{-13} \, (T/298.0)^{1.9} \, e^{-5725.0/T}$	NIST	300-3000
R75	R323	$NH_2 + O$	$\rightarrow$	$OH + NH$	1.16×10^{-11}	NIST	298-3000
R76	R326	$NH_2 + OH$	$\rightarrow$	$H_2O + NH$	$7.69 \times 10^{-13} \, (T/298.0)^{1.5} \, e^{-230.0/T}$	NIST	250-3000

Table C.1: Thermochemical Reactions

No.	No. Hu[a]	Reactants		Products	Rate Coefficients[b]	Ref.	Temp.[c]
R77	R327	$NH_3 + CH$	$\rightarrow$	$HCN + H_2 + H$	$7.24 \times 10^{-11} e^{317.0/T}$	NIST	300-1300
R78	R328	$NH_3 + CH_3$	$\rightarrow$	$CH_4 + NH_2$	$9.55 \times 10^{-14} e^{-4895.0/T}$	NIST	350-600
R79	R329	$NH_3 + CN$	$\rightarrow$	$HCN + NH_2$	1.66×10^{-11}	NIST	300-700
R80	R388	$O + C_2$	$\rightarrow$	$CO + C$	6.0×10^{-10}	NIST	8000
R81	R389	$O + C_2H$	$\rightarrow$	$CO + CH$	1.7×10^{-11}	NIST	300-2500
R82	R391	$O + C_2H_2$	$\rightarrow$	$CO + CH_2$	$3.49 \times 10^{-12} (T/298.0)^{1.5} e^{-850.0/T}$	NIST	300-2500
R83	R407	$O + CH$	$\rightarrow$	$OH + C$	$2.52 \times 10^{-11} e^{-2380.0/T}$	NIST	10-6000
R84	R408	$O + CH$	$\rightarrow$	$CO + H$	6.6×10^{-11}	NIST	300-2000
R85	R409	$O + CH_2$	$\rightarrow$	$CH + OH$	7.2×10^{-12}	NIST	300-2500
R86	R410	$O + CH_2$	$\rightarrow$	$HCO + H$	5.0×10^{-11}	NIST	1200-1800
R87	R411	$O + CH_2$	$\rightarrow$	$CO + H + H$	1.2×10^{-10}	NIST	300-2500
R88	R412	$O + CH_2$	$\rightarrow$	$CO + H_2$	7.3×10^{-11}	NIST	300-2500
R89	R414	$O + CH_3$	$\rightarrow$	CH_3O	$7.51 \times 10^{-14} (T/298.0)^{-2.12} e^{-314.0/T}$	NIST	300-2500
R90	R416	$O + CH_3$	$\rightarrow$	$CO + H_2 + H$	5.72×10^{-11}	NIST	290-900
R91	R420	$O + CH_3O$	$\rightarrow$	$CH_3 + O_2$	2.5×10^{-11}	NIST	298
R92	R423	$O + CH_4$	$\rightarrow$	$CH_3 + OH$	$2.26 \times 10^{-12} (T/298.0)^{2.2} e^{-3820.0/T}$	NIST	420-1520
R93	R424	$O + CH_3OH$	$\rightarrow$	$CH_3O + OH$	$1.66 \times 10^{-11} e^{-2360.0/T}$	NIST	300-1000
R94	R426	$O + HCO$	$\rightarrow$	$CO + OH$	5.0×10^{-11}	NIST	300-2500
R95	R427	$O + HCO$	$\rightarrow$	$CO_2 + H$	5.0×10^{-11}	NIST	300-2500
R96	R430	$O + CN$	$\rightarrow$	$CO + N$	$3.4 \times 10^{-11} e^{-210.0/T}$	NIST	500-2500
R97	R433	$O + H_2$	$\rightarrow$	$H + OH$	$3.44 \times 10^{-13} (T/298.0)^{2.67} e^{-3160.0/T}$	NIST	300-2500
R98	R436	$O + HCN$	$\rightarrow$	$CO + NH$	$3.0 \times 10^{-12} e^{-4000.0/T}$	JPL	470-900
R99	R445	$O + OH$	$\rightarrow$	$O_2 + H$	$2.2 \times 10^{-11} e^{120.0/T}$	JPL	200-300
R100	R449	$O(^1D) + CH_4$	$\rightarrow$	$CH_3O + H$	3.5×10^{-11}	JPL	200-300
R101	R450	$O(^1D) + CH_4$	$\rightarrow$	$CH_3 + OH$	1.31×10^{-10}	JPL	200-300
R102	R453	$O(^1D) + CH_3OH$	$\rightarrow$	$CH_3O + OH$	4.2×10^{-10}	NIST	300
R103	R454	$O(^1D) + CO_2$	$\rightarrow$	$CO_2 + O$	$7.5 \times 10^{-11} e^{115.0/T}$	JPL	200-300
R104	R455	$O(^1D) + H_2$	$\rightarrow$	$H + OH$	1.2×10^{-10}	JPL	200-300
R105	R456	$O(^1D) + H_2O$	$\rightarrow$	$OH + OH$	$1.63 \times 10^{-10} e^{60.0/T}$	JPL	200-300
R106	R458	$O(^1D) + N_2$	$\rightarrow$	$O + N_2$	$2.15 \times 10^{-11} e^{110.0/T}$	JPL	200-300
R107	R461	$O(^1D) + NH_3$	$\rightarrow$	$OH + NH_2$	2.5×10^{-10}	JPL	200-300
R108	R464	$O(^1D) + O_2$	$\rightarrow$	$O + O_2$	$3.3 \times 10^{-11} e^{55.0/T}$	JPL	200-300
R109	R476	$OH + C_2$	$\rightarrow$	$CO + CH$	8.3×10^{-12}	NIST	2200
R110	R477	$OH + C_2H$	$\rightarrow$	$CO + CH_2$	3.0×10^{-11}	NIST	300-2500
R111	R478	$OH + C_2H$	$\rightarrow$	$C_2H_2 + O$	3.0×10^{-11}	NIST	300-2500
R112	R480	$OH + C_2H_2$	$\rightarrow$	$C_2H + H_2O$	$1.03 \times 10^{-13} (T/298.0)^{2.68} e^{-6060.0/T}$	NIST	300-2500
R113	R482	$OH + C_2H_2$	$\rightarrow$	$CO + CH_3$	$6.34 \times 10^{-18} (T/298.0)^{4.0} e^{1010.0/T}$	NIST	500-2500
R114	R495	$OH + CH_3$	$\rightarrow$	$CH_3O + H$	$6.45 \times 10^{-13} (T/298.0)^{1} e^{-6012.0/T}$	NIST	300-3000
R115	R496	$OH + CH_3$	$\rightarrow$	$CH_2 + H_2O$	$1.2 \times 10^{-10} e^{-1400.0/T}$	NIST	300-1000

Table C.1: Thermochemical Reactions

No.	No. Hu[a]	Reactants		Products	Rate Coefficients[b]	Ref.	Temp.[c]
R116	R501	$OH + CH_4$	$\rightarrow$	$CH_3 + H_2O$	$2.45 \times 10^{-12} e^{-1775.0/T}$	JPL	200-300
R117	R502	$OH + CH_3OH$	$\rightarrow$	$CH_3O + H_2O$	$2.9 \times 10^{-12} e^{-345.0/T}$	JPL	200-300
R118	R504	$OH + HCO$	$\rightarrow$	$CO + H_2O$	1.69×10^{-10}	NIST	300-2500
R119	R507	$OH + CN$	$\rightarrow$	$O + HCN$	$1.0 \times 10^{-11} e^{-1000.0/T}$	NIST	500-2500
R120	R511	$OH + CO$	$\rightarrow$	$CO_2 + H$	$5.4 \times 10^{-14} (T/298.0)^{1.5} e^{250.0/T}$	NIST	300-2000
R121	R512	$OH + H_2$	$\rightarrow$	$H_2O + H$	$2.8 \times 10^{-12} e^{-1800.0/T}$	JPL	200-300
R122	R515	$OH + HCN$	$\rightarrow$	$CO + NH_2$	$1.1 \times 10^{-13} e^{-5890.0/T}$	NIST	500-2500
R123	R516	$OH + HCN$	$\rightarrow$	$CN + H_2O$	$1.84 \times 10^{-13} (T/298.0)^{1.5} e^{-3890.0/T}$	NIST	298-2840
R124	R523	$OH + NH_3$	$\rightarrow$	$H_2O + NH_2$	$1.7 \times 10^{-12} e^{-710.0/T}$	JPL	200-300
R125	R526	$OH + OH$	$\rightarrow$	$H_2O + O$	1.8×10^{-12}	JPL	200-300
R126	R596	$^1CH_2 + H_2$	$\rightarrow$	$CH_2 + H_2$	1.26×10^{-11}	YD99[d]	
R127	R597	$^1CH_2 + H_2$	$\rightarrow$	$CH_3 + H$	9.24×10^{-11}	YD99[d]	
R128	R598	$^1CH_2 + CH_4$	$\rightarrow$	$CH_2 + CH_4$	1.2×10^{-11}	YD99[d]	
R129	R599	$^1CH_2 + CH_4$	$\rightarrow$	$CH_3 + CH_3$	5.9×10^{-11}	YD99[d]	
R130	R608	$C_2 + CH_4$	$\rightarrow$	$C_2H + CH_3$	$5.05 \times 10^{-11} e^{-297.0/T}$	YD99[d]	
R131	R644	$NH_2 + OH$	$\rightarrow$	$NH_3 + O$	$3.32 \times 10^{-13} (T/298.0)^{0.4} e^{-250.2/T}$	NIST	250-3000
R132	M1	$C + C$	$\rightarrow$	C_2	$5.46 \times 10^{-31} (T/298.0)^{-1.6} \times M$	NIST	5000-6000
R133	M2	$C + H_2$	$\rightarrow$	CH_2	$6.89 \times 10^{-32} \times M$	NIST	300
R134	M11	$H + CN$	$\rightarrow$	HCN	$9.35 \times 10^{-30} (T/298.0)^{-2.0} e^{-521.0/T} \times M$	NIST	500-2500
R135	M12	$H + CO$	$\rightarrow$	HCO	$5.29 \times 10^{-34} e^{-370.0/T} \times M$	NIST	300-2500
R136	M13	$H + H$	$\rightarrow$	H_2	$6.04 \times 10^{-33} (T/298.0)^{-1.0} \times M$	NIST	300-2500
R137	M14	$H + NH_2$	$\rightarrow$	NH_3	$3.0 \times 10^{-30} \times M$	NIST	298
R138	M16	$H + O$	$\rightarrow$	OH	$4.36 \times 10^{-32} (T/298.0)^{-1.0} \times M$	NIST	300-2500
R139	M18	$H + OH$	$\rightarrow$	H_2O	$6.87 \times 10^{-31} (T/298.0)^{-2.0} \times M$	NIST	300-3000
R140	M22	$N + C$	$\rightarrow$	CN	$9.4 \times 10^{-33} \times M$	NIST	298
R141	M23	$N + H$	$\rightarrow$	NH	$5.0 \times 10^{-32} \times M$	NIST	298
R142	M24	$N + H_2$	$\rightarrow$	NH_2	$1.0 \times 10^{-36} \times M$	NIST	298
R143	M25	$N + N$	$\rightarrow$	N_2	$1.38 \times 10^{-33} e^{502.7/T} \times M$	JPL	90-6400
R144	M30	$O + C$	$\rightarrow$	CO	$2.0 \times 10^{-34} \times M$	NIST	8000
R145	M31	$O + CO$	$\rightarrow$	CO_2	$1.7 \times 10^{-33} e^{-1509.0/T} \times M$	NIST	300-2500
R146	M34	$O + O$	$\rightarrow$	O_2	$5.21 \times 10^{-35} e^{900.0/T} \times M$	NIST	200-4000
R147	M55	$H + CH_2$	$\rightarrow$	CH_3	$k_0{}^e = 5.8 \times 10^{-30} e^{355.0/T}$ $k_\infty{}^e = 2.37 \times 10^{-12} e^{523.0/T}$	YD99[d]	
R148	M56	$H + CH_3$	$\rightarrow$	CH_4	$6.2 \times 10^{-29} (T/298.0)^{-1.8} \times M$	NIST	300-1000
R149	M72	$CH + H_2$	$\rightarrow$	CH_3	$k_0{}^e = 5.8 \times 10^{-30} e^{355.0/T e}$ $k_\infty{}^e = 2.37 \times 10^{-12} e^{523.0/T}$	YD99[d]	
R150	T19	CH_3OH	$\rightarrow$	$CH_3O + H$	$2.16 \times 10^{-8} e^{-33556.0/T} \times M$	NIST	1400-2500
R151	T20	CH_3OH	$\rightarrow$	$CH_3 + OH$	$1.1 \times 10^{-7} e^{-33075.0/T} \times M$	NIST	1000-2000
R152	T22	CH_3OH	$\rightarrow$	$CH_2 + H_2O$	$9.51 \times 10^{15} (T/298.0)^{-1.02} e^{-46185.0/T}$	NIST	1000-3000

Table C.1: Thermochemical Reactions

No.	No. Hu[a]	Reactants		Products	Rate Coefficients[b]	Ref.	Temp.[c]
R153	T46	HCO	$\rightarrow$	CO + H	$6.0 \times 10^{-11} e^{-7721.0/T} \times M$	NIST	298-1229
R154	T57	HCN	$\rightarrow$	H + CN	$1.93 \times 10^{-4} (T/298.0)^{-2.44} e^{-62782.1/T} \times M$	NIST	1800-5000

Thermochemical Reactions used in our photochemical model. M refers to the number density of background atmosphere (unit of cm^{-3}). I assume M equals to the total number density.

---

[a] Reaction number of Hu et al. (2012)

[b] Unit of $cm^3 s^{-1}$ for 2-body reactions and $cm^6 s^{-2}$ for 3-body reactions

[c] Unit of K

[d] Yung & Demore (1999)

[e] Rate coefficient k: $k = \left(\frac{k_0 M}{1 + \frac{k_0 M}{k_\infty}} \right) 0.6^{\left[1 + \left(\log_{10} \frac{k_0 M}{k_\infty} \right)^2 \right]^{-1}}$

D Photochemical Reactions

Table D.2: Photochemical Reactions

No.	No. Hu[a]	Reactants		Products	Quantum Yields
P1	1	O_2	$\rightarrow$	$O + O$	$\lambda < 139$ nm: 0.5
					139 nm $\leq \lambda < 175$ nm: 0
					$\lambda \geq 175$ nm: 1.0
P2	2	O_2	$\rightarrow$	$O + O(^1D)$	$\lambda < 139$ nm: 0.5
					139 nm $\leq \lambda < 175$ nm: 1.0
					$\lambda \geq 175$ nm: 0
P3	6	H_2O	$\rightarrow$	$H + OH$	1.0
P4	32	CH_4	$\rightarrow$	$CH_3 + H$	0.41 (Smith & Raulin, 1999)
P5	33	CH_4	$\rightarrow$	$CH_2^1 + H_2$	0.53 (Smith & Raulin, 1999)
P6	34	CH_4	$\rightarrow$	$CH + H_2 + H$	0.06 (Smith & Raulin, 1999)
P7	35	CO	$\rightarrow$	$C + O$	$\lambda < 111$ nm: 1.0
					$\lambda \geq 111$ nm: 0
P8	36	CO_2	$\rightarrow$	$CO + O$	$\lambda < 167$ nm: 0
					167 nm $\leq \lambda < 205$ nm: 1.0
					$\lambda \geq 205$ nm: 0
P9	37	CO_2	$\rightarrow$	$CO + O(^1D)$	$\lambda < 167$ nm: 1.0
					$\lambda \geq 167$ nm: 0
P10	38	H_2	$\rightarrow$	$H + H$	$\lambda < 80$ nm: 0.1 (Mentall & Gentieu, 1970)
					80 nm $\leq \lambda < 85$ nm: 1.0
					$\lambda \geq 85$ nm: 0
P11	39	N_2	$\rightarrow$	$N + N$	1.0
P12	40	CH_3OH	$\rightarrow$	$CH_3O + H$	1.0
P13	41	HCN	$\rightarrow$	$H + CN$	1.0
P14	42	NH_3	$\rightarrow$	$NH_2 + H$	$\lambda < 106$ nm: 0.3 (Lilly et al., 1973)
					106 nm $\leq \lambda < 165$ nm: Linear interpolation
					$\lambda \geq 165$ nm: 1.0
P15	43	NH_3	$\rightarrow$	$NH + H_2$	$\lambda < 106$ nm: 0.7
					106 nm $\leq \lambda < 165$ nm: Linear interpolation
					$\lambda \geq 165$ nm: 1.0
P16	55	C_2H_2	$\rightarrow$	$C_2H + H$	$\lambda < 217$ nm: 1.0 (Läuter et al., 2002)

Table D.2: Photochemical Reactions

No.	No. Hu[a]	Reactants	Products	Quantum Yields
				$\lambda \geq 217$ nm: 0

Photochemical Reactions used in our photochemical model and values of quantum yields.

---

[a]Reaction number of Hu et al. (2012)

E   UV Cross Sections

Table E.3: UV Cross Sections

Species	Wavelength	Cross Sections	T[a]
O_2	4.13 nm $\leq \lambda \leq$ 103.00 nm	Brion et al. (1979)	N
	108.75 nm $\leq \lambda \leq$ 129.60 nm	Ogawa & Ogawa (1975)	N
	129.62 nm $\leq \lambda \leq$ 172.53 nm	Yoshino et al. (2005)	N
	176.8 nm $\leq \lambda \leq$ 202.6 nm	Kockarts (1976)	N
	205 nm $\leq \lambda \leq$ 245 nm	Sander et al. (2011)	N
H_2O	6.20 nm $\leq \lambda \leq$ 118.08 nm	Chan et al. (1993a)	N
	121.00 nm $\leq \lambda \leq$ 198.00 nm	Sander et al. (2011)	N
	198.00 nm $\leq \lambda \leq$ 240 nm	Extrapolation	
CH_4	52.054 nm $\leq \lambda \leq$ 124.629 nm	Kameta et al. (2002)	N
	125 nm $\leq \lambda \leq$ 141 nm	Chen & Wu (2004)	N
	142 nm $\leq \lambda \leq$ 152 nm	Lee et al. (2001)	N
CO	6.199 nm $\leq \lambda \leq$ 177 nm	Chan et al. (1993b)	N
CO_2	35.0000 nm $\leq \lambda \leq$ 197.6950 nm	Huestis & Berkowitz (2010)	N
	197.70 nm $\leq \lambda \leq$ 270.15 nm	Ityaksov et al. (2008)	N
H_2	18 nm $\leq \lambda \leq$ 70 nm	Lee et al. (1976)	N
	77.00 nm $\leq \lambda \leq$ 86.88 nm	Cook & Metzger (1964)	N
	88.6 nm $\leq \lambda \leq$ 124 nm	Backx et al. (1976)	N
N_2	6.199 nm $\leq \lambda \leq$ 113 nm	Chan et al. (1993c)	N
CH_3OH	15.5 nm $\leq \lambda \leq$ 103 nm	Burton et al. (1992)	N
	106.50 nm $\leq \lambda \leq$ 165.00 nm	Nee et al. (1985)	N
	165.5 nm $\leq \lambda \leq$ 219.5 nm	Cheng et al. (2002)	N
HCN	133.42 nm $\leq \lambda \leq$ 144.75 nm	Macpherson & Simons (1978)	N
NH_3	8.0 nm $\leq \lambda \leq$ 105.0 nm	Samson et al. (1987)	N
	106.00 nm $\leq \lambda \leq$ 139.98 nm	Wu et al. (2007)	N
	140.00 nm $\leq \lambda \leq$ 230.00 nm	Cheng et al. (2006)	N
C_2H_2	6.20 nm $\leq \lambda \leq$ 131 nm	Cooper et al. (1995)	N
	136.90378 nm $\leq \lambda \leq$ 185.62863 nm	Smith et al. (1991)	Y
	185.63 nm $\leq \lambda \leq$ 236.290 nm	Bénilan et al. (2000)	Y

---

[a]Temperature dependence: Y and N indicate whether temperature dependence is taken into account or not.

F Observed Data of GJ 1214b, GJ 3470b, and GJ 436b

Table F.4: Observed transit depths of GJ 1214b

Reference	Telescope/Instrument	Filter/grism	Wavelength [μm]	R_p/R_s	Filter No.
Désert et al. (2011)	Warm-Spitzer/IRAC	3.6 um		$0.1176^{+0.0008}_{-0.0009}$	77
	Warm-Spitzer/IRAC	4.5 um		$0.1163^{+0.0010}_{-0.0008}$	78
Carter et al. (2011)	1.2 m telescope/Keplercam	Sloan Z'		0.01332 ± 0.00057	82
	1.2 m telescope/Keplercam	Sloan Z'		0.01388 ± 0.00059	82
	6.5 m Magellan (Baade) telescope/MagIC and IMACS	Sloan r'		0.01355 ± 0.00059	9
	1.2 m telescope/Keplercam	Sloan Z'		0.01333 ± 0.00063	82
	1.2 m telescope/Keplercam	Sloan Z'		0.01384 ± 0.00059	82
	1.2 m telescope/Keplercam	Sloan Z'		0.01281 ± 0.00081	82
	1.2 m telescope/Keplercam	Sloan Z'		0.01345 ± 0.00067	82
	1.2 m telescope/Keplercam	Sloan Z'		0.01416 ± 0.00066	82
	6.5 m Magellan (Baade) telescope/MagIC and IMACS	Sloan r'		0.01380 ± 0.00061	9
	1.2 m telescope/Keplercam	Sloan Z'		0.01303 ± 0.00062	82
	1.2 m telescope/Keplercam	Sloan Z'		0.01271 ± 0.00055	82
	1.2 m telescope/Keplercam	Sloan Z'		0.01377 ± 0.00058	82
	1.2 m telescope/Keplercam	Sloan Z'		0.01313 ± 0.00059	82
	1.2 m telescope/Keplercam	Sloan Z'		0.01299 ± 0.00053	82
	1.2 m telescope/Keplercam	Sloan Z'		0.01299 ± 0.00053	82
	1.2 m telescope/Keplercam	Sloan Z'		0.01376 ± 0.00060	82
	6.5 m Magellan (Baade) telescope/MagIC and IMACS	Sloan r'		0.01414 ± 0.00061	9
Croll et al. (2011)	CFHT/WIRCam	J		$0.01334^{+0.00020}_{-0.00021}$	36
	CFHT/WIRCam	Ks		$0.01459^{+0.00030}_{-0.00029}$	37
	CFHT/WIRCam	J		$0.01302^{+0.00044}_{-0.00040}$	36
	CFHT/WIRCam	CH4ON		$0.01290^{+0.00050}_{-0.00043}$	38
	CFHT/WIRCam	J		$0.01368^{+0.00026}_{-0.00021}$	36
	CFHT/WIRCam	Ks		$0.01422^{+0.00032}_{-0.00034}$	37
	CFHT/WIRCam	J		$0.01307^{+0.00034}_{-0.00031}$	36
	CFHT/WIRCam	Ks		$0.01424^{+0.00044}_{-0.00031}$	37
Bean et al. (2011)	Magellan/MMIRS	J		0.1158 ± 0.0024	70
	Magellan/MMIRS	H		0.1146 ± 0.0014	71
	Magellan/MMIRS	K(Channel 1)	1.98-2.08	0.1156 ± 0.0007	72
	Magellan/MMIRS	K(Channel 2)	2.08-2.18	0.1163 ± 0.0007	72
	Magellan/MMIRS	K(Channel 3)	2.18-2.28	0.1158 ± 0.0006	72
	Magellan/MMIRS	K(Channel 4)	2.28-2.38	0.1163 ± 0.0011	72
	VLT/FORS	GG435/600RI	0.610-0.630	0.1173 ± 0.0018	73
	VLT/FORS	GG435/600RI	0.630-0.650	0.1195 ± 0.0012	73
	VLT/FORS	GG435/600RI	0.650-0.670	0.1167 ± 0.0011	73
	VLT/FORS	GG435/600RI	0.670-0.690	0.1194 ± 0.0011	73
	VLT/FORS	GG435/600RI	0.690-0.710	0.1169 ± 0.0009	73
	VLT/FORS	GG435/600RI	0.710-0.730	0.1164 ± 0.0009	73
	VLT/FORS	GG435/600RI	0.730-0.750	0.1182 ± 0.0007	73
	VLT/FORS	GG435/600RI	0.750-0.770	0.1187 ± 0.0008	73
	VLT/FORS	GG435/600RI	0.770-0.790	0.1172 ± 0.0008	73
	VLT/FORS	GG435/600RI	0.790-0.810	0.1172 ± 0.0007	73
	VLT/FORS	GG435/600RI	0.810-0.830	0.1183 ± 0.0006	73
	VLT/FORS	GG435/600RI	0.830-0.850	0.1168 ± 0.0007	73
	VLT/FORS2	OG590/600z	0.780-0.790	0.1167 ± 0.0009 [a]	75
	VLT/FORS3	OG590/600z	0.790-0.800	0.1160 ± 0.0007	75
	VLT/FORS4	OG590/600z	0.800-0.810	0.1156 ± 0.0007	75

Table F.4: Observed transit depths of GJ 1214b

Reference	Telescope/Instrument	Filter/grism	Wavelength [μm]	R_p/R_s	Filter No.
	VLT/FORS5	OG590/600z	0.810-0.820	0.1176 ± 0.0008	75
	VLT/FORS6	OG590/600z	0.820-0.830	0.1176 ± 0.0007	75
	VLT/FORS7	OG590/600z	0.830-0.840	0.1162 ± 0.0007	75
	VLT/FORS8	OG590/600z	0.840-0.850	0.1172 ± 0.0007	75
	VLT/FORS9	OG590/600z	0.850-0.860	0.1151 ± 0.0008	75
	VLT/FORS10	OG590/600z	0.860-0.870	0.1168 ± 0.0007	75
	VLT/FORS11	OG590/600z	0.870-0.880	0.1171 ± 0.0007	75
	VLT/FORS12	OG590/600z	0.880-0.890	0.1171 ± 0.0007	75
	VLT/FORS13	OG590/600z	0.890-0.900	0.1159 ± 0.0007	75
	VLT/FORS14	OG590/600z	0.900-0.910	0.1167 ± 0.0006	75
	VLT/FORS15	OG590/600z	0.910-0.920	0.1175 ± 0.0007	75
	VLT/FORS16	OG590/600z	0.920-0.930	0.1178 ± 0.0006	75
	VLT/FORS17	OG590/600z	0.930-0.940	0.1165 ± 0.0009	75
	VLT/FORS18	OG590/600z	0.940-0.950	0.1168 ± 0.0008	75
	VLT/FORS19	OG590/600z	0.950-0.960	0.1176 ± 0.0009	75
	VLT/FORS20	OG590/600z	0.960-0.970	0.1172 ± 0.0009	75
	VLT/FORS21	OG590/600z	0.970-0.980	0.1161 ± 0.0010	75
	VLT/FORS22	OG590/600z	0.980-0.990	0.1165 ± 0.0011	75
	VLT/FORS23	OG590/600z	0.990-1.000	0.1168 ± 0.0011	75
	VLT/HAWKI	NB2090		0.1179 ± 0.0012	76
de Mooij et al. (2012)	MPI/ESO/GROND	g		$0.1198^{+0.0026}_{-0.0013}$	8
	MPI/ESO/GROND	r		0.1168 ± 0.0010	9
	INT/WFC	r		0.1143 ± 0.0018	31
	MPI/ESO/GROND	i		0.1162 ± 0.0013	10
	INT/WFC	I		0.1162 ± 0.0005	32
	MPI/ESO/GROND	z		0.1165 ± 0.0013	11
	NOT/NOTCam	Ks		0.1189 ± 0.0015	33
	WHT/LIRIS	Kc		0.1162 ± 0.0030	34
Berta et al. (2012)	HST/WFC3	G141	1.1115-1.1345	0.11641 ± 0.00102	22
	HST/WFC3	G141	1.1345-1.1575	0.11707 ± 0.00099	22
	HST/WFC3	G141	1.1575-1.1805	0.11526 ± 0.00098	22
	HST/WFC3	G141	1.1805-1.2035	0.11589 ± 0.00093	22
	HST/WFC3	G141	1.2035-1.2270	0.11537 ± 0.00091	22
	HST/WFC3	G141	1.2270-1.2505	0.11574 ± 0.00090	22
	HST/WFC3	G141	1.2505-1.2735	0.11662 ± 0.00088	22
	HST/WFC3	G141	1.2735-1.2965	0.11565 ± 0.00088	22
	HST/WFC3	G141	1.2965-1.3195	0.11674 ± 0.00085	22
	HST/WFC3	G141	1.3195-1.3430	0.11595 ± 0.00087	22
	HST/WFC3	G141	1.3430-1.3665	0.11705 ± 0.00089	22
	HST/WFC3	G141	1.3665-1.3895	0.11664 ± 0.00088	22
	HST/WFC3	G141	1.3895-1.4130	0.11778 ± 0.00088	22
	HST/WFC3	G141	1.4130-1.4365	0.11693 ± 0.00091	22
	HST/WFC3	G141	1.4365-1.4595	0.11772 ± 0.00090	22
	HST/WFC3	G141	1.4595-1.4835	0.11663 ± 0.00092	22
	HST/WFC3	G141	1.4835-1.5065	0.11509 ± 0.00100	22
	HST/WFC3	G141	1.5065-1.5290	0.11635 ± 0.00104	22
	HST/WFC3	G141	1.5290-1.5525	0.11626 ± 0.00091	22
	HST/WFC3	G141	1.5525-1.5755	0.11681 ± 0.00091	22
	HST/WFC3	G141	1.5755-1.5985	0.11443 ± 0.00091	22
	HST/WFC3	G141	1.5985-1.6215	0.11631 ± 0.00091	22
	HST/WFC3	G141	1.6215-1.6445	0.11620 ± 0.00092	22

Table F.4: Observed transit depths of GJ 1214b

Reference	Telescope/Instrument	Filter/grism	Wavelength [μm]	R_p/R_s	Filter No.
	HST/WFC3	G141	1.6445-1.6675	0.11581 ± 0.00096	22
Murgas et al. (2012)	GTC/OSIRIS	RTF	0.6523-0.6547	0.151 ± 0.0025	42
	GTC/OSIRIS	RTF	0.6551-0.6575	0.1217 ± 0.0025	42
	GTC/OSIRIS	RTF	0.6608-0.6632	0.1184 ± 0.0026	43
Fraine et al. (2013)	Spitzer/IRAC	4.5 um		0.11735 ± 0.00064	78
	Spitzer/IRAC	4.5 um		0.11692 ± 0.00077	78
	Spitzer/IRAC	4.5 um		0.11681 ± 0.00057	78
	Spitzer/IRAC	4.5 um		0.11625 ± 0.00034	78
	Spitzer/IRAC	4.5 um		0.11796 ± 0.00054	78
	Spitzer/IRAC	4.5 um		0.11586 ± 0.00100	78
	Spitzer/IRAC	4.5 um		0.11803 ± 0.00052	78
	Spitzer/IRAC	4.5 um		0.11865 ± 0.00049	78
	Spitzer/IRAC	4.5 um		0.11737 ± 0.00053	78
	Spitzer/IRAC	4.5 um		0.11606 ± 0.00075	78
	Spitzer/IRAC	4.5 um		0.11567 ± 0.00047	78
	Spitzer/IRAC	4.5 um		0.11802 ± 0.00062	78
	Spitzer/IRAC	4.5 um		0.11549 ± 0.00066	78
	Spitzer/IRAC	3.6 um		0.11619 ± 0.00121	77
	Spitzer/IRAC	3.6 um		0.11584 ± 0.00066	77
	TRAPPIST	I+z		0.11680 ± 0.00135	81
	TRAPPIST	I+z		0.12389 ± 0.00216	81
	TRAPPIST	I+z		0.11389 ± 0.00275	81
	TRAPPIST	I+z		0.11573 ± 0.00331	81
	TRAPPIST	I+z		0.12138 ± 0.00182	81
	TRAPPIST	I+z		0.10802 ± 0.00296	81
	TRAPPIST	I+z		0.11877 ± 0.00228	81
Teske et al. (2013)	Kuiper 1.55 m	Harris R		$0.1203^{+0.0027}_{-0.0030}$	84
	Kuiper 1.55 m	Harris R		$0.1192^{+0.0037}_{-0.0040}$	84
	Kuiper 1.55 m	Harris V		$0.1108^{+0.0069}_{-0.0088}$	83
	STELLA .2 m	Sloan g'		$0.1210^{+0.0096}_{-0.011}$	28
	Kuiper 1.55 m	Harris V		$0.1093^{+0.0049}_{-0.0050}$	83
	STELLA .2 m	Sloan g'		$0.1197^{+0.0068}_{-0.0070}$	28
	STELLA .2 m	Sloan g'		$0.1058^{+0.0096}_{-0.012}$	28
	STELLA .2 m	Sloan g'		$0.1077^{+0.0078}_{-0.0082}$	28
	STELLA .2 m	Sloan g'		$0.1250^{+0.012}_{-0.018}$	28
	Kuiper 1.55 m	Harris R		$0.1192^{+0.0026}_{-0.0029}$	84
	Kuiper 1.55 m	Harris V		$0.1108^{+0.0027}_{-0.0028}$	83
	STELLA .2 m	Sloan g'		$0.1169^{+0.0041}_{-0.0043}$	28
Narita et al. (2013a)	IRSF/SIRIUS	J		0.11833 ± 0.00077	5
	IRSF/SIRIUS	H		0.11522 ± 0.00079	6
	IRSF/SIRIUS	Ks		0.11459 ± 0.00099	7
Narita et al. (2013b)	Subaru/Suprime-Cam	Johnson-Cousins B		0.11651 ± 0.00065	29
	Subaru/FOCAS	Johnson-Cousins B		0.11601 ± 0.00117	30
	IRSF/SIRIUS	J		0.11654 ± 0.00080	5
	IRSF/SIRIUS	H		$0.11550^{+0.00142}_{-0.00153}$	6
	IRSF/SIRIUS	Ks		0.11547 ± 0.00127	7
de Mooij et al. (2013)	VLT/FORS	B-high		0.1162 ± 0.0017	39
	WHT/ACAM	g		0.1180 ± 0.0009	40
	INT/WFC	g		0.1174 ± 0.0017	41
Colón & Gaidos (2013)	UKITRT/WFCAM	Ks		$0.1161^{+0.0047}_{-0.0048}$	35
	UKITRT/WFCAM	Ks		$0.1162^{+0.0040}_{-0.0041}$	35

Table F.4: Observed transit depths of GJ 1214b

Reference	Telescope/Instrument	Filter/grism	Wavelength [μm]	R_p/R_s	Filter No.
	UKITRT/WFCAM	Ks		$0.1152^{+0.0034}_{-0.0036}$	35
	UKITRT/WFCAM	Ks		$0.1133^{+0.0026}_{-0.0028}$	35
	UKITRT/WFCAM	Ks		$0.1224^{+0.0073}_{-0.0078}$	35
	UKITRT/WFCAM	Ks		$0.1153^{+0.0031}_{-0.0032}$	35
	UKITRT/WFCAM	Ks		0.1176 ± 0.0028	35
Kreidberg et al. (2014)	HST/WFC3	G141	1.135-1.158	0.013451 ± 0.000031	22
	HST/WFC3	G141	1.158-1.181	0.013462 ± 0.000030	22
	HST/WFC3	G141	1.181-1.204	0.013524 ± 0.000030	22
	HST/WFC3	G141	1.205-1.228	0.013442 ± 0.000028	22
	HST/WFC3	G141	1.228-1.251	0.013517 ± 0.000028	22
	HST/WFC3	G141	1.251-1.274	0.013495 ± 0.000027	22
	HST/WFC3	G141	1.274-1.297	0.013503 ± 0.000027	22
	HST/WFC3	G141	1.297-1.320	0.013504 ± 0.000026	22
	HST/WFC3	G141	1.320-1.343	0.013519 ± 0.000026	22
	HST/WFC3	G141	1.343-1.366	0.013488 ± 0.000027	22
	HST/WFC3	G141	1.366-1.389	0.013522 ± 0.000027	22
	HST/WFC3	G141	1.389-1.412	0.013521 ± 0.000027	22
	HST/WFC3	G141	1.412-1.435	0.013485 ± 0.000027	22
	HST/WFC3	G141	1.435-1.458	0.013519 ± 0.000029	22
	HST/WFC3	G141	1.458-1.481	0.013482 ± 0.000028	22
	HST/WFC3	G141	1.481-1.504	0.013517 ± 0.000028	22
	HST/WFC3	G141	1.504-1.527	0.013479 ± 0.000028	22
	HST/WFC3	G141	1.527-1.550	0.013510 ± 0.000028	22
	HST/WFC3	G141	1.550-1.573	0.013469 ± 0.000028	22
	HST/WFC3	G141	1.573-1.596	0.013425 ± 0.000028	22
	HST/WFC3	G141	1.596-1.619	0.013473 ± 0.000028	22
	HST/WFC3	G141	1.619-1.642	0.013473 ± 0.000030	22
Wilson et al. (2014)	GTC/OSIRIS	TF	0.80880-0.81120	0.12038 ± 0.0013	53
	GTC/OSIRIS	TF	0.85380-0.85620	0.11042 ± 0.0014	55
	GTC/OSIRIS	TF	0.87580-0.87820	0.11843 ± 0.0025	56
	GTC/OSIRIS	TF	0.87580-0.87820	0.11754 ± 0.0016	56
	GTC/OSIRIS	TF	0.87725-0.87965	0.11724 ± 0.0020	56
	GTC/OSIRIS	TF	0.88230-0.88470	0.11556 ± 0.0032	56
	GTC/OSIRIS	TF	0.88230-0.88470	0.11791 ± 0.0016	56
	GTC/OSIRIS	TF	0.88376-0.88616	0.11595 ± 0.0024	56
Cáceres et al. (2014)	SOAR/OSIRIS	2.14 um		$0.1173^{+0.0022}_{-0.0024}$	66
	SOAR/SOI	I-Bessel		$0.11735^{+0.00072}_{-0.00076}$	67
	NTT/SofI	H		$0.1205^{+0.0070}_{-0.0074}$	68
	NTT/SofI	K		$0.1230^{+0.0084}_{-0.0090}$	69
	NTT/SofI	H		$0.1180^{+0.0058}_{-0.0062}$	68
	NTT/SofI	K		$0.1202^{+0.0100}_{-0.0110}$	69
Nascimbeni et al. (2015b)	LBT/LBC	B		$0.1176^{+0.0009}_{-0.0009}$	90
	LBT/LBC	R		$0.1175^{+0.0004}_{-0.0004}$	91
Rackham et al. (2017)	Magellan/IMACS	f/4	0.45000-0.56570	$0.1121^{+0.0020}_{-0.0020}$	99
	Magellan/IMACS	f/4	0.56570-0.61960	$0.1119^{+0.0017}_{-0.0018}$	99
	Magellan/IMACS	f/4	0.61960-0.65060	$0.1153^{+0.0015}_{-0.0015}$	99
	Magellan/IMACS	f/4	0.65960-0.70540	$0.1112^{+0.0015}_{-0.0015}$	99
	Magellan/IMACS	f/4	0.72540-0.74850	$0.1147^{+0.0012}_{-0.0012}$	99
	Magellan/IMACS	f/4	0.74850-0.77280	$0.1130^{+0.0013}_{-0.0013}$	99
	Magellan/IMACS	f/4	0.77280-0.79670	$0.1155^{+0.0013}_{-0.0013}$	99
	Magellan/IMACS	f/4	0.79670-0.81420	$0.1157^{+0.0015}_{-0.0016}$	99

Table F.4: Observed transit depths of GJ 1214b

Reference	Telescope/Instrument	Filter/grism	Wavelength [μm]	R_p/R_s	Filter No.
	Magellan/IMACS	f/4	0.81420-0.83160	$0.1150^{+0.0018}_{-0.0019}$	99
	Magellan/IMACS	f/4	0.83160-0.85020	$0.1133^{+0.0013}_{-0.0013}$	99
	Magellan/IMACS	f/4	0.85020-0.86920	$0.1150^{+0.0014}_{-0.0014}$	99
	Magellan/IMACS	f/4	0.86920-0.88680	$0.1136^{+0.0013}_{-0.0014}$	99
	Magellan/IMACS	f/4	0.88680-0.90650	$0.1164^{+0.0017}_{-0.0017}$	99
	Magellan/IMACS	f/4	0.90650-0.92600	$0.1165^{+0.0022}_{-0.0023}$	99
	Magellan/IMACS	f/4	0.45000-0.56570	$0.1129^{+0.0021}_{-0.0021}$	99
	Magellan/IMACS	f/4	0.56570-0.61960	$0.1139^{+0.0017}_{-0.0018}$	99
	Magellan/IMACS	f/4	0.61960-0.65060	$0.1125^{+0.0024}_{-0.0025}$	99
	Magellan/IMACS	f/4	0.65960-0.70540	$0.1153^{+0.0024}_{-0.0025}$	99
	Magellan/IMACS	f/4	0.72540-0.74850	$0.1151^{+0.0017}_{-0.0016}$	99
	Magellan/IMACS	f/4	0.74850-0.77280	$0.1161^{+0.0014}_{-0.0013}$	99
	Magellan/IMACS	f/4	0.77280-0.79670	$0.1154^{+0.0011}_{-0.0011}$	99
	Magellan/IMACS	f/4	0.79670-0.81420	$0.1174^{+0.0013}_{-0.0012}$	99
	Magellan/IMACS	f/4	0.81420-0.83160	$0.1172^{+0.0019}_{-0.0019}$	99
	Magellan/IMACS	f/4	0.83160-0.85020	$0.1162^{+0.0016}_{-0.0016}$	99
	Magellan/IMACS	f/4	0.85020-0.86920	$0.1159^{+0.0015}_{-0.0016}$	99
	Magellan/IMACS	f/4	0.86920-0.88680	$0.1161^{+0.0018}_{-0.0018}$	99
	Magellan/IMACS	f/4	0.88680-0.90650	$0.1161^{+0.0017}_{-0.0017}$	99
	Magellan/IMACS	f/4	0.90650-0.92600	$0.1153^{+0.0016}_{-0.0016}$	99
	Magellan/IMACS	f/2	0.45000-0.56570	$0.1172^{+0.0026}_{-0.0027}$	98
	Magellan/IMACS	f/2	0.56570-0.61960	$0.1140^{+0.0021}_{-0.0021}$	98
	Magellan/IMACS	f/2	0.61960-0.65060	$0.1149^{+0.0013}_{-0.0013}$	98
	Magellan/IMACS	f/2	0.65960-0.70540	$0.1157^{+0.0019}_{-0.0019}$	98
	Magellan/IMACS	f/2	0.72540-0.74850	$0.1138^{+0.0008}_{-0.0008}$	98
	Magellan/IMACS	f/2	0.74850-0.77280	$0.1149^{+0.0011}_{-0.0012}$	98
	Magellan/IMACS	f/2	0.77280-0.79670	$0.1138^{+0.0012}_{-0.0011}$	98
	Magellan/IMACS	f/2	0.79670-0.81420	$0.1138^{+0.0011}_{-0.0010}$	98
	Magellan/IMACS	f/2	0.81420-0.83160	$0.1146^{+0.0010}_{-0.0010}$	98
	Magellan/IMACS	f/2	0.83160-0.85020	$0.1153^{+0.0011}_{-0.0011}$	98
	Magellan/IMACS	f/2	0.85020-0.86920	$0.1168^{+0.0013}_{-0.0014}$	98
	Magellan/IMACS	f/2	0.86920-0.88680	$0.1128^{+0.0014}_{-0.0013}$	98
	Magellan/IMACS	f/2	0.88680-0.90650	$0.1141^{+0.0016}_{-0.0017}$	98
	Magellan/IMACS	f/2	0.90650-0.92600	$0.1147^{+0.0014}_{-0.0014}$	98

The information about the filters are listed in Table G.7.

[a]First presented by Bean et al. (2010), reanalyzed by Bean et al. (2011).

Table F.5: Observed transit depths of GJ 3470b

Reference	Telescope/Instrument	Filter/grism	Wavelength [μm]	R_p/R_s	Filter No.
Demory et al. (2013)	*Spitzer*/IRAC	4.5 μm		$0.07798^{+0.00046}_{-0.00045}$	78
	Spitzer/IRAC	4.5 μm			
Fukui et al. (2013)	OAO 188 cm	J		$0.07577^{+0.00072}_{-0.00075}$	1
	MITSuME 50 cm	I_c		0.0802 ± 0.0013 [a]	4
	MITSuME 50 cm	R_c		0.0776 ± 0.0018 [a]	3
	MITSuME 50 cm	g'		0.0809 ± 0.0031 [a]	2
Crossfield et al. (2013)	Keck/MOSFIRE	K	2.09-2.13	$0.0775^{+0.0033}_{-0.0036}$	19
	Keck/MOSFIRE	K	2.13-2.17	$0.0800^{+0.0027}_{-0.0022}$	19
	Keck/MOSFIRE	K	2.17-2.21	$0.0807^{+0.0027}_{-0.0024}$	19
	Keck/MOSFIRE	K	2.21-2.26	$0.0785^{+0.0021}_{-0.0020}$	19
	Keck/MOSFIRE	K	2.26-2.31	$0.0793^{+0.0022}_{-0.0026}$	19
	Keck/MOSFIRE	K	2.31-2.36	$0.0767^{+0.0024}_{-0.0021}$	19
Nascimbeni et al. (2013)	LBT/LBC	$F972N20$		$0.07484^{+0.00052}_{-0.00048}$	20
	LBT/LBC	U_{spec}		0.0821 ± 0.0013	21
Ehrenreich et al. (2014)	HST/WFC3	G141	1.1510-1.1550	0.08114 ± 0.00251 [b]	22
	HST/WFC3	G141	1.1550-1.1595	0.07884 ± 0.00202 [b]	22
	HST/WFC3	G141	1.1595-1.1645	0.07896 ± 0.00244 [b]	22
	HST/WFC3	G141	1.1645-1.1690	0.07703 ± 0.00260 [b]	22
	HST/WFC3	G141	1.1690-1.1735	0.07557 ± 0.00258 [b]	22
	HST/WFC3	G141	1.1735-1.1785	0.07921 ± 0.00240 [b]	22
	HST/WFC3	G141	1.1785-1.1830	0.07841 ± 0.00254 [b]	22
	HST/WFC3	G141	1.1830-1.1875	0.07615 ± 0.00275 [b]	22
	HST/WFC3	G141	1.1875-1.1925	0.07984 ± 0.00287 [b]	22
	HST/WFC3	G141	1.1925-1.1970	0.08195 ± 0.00243 [b]	22
	HST/WFC3	G141	1.1970-1.2015	0.08110 ± 0.00244 [b]	22
	HST/WFC3	G141	1.2015-1.2065	0.07439 ± 0.00270 [b]	22
	HST/WFC3	G141	1.2065-1.2110	0.07596 ± 0.00320 [b]	22
	HST/WFC3	G141	1.2110-1.2155	0.07735 ± 0.00230 [b]	22
	HST/WFC3	G141	1.2155-1.2205	0.08105 ± 0.00273 [b]	22
	HST/WFC3	G141	1.2205-1.2250	0.07596 ± 0.00341 [b]	22
	HST/WFC3	G141	1.2250-1.2295	0.07905 ± 0.00258 [b]	22
	HST/WFC3	G141	1.2295-1.2340	0.08027 ± 0.00346 [b]	22
	HST/WFC3	G141	1.2340-1.2385	0.07686 ± 0.00251 [b]	22
	HST/WFC3	G141	1.2385-1.2435	0.07424 ± 0.00335 [b]	22
	HST/WFC3	G141	1.2435-1.2480	0.07828 ± 0.00283 [b]	22
	HST/WFC3	G141	1.2480-1.2525	0.07950 ± 0.00351 [b]	22
	HST/WFC3	G141	1.2525-1.2575	0.08140 ± 0.00293 [b]	22
	HST/WFC3	G141	1.2575-1.2620	0.07542 ± 0.00301 [b]	22
	HST/WFC3	G141	1.2620-1.2665	0.07561 ± 0.00270 [b]	22
	HST/WFC3	G141	1.2665-1.2715	0.07215 ± 0.00312 [b]	22
	HST/WFC3	G141	1.2715-1.2760	0.07912 ± 0.00276 [b]	22
	HST/WFC3	G141	1.2760-1.2805	0.08033 ± 0.00279 [b]	22
	HST/WFC3	G141	1.2805-1.2855	0.08141 ± 0.00267 [b]	22
	HST/WFC3	G141	1.2855-1.2900	0.07550 ± 0.00235 [b]	22
	HST/WFC3	G141	1.2900-1.2945	0.07464 ± 0.00343 [b]	22
	HST/WFC3	G141	1.2945-1.2990	0.08013 ± 0.00327 [b]	22
	HST/WFC3	G141	1.2990-1.3035	0.08059 ± 0.00295 [b]	22
	HST/WFC3	G141	1.3035-1.3085	0.08206 ± 0.00294 [b]	22
	HST/WFC3	G141	1.3085-1.3130	0.07435 ± 0.00325 [b]	22
	HST/WFC3	G141	1.3130-1.3175	0.07955 ± 0.00316 [b]	22
	HST/WFC3	G141	1.3175-1.3225	0.07844 ± 0.00273 [b]	22

Table F.5: Observed transit depths of GJ 3470b

Reference	Telescope/Instrument	Filter/grism	Wavelength [μm]	R_p/R_s	Filter No.
	HST/WFC3	G141	1.3225-1.3270	0.08461 ± 0.00234 [b]	22
	HST/WFC3	G141	1.3270-1.3315	0.08012 ± 0.00254 [b]	22
	HST/WFC3	G141	1.3315-1.3365	0.07955 ± 0.00248 [b]	22
	HST/WFC3	G141	1.3365-1.3410	0.07273 ± 0.00313 [b]	22
	HST/WFC3	G141	1.3410-1.3455	0.08083 ± 0.00260 [b]	22
	HST/WFC3	G141	1.3455-1.3505	0.08193 ± 0.00292 [b]	22
	HST/WFC3	G141	1.3505-1.3550	0.08189 ± 0.00263 [b]	22
	HST/WFC3	G141	1.3550-1.3595	0.08571 ± 0.00226 [b]	22
	HST/WFC3	G141	1.3595-1.3640	0.08306 ± 0.00254 [b]	22
	HST/WFC3	G141	1.3640-1.3685	0.07876 ± 0.00269 [b]	22
	HST/WFC3	G141	1.3685-1.3735	0.07241 ± 0.00288 [b]	22
	HST/WFC3	G141	1.3735-1.3780	0.08271 ± 0.00286 [b]	22
	HST/WFC3	G141	1.3780-1.3825	0.07755 ± 0.00253 [b]	22
	HST/WFC3	G141	1.3825-1.3875	0.07185 ± 0.00294 [b]	22
	HST/WFC3	G141	1.3875-1.3920	0.07631 ± 0.00280 [b]	22
	HST/WFC3	G141	1.3920-1.3965	0.07902 ± 0.00241 [b]	22
	HST/WFC3	G141	1.3965-1.4015	0.07898 ± 0.00255 [b]	22
	HST/WFC3	G141	1.4015-1.4060	0.07616 ± 0.00258 [b]	22
	HST/WFC3	G141	1.4060-1.4105	0.08306 ± 0.00289 [b]	22
	HST/WFC3	G141	1.4105-1.4155	0.07857 ± 0.00226 [b]	22
	HST/WFC3	G141	1.4155-1.4200	0.06891 ± 0.00329 [b]	22
	HST/WFC3	G141	1.4200-1.4245	0.08018 ± 0.00278 [b]	22
	HST/WFC3	G141	1.4245-1.4295	0.07342 ± 0.00328 [b]	22
	HST/WFC3	G141	1.4295-1.4340	0.08046 ± 0.00212 [b]	22
	HST/WFC3	G141	1.4340-1.4385	0.07819 ± 0.00281 [b]	22
	HST/WFC3	G141	1.4385-1.4430	0.08028 ± 0.00242 [b]	22
	HST/WFC3	G141	1.4430-1.4475	0.08427 ± 0.00233 [b]	22
	HST/WFC3	G141	1.4475-1.4525	0.07419 ± 0.00296 [b]	22
	HST/WFC3	G141	1.4525-1.4570	0.07692 ± 0.00272 [b]	22
	HST/WFC3	G141	1.4570-1.4615	0.08261 ± 0.00239 [b]	22
	HST/WFC3	G141	1.4615-1.4665	0.08052 ± 0.00239 [b]	22
	HST/WFC3	G141	1.4665-1.4710	0.07318 ± 0.00245 [b]	22
	HST/WFC3	G141	1.4710-1.4755	0.07988 ± 0.00235 [b]	22
	HST/WFC3	G141	1.4755-1.4805	0.08339 ± 0.00221 [b]	22
	HST/WFC3	G141	1.4805-1.4850	0.07779 ± 0.00239 [b]	22
	HST/WFC3	G141	1.4850-1.4895	0.07916 ± 0.00180 [b]	22
	HST/WFC3	G141	1.4895-1.4945	0.07709 ± 0.00220 [b]	22
	HST/WFC3	G141	1.4945-1.4990	0.08431 ± 0.00218 [b]	22
	HST/WFC3	G141	1.4990-1.5035	0.07801 ± 0.00211 [b]	22
	HST/WFC3	G141	1.5035-1.5080	0.07541 ± 0.00238 [b]	22
	HST/WFC3	G141	1.5080-1.5125	0.07906 ± 0.00239 [b]	22
	HST/WFC3	G141	1.5125-1.5175	0.07506 ± 0.00249 [b]	22
	HST/WFC3	G141	1.5175-1.5220	0.07624 ± 0.00196 [b]	22
	HST/WFC3	G141	1.5220-1.5265	0.07865 ± 0.00259 [b]	22
	HST/WFC3	G141	1.5265-1.5315	0.07707 ± 0.00254 [b]	22
	HST/WFC3	G141	1.5315-1.5360	0.07780 ± 0.00240 [b]	22
	HST/WFC3	G141	1.5360-1.5405	0.07305 ± 0.00255 [b]	22
	HST/WFC3	G141	1.5405-1.5455	0.07378 ± 0.00458 [b]	22
	HST/WFC3	G141	1.5455-1.5500	0.07773 ± 0.00277 [b]	22
	HST/WFC3	G141	1.5500-1.5545	0.07739 ± 0.00247 [b]	22
	HST/WFC3	G141	1.5545-1.5595	0.08317 ± 0.00223 [b]	22

Table F.5: Observed transit depths of GJ 3470b

Reference	Telescope/Instrument	Filter/grism	Wavelength [μm]	R_p/R_s	Filter No.
	HST/WFC3	G141	1.5595-1.5640	0.07987 ± 0.00209 [b]	22
	HST/WFC3	G141	1.5640-1.5685	0.07515 ± 0.00213 [b]	22
	HST/WFC3	G141	1.5685-1.5730	0.08324 ± 0.00222 [b]	22
	HST/WFC3	G141	1.5730-1.5775	0.08242 ± 0.00232 [b]	22
	HST/WFC3	G141	1.5775-1.5825	0.07739 ± 0.00230 [b]	22
	HST/WFC3	G141	1.5825-1.5870	0.07902 ± 0.00204 [b]	22
	HST/WFC3	G141	1.5870-1.5915	0.07823 ± 0.00244 [b]	22
	HST/WFC3	G141	1.5915-1.5965	0.07863 ± 0.00253 [b]	22
	HST/WFC3	G141	1.5965-1.6010	0.08002 ± 0.00238 [b]	22
	HST/WFC3	G141	1.6010-1.6055	0.07578 ± 0.00261 [b]	22
	HST/WFC3	G141	1.6055-1.6105	0.07894 ± 0.00239 [b]	22
	HST/WFC3	G141	1.6105-1.6150	0.08069 ± 0.00255 [b]	22
	HST/WFC3	G141	1.6150-1.6195	0.08044 ± 0.00227 [b]	22
	HST/WFC3	G141	1.6195-1.6245	0.07980 ± 0.00244 [b]	22
	HST/WFC3	G141	1.6245-1.6290	0.08002 ± 0.00235 [b]	22
	HST/WFC3	G141	1.6290-1.6335	0.07912 ± 0.00264 [b]	22
	HST/WFC3	G141	1.6335-1.6380	0.07878 ± 0.00231 [b]	22
	HST/WFC3	G141	1.6380-1.6425	0.08008 ± 0.00221 [b]	22
	HST/WFC3	G141	1.6425-1.6475	0.07879 ± 0.00234 [b]	22
Biddle et al. (2014)	Nickel	Gunn Z			
	LSC	Panstarrs-Z		$0.0766^{+0.0019}_{-0.0020}$	26
	Nickel	Gunn Z			
	Nickel	Gunn Z			
	LSC	r'			
	ELP	r'		0.0803 ± 0.0025	9
	ELP	r'			
	DCT	I		$0.0780^{+0.0015}_{-0.0016}$	24
	CAHA 1.23-m	Cousins I			
	Kuiper	Arizona-I		$0.0736^{+0.0029}_{-0.0031}$	27
	FTN	Bessel-B		$0.084^{+0.013}_{-0.016}$	23
Dragomir et al. (2015)	LCOGT	g'		$0.0833^{+0.0019}_{-0.0019}$	100
	LCOGT	i'		$0.0771^{+0.0012}_{-0.0011}$	101
	Kuiper	B		$0.0827^{+0.0022}_{-0.0020}$	102
	Kuiper	V		$0.0770^{+0.0020}_{-0.0019}$	83
Awiphan et al. (2016b)	TNT	z'		$0.0744^{+0.0020}_{-0.0020}$	11
	TNT	i'		$0.0785^{+0.0008}_{-0.0008}$ [c]	10
	TNO 0.5m/PROMPT-8	Cousins-R		$0.0765^{+0.0017}_{-0.0015}$	3
	TNT	r'		$0.0787^{+0.0016}_{-0.0022}$	9
	TNT	g'		$0.0832^{+0.0027}_{-0.0027}$	8
Chen et al. (2017)	GTC/OSIRIS	R1000B	0.435-0.485	$0.0787^{+0.0013}_{-0.0013}$	103
	GTC/OSIRIS	R1000B	0.485-0.530	$0.0788^{+0.0009}_{-0.0009}$	103
	GTC/OSIRIS	R1000B	0.530-0.575	$0.0780^{+0.0005}_{-0.0005}$	103
	GTC/OSIRIS	R1000B	0.575-0.615	$0.0773^{+0.0006}_{-0.0006}$	103
	GTC/OSIRIS	R1000B	0.615-0.640	$0.0775^{+0.0006}_{-0.0006}$	103
	GTC/OSIRIS	R1000B	0.640-0.665	$0.0768^{+0.0005}_{-0.0005}$	103
	GTC/OSIRIS	R1000B	0.665-0.690	$0.0771^{+0.0007}_{-0.0007}$	103
	GTC/OSIRIS	R1000B	0.690-0.715	$0.0779^{+0.0005}_{-0.0005}$	103
	GTC/OSIRIS	R1000B	0.715-0.735	$0.0759^{+0.0005}_{-0.0005}$	103
	GTC/OSIRIS	R1000B	0.735-0.755	$0.0778^{+0.0005}_{-0.0005}$	103

The information about the filters are listed in Table G.7.

---

[a]Derived by the MCMC analysis using the value of impact parameter reported by Demory et al. (2013) as prior information.
[b]Results of the divide-oot procedure.
[c]Analyzed including the observational data of Biddle et al. (2014), not listed here.

Table F.6: Observed transit depths of GJ 436b

Reference	Telescope/Instrument	Filter/grism	Wavelength [μm]	R_p/R_s	Filter No.
Alonso et al. (2008)	1.52 m Telescopio Carlos Sánchez (TCS)/CAIN-II	H		$0.0841^{+0.0011}_{-0.0011}$	97
Cáceres et al. (2009)	3.6-m ESO New Technology Telescope (NTT)/SofI	Ks		$0.0064^{+0.0003}_{-0.0003}$	69
Pont et al. (2009)	HST/NICMOS	G141		$0.0831^{+0.0005}_{-0.0005}$	96
Beaulieu et al. (2011)	Spitzer/IRAC	3.6 um (sub)		$0.007120^{+0.000060}_{-0.000060}$	77
	Spitzer/IRAC	4.5 um (sub)		$0.006380^{+0.000180}_{-0.000180}$	78
Knutson et al. (2011)	Spitzer/IRAC	3.6 um (sub)		$0.08182^{+0.00037}_{-0.00037}$	77
	Spitzer/IRAC	4.5 um (sub)		$0.08502^{+0.00057}_{-0.00057}$	78
Knutson et al. (2014)	HST/WFC3	G141	1.1265-1.1455	$0.006966^{+0.000060}_{-0.000060}$	22
	HST/WFC3	G141	1.1455-1.1645	$0.006994^{+0.000050}_{-0.000050}$	22
	HST/WFC3	G141	1.1645-1.1835	$0.006924^{+0.000040}_{-0.000040}$	22
	HST/WFC3	G141	1.1835-1.2020	$0.006872^{+0.000057}_{-0.000057}$	22
	HST/WFC3	G141	1.2020-1.2205	$0.006968^{+0.000039}_{-0.000039}$	22
	HST/WFC3	G141	1.2205-1.2395	$0.007046^{+0.000038}_{-0.000038}$	22
	HST/WFC3	G141	1.2395-1.2585	$0.007036^{+0.000039}_{-0.000039}$	22
	HST/WFC3	G141	1.2585-1.2785	$0.006967^{+0.000035}_{-0.000035}$	22
	HST/WFC3	G141	1.2785-1.2975	$0.006989^{+0.000035}_{-0.000035}$	22
	HST/WFC3	G141	1.2975-1.3150	$0.007043^{+0.000038}_{-0.000038}$	22
	HST/WFC3	G141	1.3150-1.3335	$0.006989^{+0.000038}_{-0.000038}$	22
	HST/WFC3	G141	1.3335-1.3525	$0.007046^{+0.000042}_{-0.000042}$	22
	HST/WFC3	G141	1.3525-1.3715	$0.007057^{+0.000037}_{-0.000037}$	22
	HST/WFC3	G141	1.3715-1.3905	$0.007006^{+0.000037}_{-0.000037}$	22
	HST/WFC3	G141	1.3905-1.4095	$0.007036^{+0.000050}_{-0.000050}$	22
	HST/WFC3	G141	1.4095-1.4285	$0.007072^{+0.000046}_{-0.000046}$	22
	HST/WFC3	G141	1.4285-1.4470	$0.007030^{+0.000042}_{-0.000042}$	22
	HST/WFC3	G141	1.4470-1.4655	$0.007044^{+0.000042}_{-0.000042}$	22
	HST/WFC3	G141	1.4655-1.4845	$0.006948^{+0.000039}_{-0.000039}$	22
	HST/WFC3	G141	1.4845-1.5035	$0.007008^{+0.000039}_{-0.000039}$	22
	HST/WFC3	G141	1.5035-1.5225	$0.007057^{+0.000040}_{-0.000040}$	22
	HST/WFC3	G141	1.5225-1.5415	$0.007022^{+0.000044}_{-0.000044}$	22
	HST/WFC3	G141	1.5415-1.5605	$0.007018^{+0.000040}_{-0.000040}$	22
	HST/WFC3	G141	1.5605-1.5790	$0.007010^{+0.000037}_{-0.000037}$	22
	HST/WFC3	G141	1.5790-1.5975	$0.006959^{+0.000040}_{-0.000040}$	22
	HST/WFC3	G141	1.5975-1.6165	$0.006994^{+0.000044}_{-0.000044}$	22
	HST/WFC3	G141	1.6165-1.6355	$0.006984^{+0.000044}_{-0.000044}$	22
	HST/WFC3	G141	1.6355-1.6545	$0.006916^{+0.000059}_{-0.000059}$	22

The information about the filters are listed in Table G.7.

G References of filter/grism transmission curve

Table G.7: Filter/grism transmission curves used in this thesis

No.	Telescope/Instrument	Filter	Reference
1	OAO188cm/ISLE	J	Used in Fukui et al. (2013) and Fukui et al. (2014), private communication
2	MITSuME 50cm	g'	Used in Fukui et al. (2013) and Fukui et al. (2014), private communication
3	MITSuME 50cm	R_c	Used in Fukui et al. (2013) and Fukui et al. (2014), private communication
4	MITSuME 50cm	I_c	Used in Fukui et al. (2013) and Fukui et al. (2014), private communication
5	IRSF/SIRIUS	J	Used in Narita et al. (2013b) and Fukui et al. (2014), private communication
6	IRSF/SIRIUS	H	Used in Narita et al. (2013b) and Fukui et al. (2014), private communication
7	IRSF/SIRIUS	K_s	Used in Narita et al. (2013b) and Fukui et al. (2014), private communication
8	MPG/ESO 2.2-m	Sloan g'	Used in Mancini et al. (2014), private communication
9	MPG/ESO 2.2-m	Sloan r'	Used in Mancini et al. (2014), private communication
10	MPG/ESO 2.2-m	Sloan i'	Used in Mancini et al. (2014), private communication
11	MPG/ESO 2.2-m	Sloan z'	Used in Mancini et al. (2014), private communication
19	Keck/MOSFIRE	K	http://ww2.keck.hawaii.edu/inst/mosfire/filters.html
20	LBT/LBC	$F972N20$	http://abell.as.arizona.edu/~lbtsci/Instruments/LBC/lbc_description.html
21	LBT/LBC	U_{spec}	http://abell.as.arizona.edu/~lbtsci/Instruments/LBC/lbc_description.html
22	HST/WFC3	G141	http://svo2.cab.inta-csic.es/svo/theory/fps3/
23		Bessel B	http://catserver.ing.iac.es/filter/
24	DCT	I	http://www.lowell.edu/techSpecs/LMI/specs.html
26	LSC	Panstarrs-Z	Used in Biddle et al. (2014), private communication
27	Kuiper	Arizona-I	Used in Biddle et al. (2014), private communication
28	STELA	Sloan g'	http://www.aip.de/en/research/facilities/stella/instruments/data/sloanugriz-filter-curves
29	Subaru/Suprime-Cam	B	http://www.naoj.org/Observing/Instruments/SCam/sensitivity.html
30	Subaru/FOCAS	B	http://www.naoj.org/Observing/Instruments/FOCAS/camera/filters.html
31	INT/WFC	Sloan r	http://catserver.ing.iac.es/filter/
32	INT/WFC	Sloan I	http://catserver.ing.iac.es/filter/
33	NOT/NOTCam	Ks	http://www.not.iac.es/instruments/notcam/filters/index.html
34	WHT/LIRIS	Kc	http://www.ing.iac.es/Astronomy/instruments/liris/config.html
35	UKIRT/WFCAM	K	http://www.jach.hawaii.edu/UKIRT/instruments/wfcam/user_guide/description.html
36	CFHT/WIRCam	J	http://www.cfht.hawaii.edu/Instruments/Imaging/WIRCam/WIRCamThroughput.html
37	CFHT/WIRCam	Ks	http://www.cfht.hawaii.edu/Instruments/Imaging/WIRCam/WIRCamThroughput.html
38	CFHT/WIRCam	CH4On	http://www.cfht.hawaii.edu/Instruments/Imaging/WIRCam/WIRCamThroughput.html
39	VLT/FORS	B-high	http://www.eso.org/sci/facilities/paranal/instruments/fors/inst/Filters/curves.html
40	WHT/ACAM	g	http://catserver.ing.iac.es/filter/
41	INT/WFC	g	http://catserver.ing.iac.es/filter/
42	GTC/OSIRIS	f657/35	http://www.gtc.iac.es/instruments/osiris/osiris.php
43	GTC/OSIRIS	f666/36	http://www.gtc.iac.es/instruments/osiris/osiris.php
53	GTC/OSIRIS	f819/52	http://www.gtc.iac.es/instruments/osiris/osiris.php
55	GTC/OSIRIS	f858/58	http://www.gtc.iac.es/instruments/osiris/osiris.php
56	GTC/OSIRIS	f878/59	http://www.gtc.iac.es/instruments/osiris/osiris.php

Table G.7: Filter/grism transmission curves used in this thesis

No.	Telescope/Instrument	Filter	Reference
66	SOAR/OSIRIS	2.14 μm	http://www.ctio.noao.edu/instruments/ir_instruments/osiris2soar/config/index.html
67	SOAR/SOI	Bessell I	http://www.ctio.noao.edu/~points/SOIFILTERS/filters/maintext.html
68	NTT/SofI	H	http://www.eso.org/sci/facilities/lasilla/instruments/sofi/inst/Imaging.html
69	NTT/SofI	Ks	http://www.eso.org/sci/facilities/lasilla/instruments/sofi/inst/Imaging.html
70	Magellan/MMIRS	J	http://www.cfa.harvard.edu/mmti/mmirs/instrstats.html
71	Magellan/MMIRS	H	http://www.cfa.harvard.edu/mmti/mmirs/instrstats.html
72	Magellan/MMIRS	K	http://www.cfa.harvard.edu/mmti/mmirs/instrstats.html
73	VLT/FORS	GG435	http://www.eso.org/sci/facilities/paranal/instruments/fors/inst/Filters/curves.html
75	VLT/FORS	OG590	http://www.eso.org/sci/facilities/paranal/instruments/fors/inst/Filters/curves.html
76	VLT/HAWK	INB2090	http://www.eso.org/sci/facilities/paranal/instruments/hawki/inst.html
77	Spitzer/IRAC	ch1	http://irsa.ipac.caltech.edu/data/SPITZER/docs/irac/calibrationfiles/spectralresponse/
78	Spitzer/IRAC	ch2	http://irsa.ipac.caltech.edu/data/SPITZER/docs/irac/calibrationfiles/spectralresponse/
81		I+z	Sum of the filter curves of No.10 and No.11
82	1.2m/Keplercam	Sloan Z'	http://www.sao.arizona.edu/FLWO/48/CCD.filters.html
83	HARRIS	V	http://catserver.ing.iac.es/filter/ (#192)
84	HARRIS	R	http://catserver.ing.iac.es/filter/ (#193)
90	LBT/LBC	B	http://svo2.cab.inta-csic.es/theory/fps/
91	LBT/LBC	R	http://svo2.cab.inta-csic.es/theory/fps/
96	HST/NICMOS3	G141	http://svo2.cab.inta-csic.es/theory/fps/
97	TCS/CAIN3	H	http://svo2.cab.inta-csic.es/theory/fps/
98	Magellan/IMACS	f/2	http://www.lco.cl/telescopes-information/magellan/operations-homepage/instruments/IMACS/imacs-filters/imacs-filters-1
99	Magellan/IMACS	f/4	http://www.lco.cl/telescopes-information/magellan/operations-homepage/instruments/IMACS/imacs-filters/imacs-filters-1
100	LCOGT	g'	https://lco.global/observatory/filters/sdss-g/
101	LCOGT	i'	https://lco.global/observatory/filters/sdss-i/
102	HARRIS	B	http://catserver.ing.iac.es/filter/ (#191)
103	GTC/OSIRIS	R1000B	http://www.gtc.iac.es/instruments/osiris/#Longslit_Spectroscopy [a]

---

[a]The data is taken by tracing the figure with the use of the software, PlotDigitizer X (http://www.surf.nuqe.nagoya-u.ac.jp/ nakahara/software/plotdigitizerx/index-e.html)